Active Vibration and Buckling Control of Piezoelectric Smart Structures

Qishan Wang

Doctor of Philosophy

Civil Engineering and Applied Mechanics

McGill University

Montreal, Quebec

2012

Submitted in partial fulfillment of requirements for the degree of
Doctor of Philosophy

DEDICATION

Dedicated to my Mom and Dad

ACKNOWLEDGEMENTS

The author would like to thank his advisor Professor S. Shrivastava for his guidance, comments, and support throughout this research. Thanks also go to the office staff of the Department of Civil Engineering and Applied Mechanics at McGill University who made the completion of this research possible. Professor R. Gehr's beautiful music and invaluable comments are also greatly appreciated. Thanks are due to his office friends for their friendship and afternoon tea which will last, and be missed, for a life time. Finally, the author would like to thank all his family members for the continuous support to let him follow his dream.

ABSTRACT

The objective of this dissertation is the vibration and buckling control of piezo-laminated composite structures with surface bonded or embedded piezoelectric sensors and actuators by using the finite element analysis and LQR/LQG feedback control techniques.

The focus is mainly on two aspects: the finite element part and the active control part.

(1) The finite element part:

Two finite element formulations for the piezo-laminated beams based on the classical Bernoulli-Euler and the Timoshenko beam theories are developed using the coupled linear piezoelectric constitutive equations, and the Hamilton variational principle.

A C^0 continuous, shear flexible, eight-node serendipity doubly curved shell element for the piezolaminated composite plates and shells is also developed based on the layer-wise shear deformation theory, linear piezoelectric coupled constitutive relations, and Hamilton variational principle.

The developed elements can handle the transverse shear strains, composite materials, and piezoelectric-mechanical coupling. Higher modes of vibration can then be predicted more precisely for thin to medium-thick multilayered composite structures. They are evaluated both for the vibration and buckling of beam, plate, and shell structures.

(2) The active control part:

The suppression of vibration of a cantilever piezo-laminated beam and the control of the first two buckling modes of a simply supported piezo-laminated beam are studied first. Then, the vibration and buckling control of a cantilever piezo-laminated composite plate are studied. Furthermore, the vibration control of a piezolaminated semicircular cylindrical shell is also studied.

The results of the finite element analysis are used to design a linear quadratic regulator (LQR) controller and a linear quadratic Gaussian (LQG) compensator with a dynamic state observer to achieve all the controls. The control design begins with an approximate reduced modal model which can represent the system dynamics with the least system modes. A state space modal model of the smart structure which integrates the host structure with bonded piezoelectric sensors and actuators, is then used to design the control system. The designed LQR/LQG feedback controls are shown to be successful in suppressing the vibration and stabilizing the buckling modes of structures.

Both the finite element analysis and the active control simulation results are consistent with the existing theoretical analysis results and the experimental data in the literature. Some important conclusions and interesting observations are obtained.

ABRÉGÉ

L'objectif de cette thése est le contrôle de la vibration et de flambage à l'aide de l'analyse par éléments finis et LQR/LQG technologies de contrôle de rétroaction pour les structures composites stratifiées piézo-électriques qui sont liés ou incorporés de surface de capteurs et d'actionneurs piézoélectriques.

Il ya principalement deux parties ciblées.

La partie des éléments finis:

Deux formulations éléments finis pour les poutres laminées piézo-basé sur le classique d'Euler-Bernoulli et la théorie des poutres de Timoshenko, respectivement, linéaires couplées piézoélectriques équations constitutives, et le principe de variation de Hamilton sont développés. Un C0 continue, cisaillement flexible, à huit nuds élément de coque à double courbure sérendipité pour les plaques piézo-composites stratifiés et de coquillages est également dérivée basée sur la théorie de la couche-sage déformation de cisaillement, linéaires piézo-électriques couplés relations constitutives mécaniques, et le principe de variation de Hamilton.

Toute la poutre, plaque, et des éléments de coque développés ont considéré la rigidité, de masse et les effets de couplage électromécanique du capteur piézoélectrique et les couches de l'actionneur. Les éléments de structure développés sont capables de traiter les effets non linéaires de déformation en cisaillement transversal et la non-linéarité des matériaux composites, piézoélectrique-mécanique d'accouplement, et peut prévoir plus précisément les modes supérieurs de vibration, et peut être appliquée à partir de minces d'épaisseur moyenne structures

composites multicouches. Ils sont évalués à la fois les vibrations et analyse de flambage de la poutre, plaque, et structures en coque.

La partie de commande actif:

La vibration de supprimer d'un porte à faux piézo-collé poutre, les deux premiers modes de flambement contrôle d'un appui simple piézo-collé poutre, et la vibration et le flambage contrôle de la charge d'un cantilever piézoélectrique stratifié plaque composite sont étudiés. Les résultats de l'analyse par éléments finis sont utilisés pour concevoir un régulateur linéaire quadratique (LQR) contrôleur et un linéaire quadratique gaussienne (LQG) compensateur avec un observateur d'état dynamique pour atteindre toutes les commandes.

Les conceptions de commandes commencent par une méthode modale modle pour déterminer un modle modal réduit approximative qui peut représenter la dynamique du systme avec les modes les moins systme inclus. Un modle modal espace d'état de la structure intelligente qui a intégré la structure d'accueil d'collés capteurs et d'actionneurs piézoélectriques, est ensuite utilisé pour concevoir le systme de contrôle. Les contrôles visant commentaires LQR/LQG sont avérés succs dans la suppression de la vibration et de stabiliser les modes de flambement des structures.

Tant l'analyse par éléments finis et les résultats de simulation de contrôle actives sont compatibles avec les résultats existants d'analyse théoriques et les données expérimentales de la littérature. Quelques conclusions importantes et des observations intéressantes sont obtenues.

STATEMENT OF ORIGINALITY

To the author's best knowledge, the results contained in this thesis are original.

The C^0 continuous, shear flexible, eight-node serendipity doubly curved shell element based on the layer-wise shear deformation theory is developed and programmed (using the Matlab software) by the author for the first time.

The developed element is used for active vibration and buckling control applications of piezolaminated smart beams, plates and shells. The mainly new contributions are:

1. Active control of the first two buckling modes of a simply-supported piezolaminated beam.
2. Active control of the first buckling mode of a cantilevered piezolaminated composite plate.
3. The comparison of the vibration control of a cantilever piezolaminated beam with its experimental results in the literature.
4. The comparison of the vibration control of a cantilever piezolaminated composite plate with other known finite element analysis results.
5. The comparison of the vibration control of a piezolaminated semicircular cylindrical shell with other known finite element analysis results.

TABLE OF CONTENTS

LIST OF TABLES

LIST OF FIGURES

CHAPTER 1
Introduction and Overview

1.1 Background

1.1.1 Smart Structures and Applications

In modern engineering, smart structures have become an important research topic and a new generation of engineering components have evolved. Srinivasan & McFarland, in [1], defined smart structures as “the integration of actuators, sensors, and controls with a material or structural component” or “material systems that have intelligence and life features integrated in the microstructure of the material system to reduce mass and energy and produce adaptive functionality”. The smart structure is a concept that borrows directly from the biological world. Like the natural growth of the biological structures in the living world, smart structures are able to respond to their environment and modify themselves to cater for the new demands and requirements. This “smart” or “intelligent” feature is conveyed in the book title “Smart Structures — Blurring the Distinction Between the Living and the Nonliving” written by V.K.Wadhawan [2]. It is the origin of my inspiration to do this “smart” research.

The evolutionary path of smart structures can be written in the following sequence (see Wadhawan [2]):

- Actively smart structures (sensor+feedback+enhanced actuator action+other biomimetic features)
- Intelligent structures (actively smart structures+learning feature or cortical-like intelligence)
- Wise structures (capable of taking moral and ethical decision)
- Collective intelligence (like the internet)
- Man-machine integration

This dissertation will deal with the very beginning of the subject: Actively controlled structures (or smart structures), which have a high degree of integration of the sensor, actuation, and control functions embedded in a distributed or hierarchic manner. The integrated or embedded structural configurations in this research are the laminated composite beams, plates, and shells bonded or embedded with segmented or distributed piezoelectric layers as sensors and actuators and microprocessors as controllers.

There are numerous applications of smart structures in different industries. These include aerospace and aviation, biomedical services, civil engineering, mechanical systems with various utilization possibilities in vibration and noise control, buckling instability control, precision position and shape control, non-destructive testing and structure health monitoring to identify damaged components, structural fatigue life extending technology, etc.

1.1.2 Piezoelectric Materials

Piezoelectrics are the most popular smart materials. They belong to a class of dielectrics which undergo deformation in response to an applied electric field (converse piezoelectric effect) and produce voltage in response to mechanical strains (direct piezoelectric effect). They are relatively linear at low fields and bipolar, but exhibit hysteresis.

PZT (Lead Zirconate Titanate) is the best known piezoceramic material. PVDF (Poly Vinylidene Fluoride) is a commonly used polymer piezofilm material. They are in the form of thin wafers which can be readily bonded or embedded in laminated composite structures. Piezoelectrics do not have piezoelectric characteristics in their original state. Piezoelectric effects are induced through poling by the application of large DC electric fields at a high temperature. Poled piezoelectrics exhibit both direct and converse piezoelectric effects and can be used as sensors and actuators.

1.1.3 Sensors, Actuators, and Controllers

Sensors are acting like the nerves of a living system. They can convert structure strains, displacements, or their time derivatives into an electric field and form a data acquisition system for the host structure (the body of living system). Key factors for sensors are their sensitivity to strain or displacement, bandwidth, and size. Typical sensors consist of strain gauges, accelerometers, fiber opticals, piezofilms, and piezoceramics. PVDF is most commonly used as piezoelectric strain sensors with 10000 V per strain sensitivity and low stiffness.

Actuators are like the muscles of a living system. They normally convert electric inputs into actuation strain or displacement that is transmitted to the host structure (the body) modifying its mechanical state. Important performance parameters for actuators are maximum stroke or induced strain, stiffness, and bandwidth. PZT and PVDF are the commonly used piezoelectric actuators with maximum induced strain of about 1000 microstrain and 700 microstrain respectively.

Controllers are like the brain of a living system. They are designed to analyze the response from the sensors and use the integrated control theory to command the actuators to apply strains/displacements to alter system response. The active control algorithms for smart structures include feedback, neural network, and fuzzy logic.

1.1.4 Induced Strain Actuator

The total strain in the actuator is the sum of the mechanical strain caused by the stress plus the induced strain caused by the electric field. The strain in the host structure is obtained by establishing the displacement compatibility between the host and the actuators.

An opposite electric field is applied along the poling axis which induces the actuators bonded with the structure to expand or contract. For the extension mode actuator, the poling direction is the Z-axis.

1.2 Literature Review

1.2.1 Finite Element Modeling of Piezoelectric Coupled Field

In the literature, modeling of embedded or bonded piezoelectric laminar sensors/actuators, and the finite element method (FEM) implementation of coupled field problems with such components have been addressed by many authors.

Generally, piezoelectric elements are used in pairs, one on each side of a structural plane. A classic configuration for a smart structure is a master structure sandwiched between two piezoelectric thin layers acting as a distributed sensor and actuator respectively. Both bonded and embedded piezoelectric sensors and actuators result in a laminated layer. Layer-wise finite elements for the multilayered composite structure should therefore be established.

Sunar & Rao [3] derived a finite element formulation of thermo-piezoelectric problems starting from linear thermo-piezoelectric constitutive equations and Hamilton's principle. Suleman & Venkayya [4] proposed a 4-node plate element using the Mindlin assumption to accommodate thick/thin plates and shells, with each node possessing 3-translational and 3-rotational degrees of freedom (DOF). In addition, the element has one electrical degree of freedom per piezoelectric layer (voltage varying linearly across the thickness). It uses a reduced integration scheme for the transverse shear stiffness to avoid the shear locking phenomenon. The experimental work of Crawley and Anderson [5] showed a nonlinear relationship between the applied voltage and the normal strain induced in an unconstrained PZT plate for electric fields exceeding 100 V/mm. Yang and Batra [6] presented a second-order theory (with quadratic relations of strain and electric fields) and nonlinear constitutive equations for piezoelectric materials. Adequate modeling of the effects of the application of large electric fields to the piezoelectric layers requires improved finite elements. Kusculuoglu and Royston [7] developed a 4-node Lagrange bilinear and an 8-node serendipity quadratic element using Mindlin plate shear deformation theory for each layer of composite plates.

A constraining matrix for enforcing shear continuity between the layers has also been introduced in their work. Polit and Bruant [8] presented an 8-node plate element based on the Mindlin first order shear deformation theory. The electric potential is approximated using the layer-wise approach: both a linear variation and a quadratic variation with respect to the thickness coordinate in each layer. Thornburgh and Chattopadhyay [9] reported high-order models for the behavior of piezo-laminated plates using nonlinear piezoelectric terms. Pai et al. [10] reported an uncoupled induced-strain geometric nonlinearity theory for the dynamics and active control of piezoelectric plates. Varelis and Saravanos [11] developed an 8-node parabolic plate element that includes nonlinear effects due to large displacements and rotations. An incremental-iterative solution is formulated for the analysis of coupled nonlinear piezo-laminated plates.

Tzou [12] proposed a generic theory for the intelligent shell system. Iozzi and Gaudenzi [13] developed a four node shear deformable shell element for adaptive piezo-laminated structures. Pinto Correia et al. [14] presented a shell conical panel element. A mixed laminated theory is used which combines an equivalent single layer higher order shear deformation with a layer-wise representation for the electric potential through each piezoelectric layer.

A survey of the available beam/plate/shell elements for piezoelectric coupled field problems has been given in Saravanos and Heyliger [15] and Benjeddou [16].

1.2.2 Enhancement of Buckling Load of Piezo-laminated Structures

In this work, we will investigate the use of the two best known piezoelectric materials, PZT (Lead Zirconate Titanate) piezoceramic and PVDF (PolyVinylidene Flouride Film) piezo-polymer in enhancing the buckling load of structures. The following are some of the important previous works on this research topic.

Chandrashekhara and Bhatia [17] used the first-order shear deformation theory, linear kinematics, and linear constitutive relations for the PZT and plate material. Their FEM results computed for a square thin plate with the length/thickness ratio of 100 showed that the actuation of the PZT elements can increase the buckling load. Thompson and Laughlan [18] experimentally showed that the buckling load of graphite-epoxy strips can be increased from 19.8% to 37.1% by using PZT actuators. Meressi and Paden [19] analytically proved that PVDF actuators mounted continuously along the length of a column could be used to stabilize the first mode of the column.

Cui et al [20] defined the dynamic buckling load of a rectangular elastic-plastic plate as the one for which the slope of the deflection vs. the load curve suddenly increased. Varelis and Saravanos [21] incorporated nonlinear effects due to large rotations to predict the buckling and post-buckling response of adaptive composite beams and plates. Batra and Geng [22] employed second-order constitutive equations to enhance the dynamic buckling load. They showed that PZT elements bonded to the top and the bottom of a graphite-epoxy rectangular plate when suitably activated can enhance the buckling load by 58.5%.

1.2.3 Active Control Systems, Algorithms, and Controllers

Active control systems use sensors and actuators to activate the application of forces on a structure. A control system usually has input and output to the system; when the output of the system is fed back into the system as part of its input, it is called the "feedback" which is used to adjust controller parameters. Many authors have proposed different optimal feedback control algorithms and systems for piezoelectric laminated structures.

For the feedback active control system, a linear quadratic regulator (LQR) is one of the powerful optimization routines, which can be used to optimize the feedback parameters. LQR controller is an optimal control theory based on full state feedback assuming that all the information is available without any consideration for state estimation. It's difficult and sometimes impossible to measure the whole states of the system. Then an observer or state estimator has to be designed to estimate the state based solely on the measured output. A linear quadratic Gaussian (LQG) compensator is the combination of the LQR controller and the observer to be able to compensate the measurement noise of the sensor output and the environment disturbances of the system dynamics. Other powerful tools for control design are the system norms such as H_2, H_∞, and Hankel. They are the measures of intensity of the system response to standard excitations.

Law and Huang [23], Balamurugan and Narayanan [24], and Narayanan and Balamurugan [25] presented finite element modeling for beams, plates, and shells and applied the LQR for active vibration control of smart laminated structures. Bhattacharya et al. [26] adopted an Independent Modal Space Control (IMSC) based LQR control methodology for the active vibration control of laminated spherical shells with different fiber orientation and varying radii of curvature. Meressi and Paden [19] used the LQR to stabilize the first buckling mode and increase the column critical buckling load by 3.8 times. Han and Lee [27] worked on vibration control of a thin plate using the LQG algorithm.

Proportional-integral-derivative (PID) is the most common general-purpose controller; see Goodwin et al. [28]. Chandrashekhara and Bhatia [17] demonstrated a proportional control algorithm where the forces induced by actuators under the applied voltage are optimized to enhance buckling loads; the sensor output is used to determine the input to the actuator. Petersen et al. [29] used H_∞ norm in a robust control design.

1.2.4 Conclusions from the Literature Review

From the above literature reviews, it is clear that many researchers have proposed different nonlinear analytical models and finite element formulations on piezoelectric structures analysis and design. However, the following points are noted.

1. Most of these models are limited to piezoelectric actuators or mechanical structures. Finite element modeling and optimal active control of nonlinear coupled systems with host structures is studied by only a few researchers.
2. There is a marked absence of papers about active buckling control of plates and shells. The present research is mainly concentrated on active vibration control of smart beams and plates.

3. For the active buckling control of smart beams, most of the research uses linear kinematics, linear constitutive relations, and the classical plate theory. For a large electric field drive problem and active control of higher buckling modes, the second order nonlinear constitutive model, the quadratic through the thickness electric field, large strains, and shear strains effects have to be studied.

In conclusion, solid understanding of the nonlinearities and the ability of simulating them will lead to improved, and robust efficient system actuation and monitoring. We must consider these mechanical nonlinearities and piezoelectric-mechanical coupling effects in sensor/actuator modeling, finite element simulation, and active optimal control design, especially in choosing the control algorithms and strategies related to the coupled field piezoelectric structures.

1.3 Objectives of the Research

This dissertation is intended to improve the vibration and buckling control of the piezoelectric laminated composite structures by using the finite element analysis and modern control technologies.

Based on the discussions in the background and literature review sections, the author would like to focus on the following special objectives and scope:

Active vibration and buckling control of piezoelectric laminated beams. By applying finite element analysis (FEA), approximate reduced modal models are built by including the first two vibration modes and the first six vibration modes. Then, by applying optimal feedback control strategies (LQR/LQG), the vibration of a cantilevered piezoelectric laminated beam will be controlled. As well, the first two buckling modes of a simply supported piezoelectric laminated beam will be stabilized. Two finite element formulations based on the classical Euler-Bernoulli and the Timoshenko beam theories and linear coupled piezoelectric constitutive equations will be developed and evaluated. The results of the FEA will then be used to design LQR/LQG compensators to achieve the control. The difference between vibration suppressing and buckling stabilizing will be illustrated. Also the optimal locations of segmented actuator pairs and sensors along the beams will be explained for the more effective control.

For active vibration and buckling control of piezoelectric laminated composite plates and shells, the following will be done. By using the Layer-Wise Shear Deformation Theory (LWSDT), a doubly curved piezo-laminated composite shell element will be developed. The developed element will be able to handle the nonlinear effects of transverse shear strain and composite materials, piezoelectric-mechanical coupling, and predict more precisely the higher modes of vibration for thin to medium-thick multilayered composite structures. The LQG feedback control will then be designed in conjunction with the FEA results to achieve the active vibration and buckling controls.

Briefly the main objectives of the dissertation are as follows:

- Develop two coupled piezoelectric laminated beam elements and compare their FEA results and active control applications.
- Optimize the locations of segmented piezoelectric sensors and actuators for the effective control.

- Design LQR/LQG feedback controls to stabilize the first two buckling modes of piezoelectric laminated beams.
- Adapt the LWSDT theory to develop a coupled curvilinear piezoelectric laminated composite shell element.
- Determine the approximate reduced modal model that will represent the system dynamics with the least system modes included.
- Design LQR/LQG feedback control to suppress the vibration and stabilize the buckling modes of plates and shells.

1.4 Organization of the Dissertation

The dissertation includes six chapters. Chapter 1 offers a number of background topics and reviews so as to lead to the motivations and objectives of the research. Chapter 2 introduces mathematical models and finite element models of piezoelectric structures. By using the Hamilton's principle, displacement-strain relations are combined with material constitutive equations, compatibility equations, and stress equations of equilibrium to derive the dynamic governing equations of piezoelectric laminated structures. Chapter 3 describes the active control design. These two chapters are devoted mainly to the theoretical basis of the study on which the following chapters dealing with the applications are built. Chapters 4 and 5 introduce appropriate beam, plate, and shell theory, including transverse shear deformation effects, layer-wise composite material nonlinearity, and piezoelectric-mechanical coupling to form the system control equations and derive the reduced modal model to achieve the active controls. Chapter 4 deals mainly with the developing of piezoelectric beam elements and vibration and buckling control applications. Chapter 5 deals with the developing of piezoelectric composite plate/shell element and corresponding vibration and buckling control applications. Chapter 6 is the conclusion chapter and it summarizes the contributions of the dissertation.

CHAPTER 2

Mathematical and Finite Element Models of Piezolaminated Structures

2.1 Summary

First, the governing dynamic equations of a piezoelectric continuum are derived from the Hamilton's principle. These equations take into account the mass and stiffness of the piezoelectric patches. By applying finite element modeling and modal analysis techniques, finite element governing equations are then established and transformed to the modal space.

The developed finite element has only considered the elastic degrees of freedom and does not introduce voltage, electric charge or other electrical degrees of freedom as additional ones. It is assumed that the electric field and electric displacement across the thickness is uniform and aligned with the normal to the mid-plane of the piezo layer. Thus the applied actuator voltage and also the capacitance effect are considered constant throughout the piezo-layers.

2.2 Piezoelectric-Mechanical Constitutive Equations

According to the *IEEE standard on piezoelectricity* [30], linear piezoelectric constitutive equations can be written in the form of coupled actuator and sensor equations.

Actuator equation

$$\{\sigma\} = [c^E]\{\varepsilon\} - [e]^T\{E\} \tag{2.1}$$

Sensor equation

$$\{D\} = [e]\{\varepsilon\} + [\epsilon^{\varepsilon}]\{E\} \tag{2.2}$$

Alternative forms depending on the type of independant variables and constants are

$$\{\varepsilon\} = [s^E]\{\sigma\} + [d]^T\{E\} \tag{2.3}$$

$$\{D\} = [d]\{\sigma\} + [\epsilon^{\sigma}]\{E\} \tag{2.4}$$

$$\{\varepsilon\} = [s^D]\{\sigma\} + [g]^T\{D\} \tag{2.5}$$

$$\{E\} = -[g]\{\sigma\} + [\beta^{\sigma}]\{D\} \tag{2.6}$$

$$\{\sigma\} = [c^D]\{\varepsilon\} - [h]^T\{D\} \tag{2.7}$$

$$\{E\} = -[h]\{\varepsilon\} + [\beta^{\varepsilon}]\{D\} \tag{2.8}$$

in which $\{\sigma\} = (\sigma_{xx}, \sigma_{yy}, \sigma_{zz}, \sigma_{yz}, \sigma_{xz}, \sigma_{xy})^T$, $\{\varepsilon\} = (\varepsilon_{xx}, \varepsilon_{yy}, \varepsilon_{zz}, \varepsilon_{yz}, \varepsilon_{xz}, \varepsilon_{xy})^T$, $\{E\}$, and $\{D\}$ are the stress, strain, electric field, and electric displacement vectors respectively; $[c]$ and $[s]$ are the elastic stiffness and compliance matrices; $[\epsilon]$ and $[\beta]$ are the dielectric constant matrices; $[e]$, $[d]$, $[g]$, and $[h]$ are the matrices of the piezoelectric constants; the superscripts E, σ, D, and ε mean that the values of the constants matrices are evaluated at constant E, σ, D, and ε respectively. The matrix superscript T indicates the matrix transpose.

In the following derivation, the $h-$type equation (2.7) will be chosen as the actuator equation and the $g-$type equation (2.6) will be chosen as the sensor equation. Also the following verified relations between elastic and piezoelectric constants will be used:

$$[c^D][s^D] = I_{6\times6} \tag{2.9}$$

$$[g] = [h][s^D] \tag{2.10}$$

2.3 Variational Principle

According to the Hamilton's principle, for an undamped conservative system, the governing dynamic equations of a piezoelectric continuum are obtainable from

$$\delta \int_{t_1}^{t_2} (L + W_d)dt = 0 \tag{2.11}$$

with

$$L = \int_V (J - H)dV \tag{2.12}$$

$$J = \frac{1}{2}\rho\{\dot{u}\}^T\{\dot{u}\} \tag{2.13}$$

$$W_d = \int_V \{u\}^T\{F_V\}dV + \int_S \{u\}^T\{F_S\}dS + \{u\}^T\{F_P\} - Q_{pz}\Phi_{pz} \tag{2.14}$$

where t_1 and t_2 are the starting and ending time, V is the body volume, L is the Lagrangian, J is the kinetic energy density, H is the electrical enthalpy density, W_d is the work of external disturbance mechanical forces and the applied electrical potential; $\{u\}$ and $\{\dot{u}\}$ are the generalized displacement field and velocity field respectively; a dot above a variable denotes its time derivative; $\{F_V\}$, $\{F_S\}$, and $\{F_P\}$ are the body forces, the surface forces applied on the surface S, and the concentrated load vector respectively; Φ_{pz}, Q_{pz}, and ρ are the external voltage applied to the piezo wafer, the electric charge of piezo patches, and the mass density respectively.

According to the linear piezoelectric theory (see the *IEEE standard* [30]), H can be written as

$$H = \frac{1}{2}[\{\varepsilon\}^T\{\sigma\} - \{D\}^T\{E\}] \tag{2.15}$$

Substituting the constitutive equations (2.7) and (2.6) into H and using the relations (2.9) and (2.10), then substituting the H and J into L, the Hamilton's principle (2.11) yields

$$\delta \int_{t_1}^{t_2} (T_k - U_\varepsilon - U_{pe} - U_{pc} + W_d)dt = 0 \tag{2.16}$$

T_k is the kinetic energy, U_ε is the mechanical strain potential energy, U_{pe} is the electric potential energy of the piezo layers, and U_{pc} is the mechanical-electrical coupled potential energy of the piezo layer.

These energy terms can be written as

$$T_k = \int_V JdV = \int_V \frac{1}{2}\rho\{\dot{u}\}^T\{\dot{u}\}dV \tag{2.17}$$

$$U_\varepsilon = \int_V \frac{1}{2}\{\varepsilon\}^T[c^D]\{\varepsilon\}dV \tag{2.18}$$

$$U_{pe} = \int_V -\frac{1}{2}\{D^T\}([g][h]^T + [\beta^T])\{D\}dV \tag{2.19}$$

$$U_{pc} = \int_V -\frac{1}{2}[\{\varepsilon\}^T[h]^T\{D\} - \{D\}^T[h]\{\varepsilon\}]dV \tag{2.20}$$

The variation of kinetic energy term of equation (2.16) can be integrated by parts over the time interval as

$$\int_{t_1}^{t_2} \delta Jdt = \int_{t_1}^{t_2} \rho\{\delta\dot{u}\}^T\{\dot{u}\}dt = [\rho\{\delta u\}^T\{\dot{u}\}]_{t_1}^{t_2} - \int_{t_1}^{t_2} \rho\{\delta u\}^T\{\ddot{u}\}dt \tag{2.21}$$

in which the first term vanishes as δu being equal to zero at $t = t_1$ and $t = t_2$.

After taking the variation of all the terms in equation (2.16), one gets

$$
\begin{aligned}
&-\int_V [\rho\{\delta u\}^T\{\ddot{u}\} + \{\delta\varepsilon\}^T[c^D]\{\varepsilon\} - \{\delta\varepsilon\}^T[h]^T\{D\} \\
&+\{\delta D\}^T[h]\{\varepsilon\} - \{\delta D\}^T([g][h]^T + [\beta^T])\{D\} - \{\delta u\}^T\{F_V\}]dV \\
&+\int_S \{\delta u\}^T\{F_S\}dS + \{\delta u\}^T\{F_P\} - \delta Q_{pz}\Phi_{pz} = 0
\end{aligned} \tag{2.22}
$$

2.4 Finite Element Model of Piezoelectric Laminated Structures

The element generalized displacements field $u(X,t)$ can be defined by the shape functions as

$$\{u(X,t)\} = [N_u(X)]\{u_i(t)\} \tag{2.23}$$

The element electric displacement of piezo layer $D^e(X,t)$ is defined by the element electric charge of piezo layer $Q^e(X,t)$ as

$$\{D^e_{pz}(X,t)\} = -\{Q^e_{pz}(X,t)/S^e_{pz}\} \tag{2.24}$$

where X and t are the position and time coordinates, S^e_{pz} is the element area of the effective surface electrode which is assumed as the entire piezoelectric patch, the upper index e denotes an element, the lower indices pz denotes the piezo layer, $u_i(t)$ is the corresponding element node displacement value, $[N_u(X)]$ are the shape functions. Later, these X and t variables are not explicitly written for simplicity.

As charge is collected only in the normal of the mid-plane of piezo-layers or the thickness direction, only D_3 is of interest:

$$\{D^e_3\} = -\{Q^e_{pz}/S^e_{pz}\} \tag{2.25}$$

The strain field ε can be derived as

$$\{\varepsilon\} = [\partial]\{u\} = [\partial][N_u]\{u_i\} = [B_u(X)]\{u_i(t)\} \tag{2.26}$$

where $[\partial]$ is the derivative operator matrix

$$[\partial] = \begin{bmatrix} \frac{\partial}{\partial x} & 0 & 0 \\ 0 & \frac{\partial}{\partial y} & 0 \\ 0 & 0 & \frac{\partial}{\partial z} \\ 0 & \frac{\partial}{\partial z} & \frac{\partial}{\partial y} \\ \frac{\partial}{\partial z} & 0 & \frac{\partial}{\partial x} \\ \frac{\partial}{\partial y} & \frac{\partial}{\partial x} & 0 \end{bmatrix} \tag{2.27}$$

Substituting these displacement, strain and electric displacement expressions into the variational equations (2.22) and since the variations δu_i and δQ_{pz}^e are arbitrary, the following finite element equations can be established from the variational principle

$$[M^e]\{\ddot{u}_i\} + [K_{uu}^e]\{u_i\} + [K_{uQ}^e]\{Q_{pz}^e\} = \{f_i^e\} \tag{2.28}$$

$$[K_{Qu}^e]\{u_i\} + [K_{QQ}^e]\{Q_{pz}^e\} = \{\Phi_{pz}^e\} \tag{2.29}$$

in which

$$[M^e] = \int_V \rho[N_u]^T[N_u]dV \tag{2.30}$$

$$[K_{uu}^e] = \int_V [B_u]^T[c^D][B_u]dV \tag{2.31}$$

$$[K_{uQ}^e] = \int_V \frac{1}{S_{pz}^e}[B_u]^T[h]^T dV \tag{2.32}$$

$$[K_{QQ}^e] = \frac{h_{pz}^e}{S_{pz}^e}([g][h]^T + [\beta^T]) \tag{2.33}$$

$$[K_{Qu}^e] = [K_{uQ}^e]^T \tag{2.34}$$

$$\{f_i^e\} = \int_V [N_u]^T\{F_V\}dV + \int_S [N_u]^T\{F_S\}dS + [N_u]^T\{F_P\} \tag{2.35}$$

are respectively the element mass, stiffness, piezoelectric coupling, and capacitance matrices as well as the external mechanical force vectors. $\{\Phi_{pz}^e\}$ is the element applied voltage to the piezo layer and h_{pz}^e is the thickness of the element piezo layer.

After introducing structural damping and assembling the element equations (2.28) and (2.29) for the whole structure, the global equations of dynamics governing the piezoelectric embedded structure system can be written as

$$[M]\{\ddot{U}\} + [C_d]\{\dot{U}\} + [K_{UU}]\{U\} + [K_{UQ}]\{Q_{pz}\} = \{F_M\} \tag{2.36}$$

$$[K_{QU}]\{U\} + [K_{QQ}]\{Q_{pz}\} = \{\Phi_{pz}\} \tag{2.37}$$

where $[M]$, $[K_{UU}]$, $[K_{UQ}]$, $[K_{QU}]$, $[K_{QQ}]$, $\{F_M\}$, and $\{\Phi_{pz}\}$ are the assembled global inertial mass matrix, mechanical stiffness matrix, electromechanical coupling matrix, electric capacitance matrix, external mechanical force vector and external voltage applied to the piezo layer. $\{U\}$ and $\{Q_{pz}\}$ are the global degrees of freedom of the mechanical variables and the electric charges of the piezo layer.

$[C_d]$ is the Rayleigh damping matrix, assumed to be a linear combination of the structural mass and stiffness as

$$[C_d] = a[M] + b[K_{UU}] \tag{2.38}$$

where a and b are the constants determined by the procedure given in [31].

2.5 Mathematical Model of Piezoelectric Laminated Structures

Piezoelectric smart structures are laminated composite composed of sensor layers, actuator layers, and nonpiezoelectric multi-base layers. For simplicity, a laminated rectangular plate/shell structure, with thickness configuration as shown in Figure 2–1 is used to build the mathematical model.

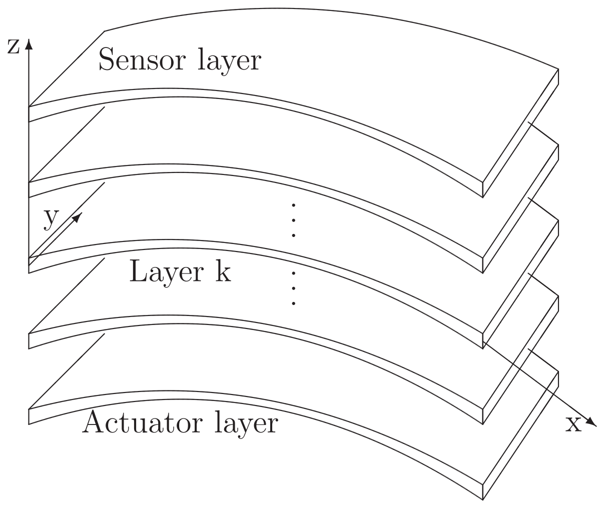

Figure 2–1: A laminated composite rectangular plate/shell configuration

Many composite materials are laminated structures or sandwich structures and composed of numerous laminae, which are bonded toghether. One of the major advantages that composites have over more conventional structures is the ability of stacking laminae to result in the optimum laminate material properties.

Generalized constitutive equations for one lamina of a composite material will first be formulated.

2.5.1 Constraining Equations

The classical, first order shear deformation or other theories of structure analysis utilize different strain-displacement relations to describe the displacements and strains of a laminated or sandwich composite structure. Because all of the individual laminae are bonded together, the same assumptions are made regarding the elements through the laminate thickness. A continuity of displacements and strains occurs across the laminated structure regardless of the orientation of individual laminae.

In order to satisfy the shear strain continuity for the laminae as well as to reduce the number of total system degrees of freedom, constraining equations are constructed, for simplicity, considering the neutral axis layer as the second layer. Thus, one writes:

$$\{\underline{q}\} = [C_q]\{q\} \tag{2.39}$$

$$\{\underline{q}\} = \{u^1, v^1, u^3, v^3, \cdots, u^k, v^k, \cdots, u^n, v^n\}^T \tag{2.40}$$

$$\{q\} = \{u^2, v^2, \phi_x^1, \phi_y^1, \phi_x^2, \phi_y^2, \cdots, \phi_x^k, \phi_y^k, \cdots, \phi_x^n, \phi_y^n, w\}^T \tag{2.41}$$

where u^k, v^k are the kth layer inplane displacements $(k = 1, n)$, w is the transverse displacement which is assumed to be uniform through the thickness, ϕ_x^k and ϕ_y^k are the rotations of transverse normals about the y and x axes in kth layer respectively.

$$[C_q] = \begin{bmatrix} 1 & 0 & -a_0 & 0 & -a_1 & 0 & 0 & 0 & 0 & 0 & 0 & 0 & 0 & 0 & 0 \\ 0 & 1 & 0 & -a_0 & 0 & -a_1 & 0 & 0 & 0 & 0 & 0 & 0 & 0 & 0 & 0 \\ 1 & 0 & 0 & 0 & a_2 - a_1 & 0 & a_3 & 0 & 0 & 0 & 0 & 0 & 0 & 0 & 0 \\ 0 & 1 & 0 & 0 & 0 & a_2 - a_1 & 0 & a_3 & 0 & 0 & 0 & 0 & 0 & 0 & 0 \\ 1 & 0 & 0 & 0 & a_2 - a_1 & 0 & a_4 & 0 & a_5 & 0 & 0 & 0 & 0 & 0 & 0 \\ 0 & 1 & 0 & 0 & 0 & a_2 - a_1 & 0 & a_4 & 0 & a_5 & 0 & 0 & 0 & 0 & 0 \\ \vdots & \vdots & \vdots & \vdots & \vdots & \vdots & \vdots & \vdots & \vdots & \vdots & \ddots & 0 & 0 & 0 & 0 \\ \vdots & \vdots & \vdots & \vdots & \vdots & \vdots & \vdots & \vdots & \vdots & \vdots & \vdots & \ddots & 0 & 0 & 0 \\ 1 & 0 & 0 & 0 & a_2 - a_1 & 0 & a_4 & 0 & a_6 & 0 & \cdots & \cdots & a_m & 0 & 0 \\ 0 & 1 & 0 & 0 & 0 & a_2 - a_1 & 0 & a_4 & 0 & a_6 & \cdots & \cdots & \cdots & a_m & 0 \end{bmatrix} \tag{2.42}$$

where $[C_q]$ represents the constraining matrix; $\underline{q}$ and q are the dependent and independent kinematic field variables vector of the problem, respectively; the constants are,

$$\begin{cases} m = \quad odd & \rightarrow \quad a_m = -\frac{h_k}{2} \quad k = floor(\frac{m}{2}) + 2 \\ m = \quad even & \rightarrow \quad a_m = -h_k \quad k = floor(\frac{m}{2}) + 1 \\ m = \quad 0 & \rightarrow \quad a_0 = -\frac{h_1}{2} \end{cases}$$

n is the total number of layers, h_1, h_k are the thickness of the first and the kth layer respectively. It should be noticed that constraining equation 2.39 is derived by assuming the midplane layer is the second layer. Otherwise, the constraining matrix $[C_q]$ has to be rearranged correspondingly.

2.5.2 Laminated Composite Constitutive Relations

Piezoelectric composite structures can be modeled as a laminate made of laminae stacked together at various orientations with differing material properties in each lamina, see Figure 2–2.

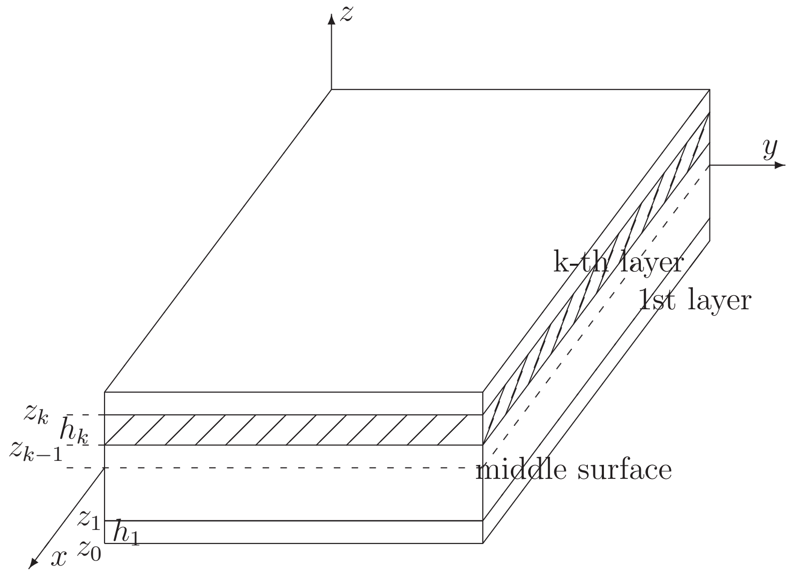

Figure 2–2: Laminate with coordinate notation of individual layers

For the k-th orthotropic lamina of the laminated composite plate and shell structure, with little loss in numerical accuracy, simpler forms [32] (under the hypothesis $\sigma_3 = \epsilon_3 = 0$ and taking into account shear strains and stresses) of the stress-strain relations in the material principal coordinates $(1, 2)$ can be defined as

$$\begin{Bmatrix} \sigma_1^k \\ \sigma_2^k \\ \sigma_3^k \\ \sigma_4^k \\ \sigma_5^k \\ \sigma_6^k \end{Bmatrix} = \begin{Bmatrix} \sigma_{11}^k \\ \sigma_{22}^k \\ \sigma_{33}^k \\ \tau_{23}^k \\ \tau_{31}^k \\ \tau_{12}^k \end{Bmatrix} = \begin{bmatrix} c_{11}^k & c_{12}^k & 0 & 0 & 0 & 0 \\ c_{21}^k & c_{22}^k & 0 & 0 & 0 & 0 \\ 0 & 0 & c_{33}^k & 0 & 0 & 0 \\ 0 & 0 & 0 & c_{44}^k & 0 & 0 \\ 0 & 0 & 0 & 0 & c_{55}^k & 0 \\ 0 & 0 & 0 & 0 & 0 & c_{66}^k \end{bmatrix} \begin{Bmatrix} \epsilon_{11}^k(=\epsilon_1^k) \\ \epsilon_{22}^k(=\epsilon_2^k) \\ \epsilon_{33}^k(=\epsilon_3^k) \\ 2\epsilon_{23}^k(=\epsilon_4^k) \\ 2\epsilon_{31}^k(=\epsilon_5^k) \\ 2\epsilon_{12}^k(=\epsilon_6^k) \end{Bmatrix} \tag{2.43}$$

where the constants are, $c_{11}^k = \frac{E_1^k}{1-\nu_{12}\nu_{21}}$, $c_{22}^k = \frac{E_2^k}{1-\nu_{12}^k\nu_{21}^k}$, $c_{33}^k = 0$, $c_{12}^k = \nu_{21}c_{11}^k$, $c_{21}^k = \nu_{12}c_{22}^k$,$c_{44}^k = G_{23}^k$, $c_{55}^k = G_{31}^k$, $c_{66}^k = G_{12}^k$, and $\nu_{ij}^k E_j^k = \nu_{ji}^k E_i^k (i, j = 1, 2)$. It should be noted that ϵ_4^k, ϵ_5^k, and ϵ_6^k are not tensor quantities, but they are widely used in composite analyses.

In short form,

$$\left\{\sigma^k\right\} = \left[C^k\right]\left\{\epsilon^k\right\} \tag{2.44}$$

Usually, the lamina material axes $(1, 2)$ do not coincide with the reference axes (x, y), as shown in Figure 2–3. The stress and strains on material and reference axes are related as

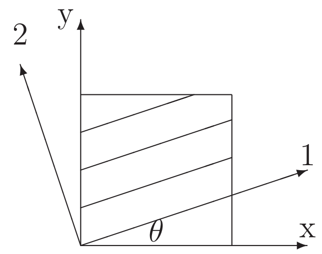

Figure 2–3: Lamina material and reference axes

$$\begin{Bmatrix} \sigma_1^k \\ \sigma_2^k \\ \sigma_3^k \\ \sigma_4^k \\ \sigma_5^k \\ \sigma_6^k \end{Bmatrix} = \left[T^k\right] \begin{Bmatrix} \sigma_{xx}^k \\ \sigma_{yy}^k \\ \sigma_{zz}^k \\ \sigma_{yz}^k \\ \sigma_{zx}^k \\ \sigma_{xy}^k \end{Bmatrix} \tag{2.45}$$

$$\begin{Bmatrix} \epsilon_1^k \\ \epsilon_2^k \\ \epsilon_3^k \\ \epsilon_4^k/2 \\ \epsilon_5^k/2 \\ \epsilon_6^k/2 \end{Bmatrix} = \left[T^k\right] \begin{Bmatrix} \epsilon_{xx}^k \\ \epsilon_{yy}^k \\ \epsilon_{zz}^k \\ \epsilon_{yz}^k \\ \epsilon_{zx}^k \\ \epsilon_{xy}^k \end{Bmatrix} \tag{2.46}$$

Here, it should be noticed that the coordinate transformations can be made only with tensor stresses and tensor strains. In equation (2.43), it is necessary to divide ϵ_4^k, ϵ_5^k, and ϵ_6^k by 2, where

$$\left[T^k\right] = \begin{bmatrix} m^2 & n^2 & 0 & 0 & 0 & 2mn \\ n^2 & m^2 & 0 & 0 & 0 & -2mn \\ 0 & 0 & 1 & 0 & 0 & 0 \\ 0 & 0 & 0 & m & -n & 0 \\ 0 & 0 & 0 & n & m & 0 \\ -mn & mn & 0 & 0 & 0 & (m^2 - n^2) \end{bmatrix} \tag{2.47}$$

where $m = cos\theta^k$ and $n = sin\theta^k$. The reverse transformations matrix $[T^k]^{-1}$ can be derived by substituting the $-\theta^k$ to the m and n.

Equation (2.43) can be transformed to the reference coordinates by using the equations 2.45 and 2.46.

$$\begin{Bmatrix} \sigma_{xx}^k \\ \sigma_{yy}^k \\ \sigma_{zz}^k \\ \sigma_{yz}^k \\ \sigma_{xz}^k \\ \sigma_{xy}^k \end{Bmatrix} = \begin{bmatrix} Q_{11}^k & Q_{12}^k & Q_{13}^k & 0 & 0 & Q_{16}^k \\ Q_{12}^k & Q_{22}^k & Q_{23}^k & 0 & 0 & Q_{26}^k \\ Q_{13}^k & Q_{23}^k & Q_{33}^k & 0 & 0 & Q_{36}^k \\ 0 & 0 & 0 & Q_{44}^k & Q_{45}^k & 0 \\ 0 & 0 & 0 & Q_{45}^k & Q_{55}^k & 0 \\ Q_{16}^k & Q_{26}^k & Q_{36}^k & 0 & 0 & Q_{66}^k \end{bmatrix} \begin{Bmatrix} \epsilon_{xx}^k \\ \epsilon_{yy}^k \\ \epsilon_{zz}^k \\ 2\epsilon_{yz}^k \\ 2\epsilon_{xz}^k \\ 2\epsilon_{xy}^k \end{Bmatrix} \tag{2.48}$$

or in the succinct notation:

$$\left\{\sigma^k\right\} = \left[Q^k\right]\left\{\epsilon^k\right\} \tag{2.49}$$

where $[Q^k] = [T^k]^{-1}[C^k][T^k]$.

Up to this point, the concentration has been on the stress-strain relations or the material constitutive matrix. Now the other three sets of equations comprising the equations of elasticity will be considered: the strain-displacement relations, the equilibrium equations and the compatibility equations.

The inclusion of transverse shear deformations in the structural behavior, usually results in an improved theory. For simplicity, the displacement field of the k^{th} layer lamina is based on the first-order shear deformation theory for the proposed element.

By the classical laminated composite structure theory, stress resultants N, stress couples M, and transverse shear resultants Q per unit width are defined for the overall structure regardless of the number and the orientation of the laminae as

$$(N_x, N_y, Q_y, Q_x, N_{xy}) = \int_{-h/2}^{h/2} (\sigma_{xx}, \sigma_{yy}, \tau_{yz}, \tau_{xz}, \tau_{xy}) dz \tag{2.50}$$

$$(M_x, M_y, M_{xy}) = \int_{-h/2}^{h/2} (\sigma_{xx}, \sigma_{yy}, \tau_{xy}) z dz \tag{2.51}$$

For a composite laminate of n layers with stacking angle $\theta_k (k = 1, n)$ and layer thickness $h_k (k = 1, n)$, the strain-displacement relations for small displacements assumption is

$$\{\epsilon\} = \left\{\epsilon^0\right\} + z\{\kappa\} \tag{2.52}$$

where the strain vector $\{\epsilon\} = \{\epsilon_{xx}, \epsilon_{yy}, \epsilon_{zz}, 2\epsilon_{yz}, 2\epsilon_{xz}, 2\epsilon_{xy}\}^T$, the strains of mid-surface $\{\epsilon^0\} = \left\{\epsilon^0_{xx}, \epsilon^0_{yy}, 0, 2\epsilon^0_{yz}, 2\epsilon^0_{xz}, 2\epsilon^0_{xy}\right\}^T$, and the curvatures $\{\kappa\} = \{\kappa_x, \kappa_y, 0, 0, 0, 2\kappa_{xy}\}^T$

Substituting equation (2.52) into equation (2.48), then into equation (2.50) and equation (2.51) results in:

$$\left\{\bar{N}\right\} = [\bar{D}]\{\bar{\epsilon}\} \tag{2.53}$$

where $\left\{\bar{N}\right\} = \{N_x, N_y, Q_y, Q_x, N_{xy}, M_x, M_y, M_{xy}\}^T$ is the laminate force and moment resultant corresponding to the mid-surface, the generalized strain vector of the mid-surface is $\{\bar{\epsilon}\} = \left\{\epsilon^0_{xx}, \epsilon^0_{yy}, 2\epsilon^0_{yz}, 2\epsilon^0_{xz}, 2\epsilon^0_{xy}, \kappa_x, \kappa_y, 2\kappa_{xy}\right\}^T$, and

$$[\bar{D}] = \begin{bmatrix} A_{11} & A_{12} & 0 & 0 & A_{16} & B_{11} & B_{12} & B_{16} \\ A_{12} & A_{22} & 0 & 0 & A_{26} & B_{12} & B_{22} & B_{26} \\ 0 & 0 & A_{44} & A_{45} & 0 & 0 & 0 & 0 \\ 0 & 0 & A_{45} & A_{55} & 0 & 0 & 0 & 0 \\ A_{16} & A_{26} & 0 & 0 & A_{66} & B_{16} & B_{26} & B_{66} \\ B_{11} & B_{12} & 0 & 0 & B_{16} & D_{11} & D_{12} & D_{16} \\ B_{12} & B_{22} & 0 & 0 & B_{26} & D_{12} & D_{22} & D_{26} \\ B_{16} & B_{26} & 0 & 0 & B_{66} & D_{16} & D_{26} & D_{66} \end{bmatrix} \quad (2.54)$$

where, the extensional, bending-stretching coupling, and flexural stiffness coefficient matrices of the laminate are

$$([A_{ij}], [B_{ij}], [D_{ij}]) = \sum_{k=1}^{n} \int_{z_{k-1}}^{z_k} [Q_{ij}]^k (1, z, z^2) dz \ (i, j, 1, 2, 6) \quad (2.55)$$

and the transverse shear stiffness coefficient matrix of the laminate is

$$[A_{ij}] = \sum_{k=1}^{n} \kappa^2 \int_{z_{k-1}}^{z_k} [Q_{ij}]^k dz \ (i, j, 4, 5) \quad (2.56)$$

in which the shear correction factor κ^2 is taken as $\frac{5}{6}$, see Reddy [33].

Since $[Q_{ij}]^k$ are not functions of z, they can be integrated explicitly [34]

$$[A_{ij}] = \sum_{k=1}^{n} [Q_{ij}]^k (z_k - z_{k-1}) \ (i, j, 1, 2, 6) \quad (2.57)$$

$$[B_{ij}] = \sum_{k=1}^{n} [Q_{ij}]^k (z_k^2 - z_{k-1}^2) \ (i, j, 1, 2, 6) \quad (2.58)$$

$$[D_{ij}] = \sum_{k=1}^{n} [Q_{ij}]^k (z_k^3 - z_{k-1}^3) \ (i, j, 1, 2, 6) \quad (2.59)$$

$$[A_{ij}] = \sum_{k=1}^{n} \kappa^2 [Q_{ij}]^k (z_k - z_{k-1}) \ (i, j, 4, 5) \tag{2.60}$$

2.5.3 System Governing Equations

Consider a general three layers piezoelectric structure with a non-piezoelectric base layer bonded with or embedded in colocated actuator and sensor layers as in Figure 2–4.

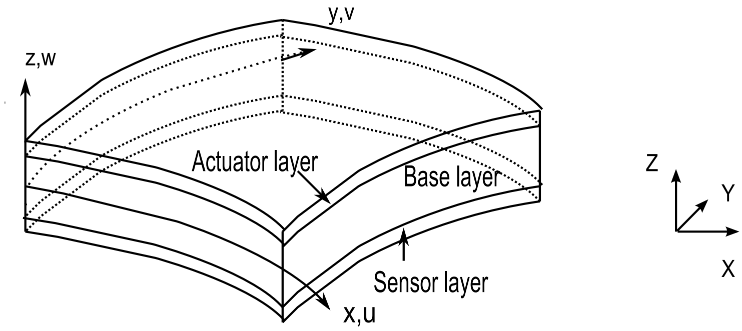

Figure 2–4: Piezolaminated composite shell configuration

Following the finite element formulation, both the equations of host structures with induced strain actuator layers and the sensor equations can be obtained.

For the sensor layer, charge sensing is considered. With zero voltage, from equation (2.37), the sensor electric charge $\{Q_s\}$ can be written as,

$$\{Q_s\} = -[K^s_{QQ}]^{-1}[K^s_{QU}]\{U\} \tag{2.61}$$

and it is called the sensor equation, which is the output of the dynamic system.

For the actuator layer, voltage actuation is considered. By imposing a voltage $\{\Phi_a\}$ on the actuator, from equation (2.37), the actuation charge $\{Q_a\}$ can be written as,

$$\{Q_a\} = [K^a_{QQ}]^{-1}(\{\Phi_a\} - [K^a_{QU}])\{U\} \tag{2.62}$$

Combining equations (2.36), (2.61), and (2.62), the global dynamic governing equations can be written as,

$$[M]\{\ddot{U}\} + [C_d]\{\dot{U}\} + [K^\star]\{U\} = \{F_M\} - [K^a]\{\Phi_a\} \tag{2.63}$$

in which

$$[K^\star] = [K_{UU}] - [K^s_{UQ}][K^s_{QQ}]^{-1}[K^s_{QU}] - [K^a_{UQ}][K^a_{QQ}]^{-1}[K^a_{QU}] \tag{2.64}$$

$$[K^a] = [K^a_{UQ}][K^a_{QQ}]^{-1} \tag{2.65}$$

2.6 Reduced-order modal model equations

The governing equations (2.63) are coupled dynamic system equations. They can be decoupled by the modal coordinates representation. Modal coordinates are defined through the displacements and velocities of structural (or natural) modes. Since these coordinates are linearly independent, they are often used in the dynamics analysis of complex structures modeled by finite elements to reduce the system order.

Modal models of structures or the modal coordinate representation can be obtained by the transformation of the previous nodal coordinates governing equations. This transformation can be derived by the mode superposition method, in which system modal matrix is used to transform the finite element nodal displacement vector to the modal coordinate vector. An approximate reduced-order model of the system in modal coordinates can then be obtained.

The generalized nodal displacement vector $\{U(t)\}$ can be approximated by:

$$\{U\left(t\right)\} \approx \sum_{i=1}^{n_m} \psi_i q_i\left(t\right) = [\Psi]\{q\left(t\right)\} \tag{2.66}$$

where $q_i(t)$ represents the modal amplitude of mode i. The mode shapes ψ_i and corresponding eigenfrequencies ω_i are the solutions of the eigenvalue problem of equation (2.63) with damping term neglected as

$$([K^\star] - \omega_i^2[M])\{q_i\} = 0 \tag{2.67}$$

$[\Psi]$ is the truncated modal shapes matrix. It can be given as:

$$[\Psi] = [\psi_1, \cdots, \psi_{n_m}] \qquad (n_m < n) \tag{2.68}$$

and $\{q(t)\}$ is the modal coordinates vector, which is a time dependent vector of order n_m; here n_m is the number of retained vibration modes or the number of modes to be controlled.

The dimension of the modal model is the most obvious advantage over the nodal model. The dimension of the modal representation is n_m, while the nodal representation is n, and typically we have $n_m << n$, i.e., the order of the model in modal coordinates is much lower than the model in nodal coordinates.

Another advantage of the models in modal coordinates is their definition of damping properties. While the mass and stiffness matrices are derived in the nodal coordinates from a finite-element model, the damping matrix is commonly not known, but is conveniently evaluated in the modal coordinates. Usually, the damping estimation is more accurate in modal coordinates.

By assuming that the system response is governed by the first n_m modes and using the modal coordinates $\{q(t)\}$ and equation (2.66), the system governing equations (2.63) and the sensor equation (2.61) can then be transformed to the reduced-order modal-space equations:

$$[\bar{M}]\{\ddot{q}\} + [\bar{C}_d]\{\dot{q}\} + [\bar{K}^\star]\{q\} = \{\bar{F}_M\} - [\bar{K}^a]\{\Phi_a\} \tag{2.69}$$

$$\{Q_s\} = -[K^s_{QQ}]^{-1}[K^s_{QU}][\Psi]\{q\} \tag{2.70}$$

$[\bar{M}] = [\Psi]^T[M][\Psi]$, $[\bar{C}_d] = [\Psi]^T[C_d][\Psi]$, $[\bar{K}^\star] = [\Psi]^T[K^\star][\Psi]$, $[\bar{K}^a] = [\Psi]^T[K^a]$, and $\{\bar{F}_M\} = [\Psi]^T\{F_M\}$ are the modal mass, modal damping, modal stiffness, modal actuator stiffness matrix, and external disturbing force vector, respectively.

Using the orthogonality properties of the mode shapes with respect to the mass and stiffness matrices

$$[\bar{M}] = [\Psi]^T[M][\Psi] = diag(m_i) \tag{2.71}$$

$$[\bar{K}^\star] = [\Psi]^T[K^\star][\Psi] = diag(m_i\omega_i^2) \tag{2.72}$$

A proportional damping is assumed

$$[\bar{C}_d] = [\Psi]^T[C_d][\Psi] = diag(2m_i\zeta_i\omega_i) \tag{2.73}$$

ζ_i $(i = 1, n_m)$ is the damping coefficient.

The modal system equation (2.69) can be normalized with respect to mass as

$$\{\ddot{q}\} + diag[2\zeta_i\omega_i]\{\dot{q}\} + diag[\omega_i^2]\{q\} = [\bar{M}]^{-1}\{\bar{F}_M\} - [\bar{M}]^{-1}[\bar{K}^a]\{\Phi_a\} \tag{2.74}$$

The system governing equations (2.63) are now decoupled into n_m equations corresponding to each individual mode and each mode corresponds to a natural frequency ω_i and a mode shape vector ψ_i $(i = 1, n_m)$.

The piezoelectric continuum linear decoupled dynamic system and sensor output equations in modal space form can be written as

$$\{\ddot{q}\} + diag[2\zeta_i\omega_i]\{\dot{q}\} + diag[\omega_i^2]\{q\} = [\bar{M}]^{-1}\{\bar{F}_M\} - [\bar{M}]^{-1}[\bar{K}^a]\{\Phi_a\} \tag{2.75}$$

$$\{Q_s\} = -[K^s_{QQ}]^{-1}[K^s_{QU}][\Psi]\{q\} \tag{2.76}$$

CHAPTER 3

Active Control Design Scheme of Piezoelectric Structures

3.1 Summary

A control system is an arrangement of physical components connected or related in such a manner as to command, regulate, direct, or govern itself or another system for providing a desired system response. A basic control system has an input, a process, and an output. The input and the output represent the desired response and the actual response respectively. In other words, a control system provides an output or response for a given input or stimulus. The basic objective of a control system is of regulating the value of some physical variable or causing that variable to change in a prescribed manner in time.

Control systems are typically classified as open-loop or closed-loop. Open-loop control systems do not monitor or correct the output for disturbances whereas closed-loop control systems do monitor the output and compare it with the input by adding a feedback loop, which measures a control variable and returns the output to influence it. In this chapter, an optimal LQR/LQG feedback closed-loop control system design scheme is presented for the active control of smart structures with piezoelectric sensors and actuators. By incorporating finite element analysis formulations, this control scheme will be carried out on different applications in the following chapters.

Most linear control system analyses and design methods are given in the state-space representation. The state-space standardization of structural models allows for the extension of known control system properties into structural dynamics. First, by introducing a state space variable, the structure system modal space equations can be written in state space form. Next, stability analysis of the closed-loop system is performed. Then, a Linear Quadratic Regulator (LQR) based on the full state feedback control law and a dynamic observer (Kalman filter) to estimate state variables based upon the sensor outputs are designed. Finally, a Linear Quadratic Gaussian (LQG) compensator is designed by combining the LQR controller with a state estimator. For simplicity, most of the matrix bracket-pairs symbols are dropped off in this chapter.

3.2 State Space Model

The modal state-space representation is (A_m, B_m, C_m) triple characterized by the block-diagonal state matrix, the modal input and output matrices, which are $A_m = diag(A_{mi})$, $B_m = [B_{m1}, \cdots, B_{mi}, \cdots, B_{mn_m}]^T$, $C_m = [C_{m1}, \cdots, C_{mi}, \cdots, C_{mn_m}]$, $i = 1, \cdots, n_m$, where A_{mi}, B_{mi}, and C_{mi} are 2×2 blocks, $2 \times ac$ blocks (ac is the number of inputs), and $sr \times 2$ blocks (sr is the number of outputs), respectively. The state $x = \{x_1, \cdots, x_i, \cdots, x_{n_m}\}^T$, consists of n_m independent components, $x_i = \{x_{i1}, x_{i2}\}^T$, that represent two states of each mode. The ith component, or mode, has the state-space representation (A_{mi}, B_{mi}, C_{mi}) independently obtained from the state equations

$$\begin{aligned} \dot{x}_i &= A_{mi} x_i + B_{mi} u \\ y_i &= C_{mi} x_i \end{aligned} \tag{3.1}$$

The state vector x_i can have different modal coordinates representations. In this thesis, two modal models are used.

For the first modal model,

$$x_i = \begin{Bmatrix} q_i \\ \dot{q}_i \end{Bmatrix} \tag{3.2}$$

the blocks A_{mi}, B_{mi}, and C_{mi} of the model are as follows:

$$A_{mi} = \begin{bmatrix} 0 & 1 \\ -\omega_i^2 & -2\zeta_i\omega_i \end{bmatrix}, B_{mi} = \begin{bmatrix} 0 \\ b_{mi} \end{bmatrix}, C_{mi} = [\ c_{mqi} \quad c_{mvi}\ ]; \tag{3.3}$$

For the second modal model,

$$x_i = \begin{Bmatrix} \omega_i q_i \\ \zeta_i\omega_i q_i + \dot{q}_i \end{Bmatrix} \tag{3.4}$$

By considering small damping ratios ζ_i (${\zeta_i}^2 \approx 0$), the blocks A_{mi}, B_{mi}, and C_{mi} of the model are as follows:

$$A_{mi} = \begin{bmatrix} \zeta_i\omega_i & \omega_i \\ \omega_i & \zeta_i\omega_i \end{bmatrix}, B_{mi} = \begin{bmatrix} 0 \\ b_{mi} \end{bmatrix}, C_{mi} = [\ \tfrac{c_{mqi}}{\omega_i} \quad c_{mvi}(1+\zeta_i)\ ]; \tag{3.5}$$

where, q_i and $\dot{q}_i$ are the ith modal displacement and velocity, which, by coordinates transformation equations (2.66), gives the original nodal displacement U and velocity $\dot{U}$. The first modal model is a straightforward approach and it has direct physical interpretation. However, its properties are not so useful as the second modal model, which shows a symmetrical A_{mi} matrix with small damping ratio simplification.

By introducing the state vector x_i of the first modal model, the second-order governing system equations (2.75) and sensor output equations (2.76) can be converted to a standard first-order state-space form

$$\begin{aligned} \{\dot{x}\} &= A\{x\} + B\{u\} + B_d\{u_d\} \\ \{y\} &= C\{x\} \end{aligned} \tag{3.6}$$

which represents

$$\left\{ \begin{array}{c} \dot{q}_1 \\ \ddot{q}_1 \\ \dot{q}_2 \\ \ddot{q}_2 \\ \cdots \\ \cdots \end{array} \right\} = \left\{ \begin{array}{cccccc} 0 & 1 & 0 & 0 & \cdots & \cdots \\ -\omega_1^2 & -2\zeta_1\omega_1 & 0 & 0 & \cdots & \cdots \\ 0 & 0 & 0 & 1 & \cdots & \cdots \\ 0 & 0 & -\omega_2^2 & -2\zeta_2\omega_2 & \cdots & \cdots \\ \cdots & \cdots & \cdots & \cdots & \cdots & \cdots \\ \cdots & \cdots & \cdots & \cdots & \cdots & \cdots \end{array} \right\} \left\{ \begin{array}{c} q_1 \\ \dot{q}_1 \\ q_2 \\ \dot{q}_2 \\ \cdots \\ \cdots \end{array} \right\}$$

$$-[\bar{M}]^{-1}[\bar{K}^a]\{\Phi_a\} + [\bar{M}]^{-1}\{\bar{F}_M\}$$

where the actuator input $\{u\} = \{\Phi_a\}$, the sensor output $\{y\}$ is the measured reaction electric charge $\{Q_s\}$ appearing on the sensors. The sensor output matrix in the first modal model form is $C_i = [C_{qi}\ C_{vi}]$ and $C_{vi} = 0$, $C_{qi} = -[K^s_{QQ}]^{-1}[K^s_{QU}][\Psi_i]$ is the function of both modal $[\Psi_i]$ and sensor locations. Notice that all the m subscripts in the modal model representations are dropped here. The actuator voltage and mechanical disturbance force terms form the actuator input matrix B and disturbance input matrix B_d.

3.3 Stability Analysis of Closed-loop Feedback System

The stability of dynamic characteristics of structural systems has to be guaranteed for any designed control system. The system natural response should decay to a zero value or oscillate as time approaches infinity. In other words, a control law must be established on the stability theory.

Considering a closed-loop feedback system as (3.6) but without the external force disturbance term $B_d\{u_d\}$

$$\begin{aligned} \{\dot{x}\} &= A\{x\} + B\{u\} \\ \{y\} &= C\{x\} \end{aligned} \tag{3.7}$$

Stability analysis can be done by the following definition: A continuous Linear-Time-Invariant (LTI) system is asymptotically stable when all eigenvalues of the system matrix A have negative real parts.

The eigenvalues of the system are the solutions of the characteristic equation

$$|sI - A| = s^n + a_1 s^{n-1} + \cdots + a_{n-1}s + a_n = 0 \tag{3.8}$$

Given that the solutions are $s_i = \lambda_i$, $i = 1, \cdots, n$, then the system is stable if $Re[\lambda_i(A)] < 0, i = 1, \cdots, n$. For the system (3.7) derived in the previous section, the external input has to be taken into account. It can be defined as the Bounded Input Bounded Output (BIBO) stability of the system as below:

For any bounded input $u(t)$, a system is BIBO stable if the output $y(t)$ and the state $x(t)$ are also bounded, i.e., $\|u(t)\| \leq c1, \forall t \geq 0 \Longrightarrow \|y(t)\| \leq c2, \|x(t)\| \leq c3, \forall t \geq 0$.

Moreover, if $u(t)$ converges to zero as $t \longrightarrow \infty$, then $x(t)$ and $y(t)$ also converge to zero as $t \longrightarrow \infty$.

An alternative approach is based on the Lyapunov stability theory. Consider an LTI system:

$$\{\dot{x}\} = A\{x\} \tag{3.9}$$

Choosing a possible Lyapunov function as

$$V = \{x\}^T P\{x\} \tag{3.10}$$

where P is a positive definite real symmetric matrix. The time derivative of the V gives

$$\dot{V} = \{\dot{x}\}^T P\{x\} + \{x\}^T P\{\dot{x}\} \tag{3.11}$$

Plugging equation (3.9) and after some algebraic manipulations, equation (3.11) becomes

$$\dot{V} = \{x\}^T (A^T P + PA)\{x\} \tag{3.12}$$

By Lyapunov second method of stability theory, asymptotic stability needs a positive definite matrix Q defined as

$$Q = -(A^T P + PA) \tag{3.13}$$

so that $\dot{V} = -\{x\}^T Q\{x\} < 0$.

Therefore, the asymptotic stability can be defined as: The LTI system (3.9) is stable if and only if there exists a positive definite P matrix which satisfies equation (3.13) for a given positive definite matrix Q.

The question of stability of the closed-loop system with a controller should be answered before an implementation of the controller. In order to answer this question, consider the general architecture of a closed-loop feedback control system as shown in Figure 3–1.

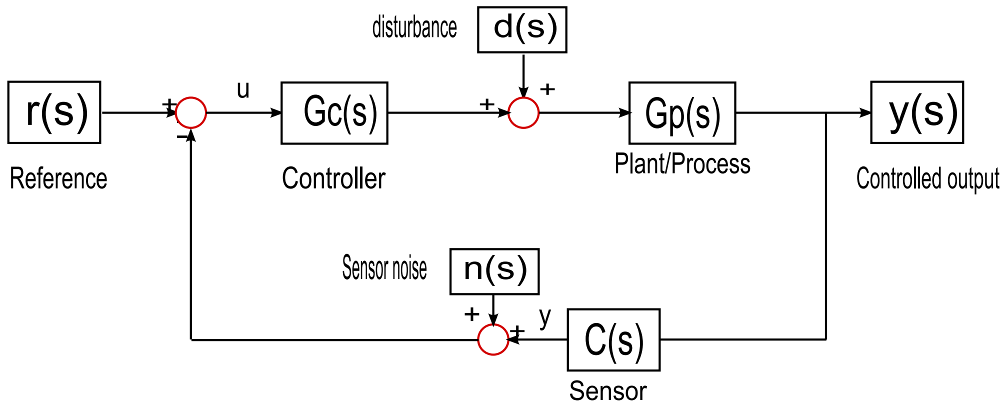

Figure 3–1: Feedback Control Block Diagram

Where, $r(s)$, $d(s)$, $n(s)$, $y(s)$ are reference input, disturbance, sensor noise and sensor output respectivly, Gc, Gp are the controller and plant gains. By simple algebraic manipulations, the relation between reference input and sensor output can be derived as

$$y(s)/r(s) = \frac{GcGp}{1 + GcGp} \tag{3.14}$$

Thus feedback affects the gain Gp of a non-feedback system by a factor $1 + GcGp$ and produces a new closed-loop characteristic equation $1 + GcGp = 0$. Its solution determines the stability of the system which depends on both Gc, Gp gains. The goal is to design the controller block (with gain Gc) to achieve the desired system behavior and ensure the closed-loop system stable at the same time.

3.4 LQR Controller Design

Before designing the controller, whether the structural control system is controllable or not must firstly be considered. Basically, the controllability is the ability that a control input is able to control or alter all the state variables of a system. The actuator numbers and locations, or actuators placement is therefore determined by the controllability.

For our considered piezoelectric smart structures, after applying the modal transformation, the obtained decoupled set of modal coordinate equations must be controlled independently according to the controllability condition. This means that there should be the same number of actuators as that of modal coordinates to ensure the independent modal control.

3.4.1 Controllability

The system (3.7) is said to be controllable when given any initial state $x_0 \in R^n$ at time t_0, any final state $x_f \in R^n$ at finite time t_f, there exists an control input u(t) that takes the state of (3.7) from x_0 to x_f in time $0 \leq t_0 \leq t_f$.

Mathematically, this means Controllability Grammian of the system should be positive definite to guarantee the existence of $u(t)$ [35].

$$G_c = \int_{t_0}^{t_f} e^{A(t_f-\tau)} BB^T e^{A^T(t_f-\tau)} d\tau \tag{3.15}$$

It has been proved that G_c satisfies the Lyapunov equation:

$$AG_c + G_c A^T + BB^T = 0 \tag{3.16}$$

As it is not easy to solve the Lyapunov equation for G_c, an alternative approach is that one can compute the controllability matrix, which is defined by

$$[B \quad AB \quad A^2B \quad \cdots \quad A^{n-1}B] \tag{3.17}$$

The system is controllable if and only if this matrix has the same rank n as the size of the state vector.

3.4.2 Feedback Control Law

Figure (3–2) shows the feedback configuration without reference input and disturbance-free.

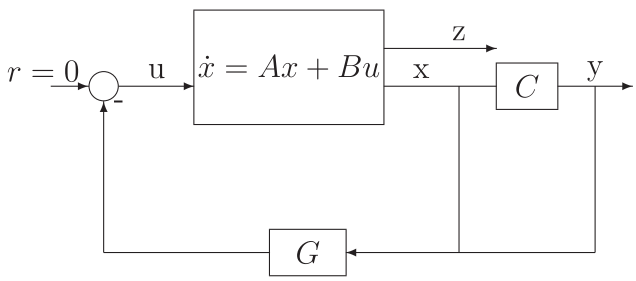

Figure 3–2: Feedback control configuration

The key idea of a feedback control is to use the measured current state of a system to construct an actuator control input. There are two different feedback control laws applied to the control design.

In the case of the full state feedback law where it is assumed that all states are measured and available for feedback. The full state feedback uses all state variables $\{x\}$ to stabilize a system. The control input $\{u\}$ is:

$$\{u\} = -G\{x\} \tag{3.18}$$

By the previous stability analysis, the closed-loop system is stable if $Re[\lambda_i(A-BG)] < 0, \quad i = 1, \cdots, n$. Therefore, the full state feedback control law design is to find the feedback gain G which makes the closed-loop system stable. One of the powerful tool for the full state feedback design is the LQR technique.

The output feedback uses the sensor output $\{y\}$ as the control input $\{u\}$

$$\{u\} = -G\{y\}, \qquad \{y\} = C\{x\} \tag{3.19}$$

The closed-loop system is stable if $Re[\lambda_i(A - BGC)] < 0, \quad i = 1, \cdots, n$. Since usually the number of sensors or output is limited, it is not easy to find a feedback control gain G to satisfy the stability condition in the output feedback control design. There is no unified tool for an output feedback control design compared with the LQR in full state feedback.

3.4.3 State Feedback LQR

LQR is an optimal control procedure which energy-like criteria are used and the minimization procedure automatically produces controllers that are stable and somewhat robust. The key idea is to design an optimal control to minimize a cost function or a performance index which is a quadratic function of the desired system response and required control force [36]:

$$J = \int_0^\infty \Big(\alpha \, \{z(t)\}^T \, \bar{Q}\{z(t)\} + \{u(t)\}^T R\{u(t)\}\Big) \, dt \tag{3.20}$$

where, α is a positive constant, $\bar{Q}$ and R are symmetric positive semi-definite and positive definite weighting matrices on the controlled outputs $\{z(t)\}$ and control inputs $\{u(t)\}$ respectively. A relatively larger $\bar{Q}$ means more controlled output response ability and a larger R puts more limit on applied input control force.

The feedback gain G is found from the solution of the corresponding Controller Algebraic Riccati equation (CARE) [36]:

$$A^T P + PA - PBR^{-1}B^T P + C^T \bar{Q} C = 0 \tag{3.21}$$

where A and B are defined in equation (3.7), P is an auxiliary matrix which is the solution of the CARE (3.21).

The control gain G is then given by:

$$G = R^{-1}B^T P \tag{3.22}$$

Thus the control input $\{u\}$ can be obtained from eqution (3.18) or (3.19).

The relative values of the weighing matrices $\bar{Q}$ and R are selected to trade off requirements on the smallness of the controlled results against requirements on the smallness of the control force. Weighting matrix R can be set as $\beta\boldsymbol{I}$ with β as a positive scalar design parameter. Consequently, α and β can be tuned to establish a trade-off between these conflicting goals for the best control performance.

An efficient way of choosing $\bar{Q}$ is to consider the objective of controlled performance. If the measured sensor output $\{y\} = C\{x\}$ is served as performance output, i.e., $\{z\} = \{y\}$, the related state weight matrix Q can then be computed from output matrix C as $Q = C^T \bar{Q} C$. But usually the trial and error procedure is taken to select the Q.

A crucial property of LQR controller design is that this closed-loop control system is asymptotically stable (i.e., all the eigenvalues of $A - BG$ have negative real part) as long as the system (3.1) is controllable and observable when we choose other than measured sensor output as the sole controlled output $z\{t\}$. Another important property is that LQR controllers are inherently robust with respect to process uncertainty. Moreover, it can also be used for multiple input and output systems design.

3.5 Dynamic Observer Design

The drawback of the full state LQR control design is that the whole states x of the process are required to be measurable. But in most of the control design, the number of sensors is less than state variables due to the actual constraints. A possible approach to overcome this difficulty is to estimate the state of the process based solely on the measured output y of limited number of sensors. Here the concern is to estimate values of the states when they cannot all be measured directly, but only certain measurements are available. The Observability is a primary requirement for the state estimating.

3.5.1 Observability

The system (3.7) is said to be observable when one can determine any initial state $x(t_i)$ by using a finite output $y(t)$ on a certain interval of time $t_i \leq t \leq t_f$.

Mathematically, this means Observability Grammian of the system should be positive definite [37].

$$G_o = \int_{t_i}^{t_f} e^{A^T(t_i-\tau)} C^T C e^{A(t_i-\tau)} d\tau \tag{3.23}$$

where, G_o also satisfies the Lyapunov equation:

$$A^T G_o + G_o A + C^T C = 0 \tag{3.24}$$

Also, similar to the controllability matrix, an alternative approach is that one can compute the observability matrix,

$$\begin{bmatrix} C \\ CA \\ CA^2 \\ \vdots \\ CA^{n-1} \end{bmatrix} \tag{3.25}$$

The system is observable if and only if this matrix has the same rank n as the size of the state vector.

3.5.2 Full Order Observers

An observer is needed to provide the feedback control law with estimated state variables. The mathematical model of the dynamic observer is to construct the physical system based on the sensor measurement.

We assume that x cannot be measured and our goal is to estimate its value based on y. Suppose we construct the estimate $\hat{x}$ by adding a correct term to the replicated process dynamics as

$$\begin{aligned} \left\{\dot{\hat{x}}\right\} &= A\{\hat{x}\} + B\{u\} + L(\{y\} - \{\hat{y}\}) \\ \{\hat{y}\} &= C\{\hat{x}\} \end{aligned} \tag{3.26}$$

where L is a given matrix, $\{\hat{x}\}$, $\{\hat{y}\}$ is an estimate of x, y.

To see if this would generate a good estimate for x, we can define the state estimation error $\{e\} = \{x\} - \{\hat{x}\}$ and study its dynamics.

From (3.7) and (3.26), we conclude that $\{\dot{e}\} = (A - LC)\{e\}$. This shows that when the matrix $A - LC$ is asymptotically stable, the error e converges to zero for any input u, which means that $\{\hat{x}\}$ eventually converges to $\{x\}$ as $t \longrightarrow \infty$.

It turns out that, even when A is unstable, in general we will be able to select L so that $A - LC$ is asymptotically stable. The system (3.26) can be rewritten as

$$\left\{\dot{\hat{x}}\right\} = (A - LC)\{\hat{x}\} + B\{u\} + L\{y\} \tag{3.27}$$

and is called the full order observer, L is the observer gain to be determined [38].

The main strategy of a dynamic observer design is to select the L to ensure the closed-loop system $A - LC$ stable. Full order observer has two inputs: u (control input) and y (process measured output) and one output: $\{\hat{x}\}$ (state estimate). Figure 3–3 shows how a full order observer is connected to the process.

3.6 LQR Compensator Design

The LQR controller and state observer can be combined into a complete system which uses the estimated state variables from the observer in the feedback control law:

$$\{u\} = -G\{\hat{x}\} \tag{3.28}$$

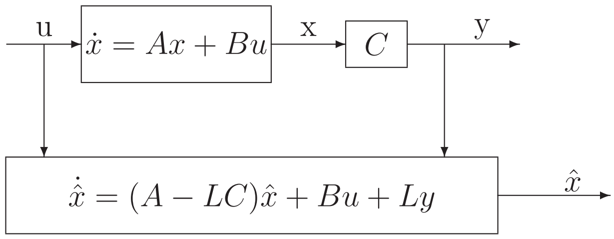

Figure 3–3: Full-order observer

Substituting the equation (3.28) to the equations (3.7) and (3.27), the combined system is:

$$\begin{aligned} \{\dot{x}\} &= A\{x\} - BG\{\hat{x}\} \\ \left\{\dot{\hat{x}}\right\} &= (A - BG - LC)\{\hat{x}\} + L\{y\} \end{aligned} \tag{3.29}$$

Substituting the output equation $\{y\} = C\{x\}$ and rearranging the above equations yield:

$$\left\{ \begin{array}{c} \dot{x} \\ \hat{x} \end{array} \right\} = \left[\begin{array}{cc} A & -BG \\ LC & A - BG - LC \end{array} \right] \left\{ \begin{array}{c} x \\ \hat{x} \end{array} \right\} \tag{3.30}$$

The combined control system can be called LQR compensator. Separation principle are used to check whether or not this combined closed-loop system is stable. Using the property in linear algebra, the characteristic equation of the combined system can be simplified as:

$$|\lambda I - A + BG|\,|\lambda I - A + LC| = 0 \tag{3.31}$$

This characteristic equation consists of two separate parts: the feedback control law and the dynamic observer. The system stability and control design can therefore be achieved by the separation principle: The eigenvalues of the closed-loop system (3.7) are given by both the state-feedback regulator dynamics $A - BG$ and state-estimator dynamics $A - LC$. In case these both matrices are asymptotically stable, then so is the closed loop. This means that the feedback gain G and the observer gain L can be designed separately.

3.7 LQG Compensator Design

3.7.1 Definition

Previously considered LQR controllers and state estimators were designed under the assumed disturbance-free environment. However, in general the sensor output is affected by measurement noise and the process dynamics are also affected by disturbances. For vibration suppression purposes, it is expected that the suppression requirements should be satisfied with natural frequencies both within the controller bandwidth and within the disturbance spectra.

LQG (Linear system, Quadratic cost, Gaussian noise) controllers can typically meet these conditions and they can be designed for both vibration suppression and disturbance rejection purposes.

The closed-loop system configuration of the LQG controll system is shown in Figure 3–4. In this figure (A, B, C) is the plant state-space triple, x is the state, $\hat{x}$ is the estimated state, u is the control input, y is the output, $\hat{y}$ is the estimated output. It consists of a stable plant or structure and a controller (G). The plant output y is measured and supplied to the controller. Using the output y the

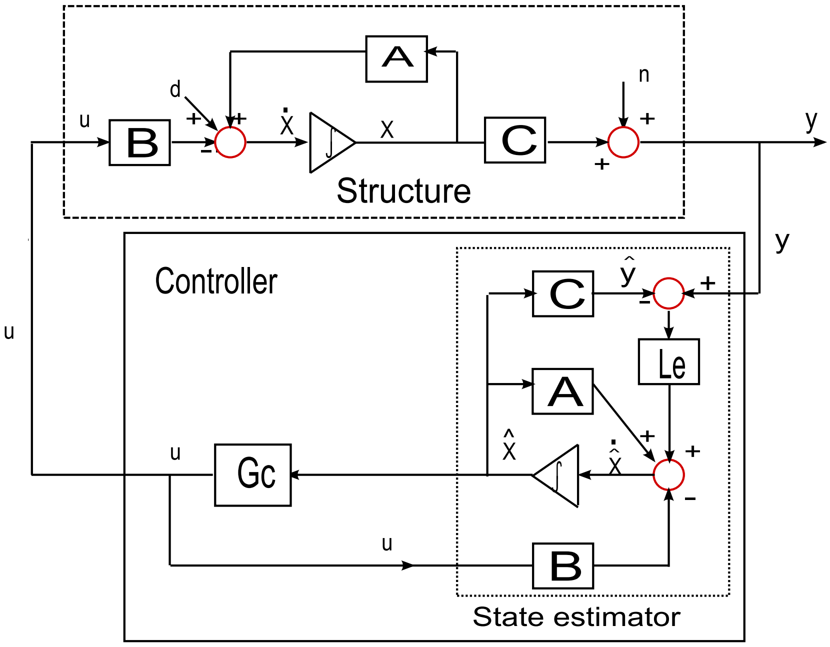

Figure 3–4: LQG closed-loop system block diagram

controller determines the control signal u that drives the plant. Notice that the curly brackets for the vectors are also dropped off for simplicity in this section.

The plant is described by the following state-space equations:

$$\begin{aligned} \dot{x} &= Ax + Bu + B_d d \\ y &= Cx + n \end{aligned} \tag{3.32}$$

where the plant or the structure is perturbed by initial disturbance force, denoted by d, and its output is corrupted by measurement noise n.

3.7.2 LQG Estimator

Rewrite the estimation error for (3.32) and (3.26), which leads to $\dot{e} = Ax + B_d d - A\hat{x} - L(Cx + n - C\hat{x}) = (A - LC)e + B_d d - Ln$

Because of n and d, the estimation error will generally not converge to zero, but will remain small by appropriate choice of the observer gain matrix L. This motivates the so called LQG estimation problem: Find the observer gain L that minimizes the asymptotic expected value of the estimation error e.

$$J_{LQG} = \lim_{t \to \infty} E[\|e(t)\|^2] \tag{3.33}$$

where $d(t)$ and $n(t)$ are zero-mean Gaussian noise processes with power spectrum $S_d(\omega) = Q_N$; $S_n(\omega) = R_N$; $\forall\omega$. $Q_N = E(dd^T)$, $R_N = E(nn^T)$ are the covariances of noises d and n. And they are uncorrelated from each other, i.e., $E(dn^T) = 0$.

The solution to this optimal LQG Problem gives the LQG estimator gain L as

$$L = PC^T R_N^{-1} \tag{3.34}$$

where P is the unique positive-definite solution to the following Filter Algebraic Riccati Equation (FARE)

$$AP + PA^T + B_d Q_N B_d^T - PC^T R_N^{-1} CP = 0 \tag{3.35}$$

and this system is called the Kalman-Bucy filter. Different choices of Q_N and R_N result in different estimator gains L.

A crucial property of the system is that $A - LC$ is asymptotically stable as long as the system (3.32) is observable and controllable when we ignore u and regard d as the sole input.

3.7.3 LQG Compensator

Using the estimator equation(3.27) and referring the inner structure block diagram of the LQG closed-loop system in Figure 3–4, the LQG compensator state space equations from input y to output u can be derived as:

$$\begin{aligned} \dot{\hat{x}} &= (A - BG - LC)\hat{x} + Ly \\ u &= -G\hat{x} \end{aligned} \tag{3.36}$$

From these equations, we obtain the LQG compensator triple (A_lqg, B_lqg, C_lqg)

$$\begin{aligned} A_{lqg} &= A - BG - LC \\ B_{lqg} &= L \\ C_{lqg} &= -G \end{aligned} \tag{3.37}$$

The open-loop system are given by (3.32), and the LQG follow from (3.37), Defining a new state variable

$$x_c = \begin{Bmatrix} x \\ e \end{Bmatrix} \tag{3.38}$$

where $e = x - \hat{x}$, we obtain the closed-loop state-space equations in the form:

$$\begin{aligned} x_c &= A_c x_c + B_c d \\ z &= C_c x_c \end{aligned} \tag{3.39}$$

where

$$A_c = \begin{bmatrix} A & BG \\ 0 & A - LC \end{bmatrix} \quad B_c = \begin{bmatrix} B_d \\ B_d \end{bmatrix} \quad C_c = \begin{bmatrix} C & 0 \end{bmatrix} \tag{3.40}$$

is the closed-loop triple.

3.7.4 The Balanced LQG Compensator

The solutions of the CARE and FARE depend on the states we choose. Among the multiple choices there exists a state-space representation such that the CARE and FARE solutions are equal and diagonal, see [39], [40], and [41], assuming that the system is controllable and observable.

In this case we obtain $P = M = diag(\lambda_i)$, $i = 1, \cdots, N$, $\lambda_1 \geq \lambda_2 \geq \cdots \lambda_N > 0$, where λ_i are its LQG singular (or characteristic) values and M is a diagonal positive definite matrix. A state-space representation with this condition satisfied is called an LQG balanced representation.

Let R be the transformation of the state x such that $x = R\bar{x}$. Then the solutions of CARE and FARE in the new coordinates are $\bar{S}_c = R^T PR$, $\bar{S}_e = R^{-1}PR^{-T}$, and the weighting matrices are $\bar{Q}_c = R^T QR$, $\bar{Q}_e = R^{-1}QR^{-T}$.

The transformation R to the LQG-balanced representation can be obtained as follows: For a given state-space representation (A, B, C), firstly, decompose the solutions of CARE and FARE as $S_c = P_c^T P_c$ and $S_e = P_e P_e^T$. Then, form a matrix H, such that $H = P_c P_e$. Next, find the singular value decomposition of H, $H = VMU^T$. Lastly the transformation matrix can be obtained either as $R = P_e U M^{-1/2}$ or as $R = P_c^{-1} V M^{1/2}$.

CHAPTER 4
Active Vibration and Buckling Control of Piezolaminated Beams

4.1 Summary

The goal is to increase the beam buckling loads by using piezoelectric sensors/actuators along with optimal feedback control. First, both Euler-Bernoulli and Timoshenko beam theory based laminated beam elements are formulated. Then, LQG active control is designed to stabilize the first two buckling modes of both simply supported and cantilevered beams.

The uniform beams are bonded with two pairs of segmented piezoelectric sensors/actuators at top and bottom sides. The sensor's measurements are taken to estimate the system states. The beams are subjected to a slowly increasing axial compressive load. Finite element formulations based on the classical Euler-Bernoulli beam theory, Timoshenko First-order shear deformation theory, and Layer-wise shear deformation theory and linear piezoelectric constitutive equations for the piezoelectric sensor and actuator are presented. The associated reduced order modal equations and state-space equations are derived for the design of an LQG control.

The finite element analysis and the active control simulation results are consistent with both theoretical analysis results and experimental data. The designed full state feedback LQR controller and dynamic observer are shown to be successful in stabilizing the first two buckling modes of the beams. Also the control simulation shows that the optimally located segmented sensor/actuator pairs along the beam are more effective in the buckling control.

The problem addressed in this chapter is the active control of the first two buckling modes of flexible beams. The controlled structures can bear more load and have extensive application in high-performance, light-weight structural systems, especially in aerospace engineering.

Meressi and Paden [19] have shown that the buckling of a simply supported beam can be postponed beyond the first critical load by means of feedback control using piezoelectric actuators and strain gauge sensors. Hence, the controlled beam could support a load up to the second critical load. Berlin [42] constructed a prototype composite column that was stabilized against buckling through the use of piezoelectric actuators and non-adaptive control strategies. He demonstrated that multiple buckling modes can be stabilized simultaneously. The load-bearing strength of his controlled column was increased by 5.6 times. Some other researchers have also discussed multi-mode control problems [43].

First, a finite element vibration and buckling analysis of axial compressed simply-supported or cantilevered beam is performed. Next, the associated modal equations and state-space equations of a reduced order system are derived. A compensator combining the feedback control law and the dynamic observer is then designed to stabilize the first two buckling modes of both simply-supported and cantilevered beams. Lastly, some results and conclusions are given.

4.2 Finite Element Formulation

4.2.1 Classical Laminated Beam Theory

The piezo-laminated beam assumes the substrate, sensor layers, and actuator layers as a continuous structure and there is a linear distribution of strain. The displacement and strain follow the Euler-Bernoulli assumption that the plane cross-section normal to the beam axis remains plane and normal to the axis after deformation. The transverse displacement of each layer is same and the shear strains between the layers are negligible. The displacement field for the k^{th} layer is defined as

$$\begin{aligned} u_1^k =& u - z\frac{\partial w}{\partial x} \\ u_3^k =& w \end{aligned} \tag{4.1}$$

where, $\left\{u_1^k, u_3^k\right\}^T$ is the displacement field vector, u, w are the lateral displacement on x-axis and the transverse displacement on z-axis of the midplane, respectively.

The mechanical strain energy for the k^{th} layer can be written as

$$U_\epsilon^k = \int_0^L \left\{ \frac{E^k A^k}{2} \left[\frac{du}{dx} + \frac{1}{2}\left(\frac{dw}{dx}\right)^2 \right]^2 + \frac{E^k I^k}{2}\left(\frac{d^2 w}{dx^2}\right)^2 \right\} dx \tag{4.2}$$

where, L, E^k, A^k, and I^k are the beam length, Young modulus, the area and moment of inertia of the beam cross section for the k^{th} layer, respectively.

The above can be explicitly written as

$$U_\epsilon^k = \int_0^L \left\{ \frac{E^k A^k}{2} \left[\left(\frac{du}{dx}\right)^2 + \frac{du}{dx}\left(\frac{dw}{dx}\right)^2 + \frac{1}{4}\left(\frac{dw}{dx}\right)^4 \right] + \frac{E^k I^k}{2}\left(\frac{d^2 w}{dx^2}\right)^2 \right\} dx \tag{4.3}$$

For small displacement assumption, only the first term and the last term of equation (4.3) are kept, and so

$$U_{\epsilon}^{k} = \int_{0}^{L} [\frac{E^k A^k}{2} \left(\frac{du}{dx}\right)^2 + \frac{E^k I^k}{2} \left(\frac{d^2 w}{dx^2}\right)^2]dx \tag{4.4}$$

Applying both linear and Hermitian interpolation polynomials as shape functions to approximate the independent displacement field

$$u(x) = [N_5 \ N_6] \begin{Bmatrix} u_i \\ u_j \end{Bmatrix}, \ \ w(x) = [N_1 \ N_3 \ N_2 \ N_4] \begin{Bmatrix} w_i \\ \frac{dw_i}{dx} \\ w_j \\ \frac{dw_j}{dx} \end{Bmatrix} \tag{4.5}$$

where, the subscripts i, j indicate the local node number of the element and the shape functions are

$$\begin{aligned} &N_1 = 1 - \tfrac{3x^2}{l^2} + \tfrac{2x^3}{l^3} \ , N_2 = \tfrac{3x^2}{l^2} - \tfrac{2x^3}{l^3}, \\ &N_3 = -x + \tfrac{2x^2}{l} - \tfrac{x^3}{l^2} \ , N_4 = \tfrac{x^2}{l} - \tfrac{x^3}{l^2}, \\ &N_5 = 1 - \tfrac{x}{l} \ \ , N_6 = \tfrac{x}{l} \end{aligned} \tag{4.6}$$

where, $l = |x_j - x_i|$.

Substituting the discretized displacement equation (4.5) in the strain energy equation (4.4) and integrating over the layer yields the element stiffness matrix of the k^{th} layer as

$$[K^k]^e = \begin{bmatrix} \frac{E^kA^k}{l} & 0 & 0 & -\frac{E^kA^k}{l} & 0 & 0 \\ 0 & \frac{12E^kI^k}{l^3} & \frac{6E^kI^k}{l^2} & 0 & \frac{-12E^kI^k}{l^3} & \frac{6E^kI^k}{l^2} \\ 0 & \frac{6E^kI^k}{l^2} & \frac{4E^kI^k}{l} & 0 & \frac{-6E^kI^k}{l^2} & \frac{2E^kI^k}{l} \\ -\frac{E^kA^k}{l} & 0 & 0 & \frac{E^kA^k}{l} & 0 & 0 \\ 0 & \frac{-12E^kI^k}{l^3} & \frac{-6E^kI^k}{l^2} & 0 & \frac{12E^kI^k}{l^3} & \frac{-6E^kI^k}{l^2} \\ 0 & \frac{6E^kI^k}{l^2} & \frac{2E^kI^k}{l} & 0 & \frac{-6E^kI^k}{l^2} & \frac{4E^kI^k}{l} \end{bmatrix} \tag{4.7}$$

4.2.2 Layer-Wise Shear Deformation Laminated Beam Theory

The piezo-laminated beam assumes each of the substrate, sensor layers, and actuator layers as a Timoshenko beam. That is the plane cross-section normal to the beam axis remains plane but does not remain normal to the axis any longer after deformation. The transverse shear strain is not negligible. The displacement field for the k^{th} layer is defined as

$$\begin{aligned} u_1^k &= u^k - z\phi^k \\ u_3^k &= w \end{aligned} \tag{4.8}$$

To ensure the continuity of displacement, u_1^k must be equal at the interface of base layer and piezo-layers. That is

$$u^b - \frac{h_b}{2}\phi^b = u^s + \frac{h_s}{2}\phi^s \tag{4.9}$$

$$u^b + \frac{h_b}{2}\phi^b = u^a - \frac{h_a}{2}\phi^a \tag{4.10}$$

here, b, s, and a represent the base, sensor, and actuator layer, respectively and h_b, h_s, h_a represent the thickness of the correspondent layers. u^s, u^a can be solved from the above equations as

$$u^s = u^b - \frac{h_b}{2}\phi^b - \frac{h_s}{2}\phi^s \tag{4.11}$$

$$u^a = u^b + \frac{h_b}{2}\phi^b + \frac{h_a}{2}\phi^a \tag{4.12}$$

These are the constraint equations of the beam. The displacements for the base layer and piezo-layers in matrix form become

$$\begin{Bmatrix} u_1^b \\ u_3^b \end{Bmatrix} = \left[C^b\right]\{\Delta\} \tag{4.13}$$

$$[C^b] = \begin{bmatrix} 1 & 0 & -z & 0 & 0 \\ 0 & 0 & 0 & 0 & 1 \end{bmatrix} \tag{4.14}$$

$$\{\Delta\} = \{\ u^b\ \phi^a\ \phi^b\ \phi^s\ w\ \}^T \tag{4.15}$$

$$\begin{Bmatrix} u_1^s \\ u_3^s \end{Bmatrix} = [C^s]\{\Delta\} \tag{4.16}$$

$$[C^s] = \begin{bmatrix} 1 & 0 & -h_b/2 & -(h_s/2+z) & 0 \\ 0 & 0 & 0 & 0 & 1 \end{bmatrix} \tag{4.17}$$

$$\begin{Bmatrix} u_1^a \\ \\ u_3^a \end{Bmatrix} = [C^a]\{\Delta\} \tag{4.18}$$

$$[C^a] = \begin{bmatrix} 1 & h_a/2 - z & h_b/2 & 0 & 0 \\ \\ 0 & 0 & 0 & 0 & 1 \end{bmatrix} \tag{4.19}$$

where, $[C]$ represents the constraint matrix.

Using the strain equation

$$\begin{Bmatrix} \epsilon_{xx}^k \\ \\ 2\epsilon_{xz}^k \end{Bmatrix} = \begin{bmatrix} \frac{\partial}{\partial x} & 0 \\ \\ \frac{\partial}{\partial z} & \frac{\partial}{\partial x} \end{bmatrix} \begin{Bmatrix} u_1^k \\ \\ u_3^k \end{Bmatrix} \tag{4.20}$$

The strains for the base layer and piezo-layers can be written as

$$\begin{Bmatrix} \epsilon_{xx}^b \\ \\ 2\epsilon_{xz}^b \end{Bmatrix} = \left[H^b\right]\{\Delta\} = \left[C^b\right]\left[\partial^b\right]\{\Delta\} \tag{4.21}$$

$$\left[\partial^b\right] = \begin{bmatrix} \frac{\partial}{\partial x} & 0 & 0 & 0 & 0 \\ \\ 0 & 0 & 0 & 0 & 0 \\ \\ 0 & 0 & \frac{\partial}{\partial x} & 0 & 0 \\ \\ 0 & 0 & 0 & 0 & 0 \\ \\ 0 & 0 & -1 & 0 & \frac{\partial}{\partial x} \end{bmatrix} \tag{4.22}$$

$$\begin{Bmatrix} \epsilon_{xx}^s \\ \\ 2\epsilon_{xz}^s \end{Bmatrix} = [H^s]\{\Delta\} = [C^s][\partial^s]\{\Delta\} \tag{4.23}$$

$$[\partial^s] = \begin{bmatrix} \frac{\partial}{\partial x} & 0 & 0 & 0 & 0 \\ 0 & 0 & 0 & 0 & 0 \\ 0 & 0 & \frac{\partial}{\partial x} & 0 & 0 \\ 0 & 0 & 0 & \frac{\partial}{\partial x} & 0 \\ 0 & 0 & 0 & -1 & \frac{\partial}{\partial x} \end{bmatrix} \tag{4.24}$$

$$\left\{ \begin{array}{c} \epsilon^a_{xx} \\ 2\epsilon^a_{xz} \end{array} \right\} = [H^a]\{\Delta\} = [C^a][\partial^a]\{\Delta\} \tag{4.25}$$

$$[\partial^a] = \begin{bmatrix} \frac{\partial}{\partial x} & 0 & 0 & 0 & 0 \\ 0 & \frac{\partial}{\partial x} & 0 & 0 & 0 \\ 0 & 0 & \frac{\partial}{\partial x} & 0 & 0 \\ 0 & 0 & 0 & 0 & 0 \\ 0 & -1 & 0 & 0 & \frac{\partial}{\partial x} \end{bmatrix} \tag{4.26}$$

where, $[\partial]$ represents the operator matrix.

The strain energy for the k^{th} layer is

$$U^k_\epsilon = \frac{1}{2}\int_V \left\{\epsilon^k_{xx} \ 2\epsilon^k_{xz}\right\} \begin{bmatrix} E^k & 0 \\ 0 & G^k \end{bmatrix} \left\{ \begin{array}{c} \epsilon^k_{xx} \\ 2\epsilon^k_{xz} \end{array} \right\} dV \tag{4.27}$$

Substituting strains (4.21), (4.23), and (4.25) to the strain energy equation (4.27) yields

$$U_\epsilon^k = \frac{1}{2}\int_V \left\{ \begin{array}{ccccc} u^b & \phi^a & \phi^b & \phi^s & w \end{array} \right\} [H^k]^T \begin{bmatrix} E^k & 0 \\ 0 & G^k \end{bmatrix} \left[H^k\right] \left\{ \begin{array}{c} u^b \\ \phi^a \\ \phi^b \\ \phi^s \\ w \end{array} \right\} dV \tag{4.28}$$

where, $k = a, b, s$ for actuator, base, and sensor layer respectively.

The independent displacements $u^b, \phi^a, \phi^b, \phi^s, w$ are discretized as

$$\{\Delta\} = \left\{u^b \ \phi^a \ \phi^b \ \phi^s \ w\right\}^T = [N]\{u\} \tag{4.29}$$

where $[N]$ and $\{u\}$ are

$$[N] = \begin{bmatrix} N_5 & 0 & 0 & 0 & 0 & 0 & N_6 & 0 & 0 & 0 & 0 & 0 \\ 0 & N_5 & 0 & 0 & 0 & 0 & 0 & N_6 & 0 & 0 & 0 & 0 \\ 0 & 0 & N_5 & 0 & 0 & 0 & 0 & 0 & N_6 & 0 & 0 & 0 \\ 0 & 0 & 0 & N_5 & 0 & 0 & 0 & 0 & 0 & N_6 & 0 & 0 \\ 0 & 0 & 0 & 0 & N_1 & N_3 & 0 & 0 & 0 & 0 & N_2 & N_4 \end{bmatrix} \tag{4.30}$$

$$\{u\} = \left\{ \begin{array}{cccccccccccc} u_i^b & \phi_i^a & \phi_i^b & \phi_i^s & w_i & w_i^{'} & u_j^b & \phi_j^a & \phi_j^b & \phi_j^s & w_j & w_j^{'} \end{array} \right\}^T \tag{4.31}$$

Here, the shape functions $N_1 \cdots N_4$ are Hermitian polynomials and N_5, N_6 are linear interpolation functions given by (4.6).

Substituting the equation (4.29) to the strain energy equation (4.28) and integrating over the layer yields the element stiffness matrix of the k^{th} layer

$$[K^k]^e = \int_{l_k^e} \left[[N]^T \left(\int_{-h_k/2}^{h_k/2} \int_{-b_k/2}^{b_k/2} [H^k]^T \begin{bmatrix} E^k & 0 \\ 0 & G^k \end{bmatrix} \left[H^k\right] dz\, dy \right) [N] \right] dx \quad (4.32)$$

4.2.3 Electric Potential Energy and Electromechanical Coupled Potential Energy

From the electric potential energy (2.19) and the electromechanical coupled potential energy (2.20) for the piezo layers, the dielectric effect term and the coupling term can be explicitly written as

$$U_{pe}^{pz} = \int_{V_e^{pz}} -\frac{1}{2}(g_{31}^{pz} h_{31}^{pz} + (\beta_{33}^T)^{pz})(D^{pz})^2 dV \quad (4.33)$$

$$U_{pc}^{s} = \int_{V_e^{s}} \frac{1}{2}(h_{31}^{s} \varepsilon_{xx}^{s}) D^s dV \quad (4.34)$$

$$U_{pc}^{a} = \int_{V_e^{a}} -\frac{1}{2}(\varepsilon_{xx}^{a} h_{31}^{a}) D^a dV \quad (4.35)$$

where, superscripts s and a represent the sensor and actuator layer respectively; the superscript pz represents the piezo layer, it can be s or a.

Substituting first the displacement (4.11) and (4.12) in the coupling potential energy (4.34) and (4.35), then applying equation (4.29) to discretize them and integrating over the layer, the coupled element stiffness matrix of the sensor and actuator layers can be explicitly written as

$$[K_{coup}^s]^e = \int_{l^{se}} h_{31}^s S^{se} [H_{coup}^s][N] dx \quad (4.36)$$

where, S^{se} is the element cross section area of the sensor layer, l^{se} is the element length of the sensor layer and

$$\left[H^{s}_{coup}\right] = \left[\begin{array}{ccccc} \frac{1}{2} & 0 & -\frac{h_b}{4} & -\frac{h_s}{4} & 0 \end{array}\right] \begin{bmatrix} \frac{\partial}{\partial x} & 0 & 0 & 0 & 0 \\ 0 & \frac{\partial}{\partial x} & 0 & 0 & 0 \\ 0 & 0 & \frac{\partial}{\partial x} & 0 & 0 \\ 0 & 0 & 0 & \frac{\partial}{\partial x} & 0 \\ 0 & 0 & 0 & 0 & \frac{\partial}{\partial x} \end{bmatrix} \tag{4.37}$$

$$[K^{a}_{coup}]^{e} = \int_{l^{ae}} h^{a}_{31} S^{ae} [H^{a}_{coup}][N] dx \tag{4.38}$$

where, S^{ae} is the element cross section area of the actuator layer, l^{ae} is the element length of the actuator layer and

$$\left[H^{a}_{coup}\right] = \left[\begin{array}{ccccc} -\frac{1}{2} & -\frac{h_a}{4} & -\frac{h_b}{4} & 0 & 0 \end{array}\right] \begin{bmatrix} \frac{\partial}{\partial x} & 0 & 0 & 0 & 0 \\ 0 & \frac{\partial}{\partial x} & 0 & 0 & 0 \\ 0 & 0 & \frac{\partial}{\partial x} & 0 & 0 \\ 0 & 0 & 0 & \frac{\partial}{\partial x} & 0 \\ 0 & 0 & 0 & 0 & \frac{\partial}{\partial x} \end{bmatrix} \tag{4.39}$$

Similarly, integrating equation (4.33) yields the dielectric term

$$[K^{pz}_{dielec}]^{e} = -h^{e}_{pz} (g^{pz}_{31} h^{pz}_{31} + (\beta^{T}_{33})^{pz}) \tag{4.40}$$

4.2.4 Kinetic energy

From the definition of (2.17), the beam kinetic energy of the k^{th} layer is

$$T_k = \int_{V_k} \frac{1}{2}\rho_k \{\dot{u}_1^k \ \dot{u}_3^k\}\{ \begin{matrix} \dot{u}_1^k \\ \dot{u}_3^k \end{matrix} \} dV \tag{4.41}$$

For the classical Euler-Bernoulli beam, substituting the displacement equation (4.1) into the kinetic energy equation (4.41) then discretizing them using equation (4.5) and integrating over the layer will yield element mass matrix of the beam. The consistent mass matrix for the k^{th} layer can then be explicitly written [45] as

$$[M^k]^e = \frac{\rho^k A^k l}{420} \begin{bmatrix} 140 & 0 & 0 & 70 & 0 & 0 \\ 0 & 156 & 22l & 0 & 54 & -13l \\ 0 & 22l & 4l^2 & 0 & 13l & -3l^2 \\ 70 & 0 & 0 & 140 & 0 & 0 \\ 0 & 54 & 13l & 0 & 156 & -22l \\ 0 & -13l & -3l^2 & 0 & -22l & 4l^2 \end{bmatrix} \tag{4.42}$$

For the shear deformable Timoshenko beam,substituting the displacement (4.13), (4.16), and (4.18) into the kinetic energy equation (4.41) then discretizing them using the equation (4.29) and integrating over the layer will yield element mass matrices of the base, the sensor and the actuator layers for $k = b, s, a$

$$[M^k]^e = \rho_k \int_{l_k^e} \left[[N]^T \left(\int_{-h_k/2}^{h_k/2} \int_{-b_k/2}^{b_k/2} [C^k]^T dz\, dy \right) [N] \right] dx \tag{4.43}$$

4.2.5 Governing Equations of Motion

For the vibration analysis and control of the beam, the element dynamic governing equations are (2.28) and (2.29). From the previous equations, all the potential energy terms and kinetic energy terms for each layer are evaluated individually. Consequently the element stiffness and mass matrices are formed by adding all layers together. This formulation can be easily extended from three layers beam to multilayered beam. After assembly of element matrices and vectors, the global governing equation is equation (2.63).

For the buckling analysis and control of the beam, the element dynamic buckling equations are

$$[M]\{\ddot{U}\} + [C_d]\{\dot{U}\} + [K^{\star}]\{U\} - P[K_G]\{U\} = \{F_M\} - [K^a]\{\Phi_a\} \tag{4.44}$$

where, the only new term is the geometric stiffness matrix K_G and P is the axial compressive load.

Considering small lateral displacement of the beam, the slowly increasing axial compressive load P remains essentially constant. The membrane strain energy caused by P is

$$U_m = \int_l (P\epsilon_m)dx \tag{4.45}$$

here, the membrane strain is defined as Green strain in terms of the displacement components u_1 and u_3 in coordinate directions x and z

$$\epsilon_m = u_{1,x} + \frac{1}{2}({u_{1,x}}^2 + {u_{3,x}}^2) \tag{4.46}$$

With small displacement assumption, only first and third terms are kept, this yields

$$U_m = \int_l [P(u_{1,x} + \frac{1}{2}{u_{3,x}}^2)]dx \tag{4.47}$$

For the classical Euler beam, substituting the displacement equation (4.1) into the equation (4.47) then discretizing them using the equation (4.5) and integrating over the layer will yield element geometric stiffness matrix K_G^e of the beam which can be explicitly written [45] as

$$[K_G]^e = \frac{1}{30l}\begin{bmatrix} 30 & 0 & 0 & -30 & 0 & 0 \\ 0 & 36 & 3l & 0 & -36 & 3l \\ 0 & 3l & 4l^2 & 0 & -3l & -l^2 \\ -30 & 0 & 0 & 30 & 0 & 0 \\ 0 & -36 & -3l & 0 & 36 & -3l \\ 0 & 3l & -l^2 & 0 & -3l & 4l^2 \end{bmatrix} \tag{4.48}$$

Comparing the $P[K_G]$ with the elastic stiffness matrix (4.7), for the net stiffness $\pm(EA + P)/l$ associated with the displacement u term, because of $EA >> |P|$ in any parctical problem, the extra P/l terms are negligible.

For the Timoshenko beam, substituting the displacement equation (4.13) into the equation (4.47) and keeping only the terms associated the w, then discretizing them using the equation (4.29) and integrating over the layer yields element geometric stiffness matrix K_G^e as

$$\begin{aligned} &[K_G]^e = \textstyle\int_0^l [N]^T([\partial_G]^T[\partial_G])[N]dx \\ &[\partial_G] = \{\ 0 \quad 0 \quad 0 \quad 0 \quad \tfrac{\partial}{\partial x}\ \} \end{aligned} \tag{4.49}$$

4.3 Model Validation

The present classical Euler and first order shear deformable Timoshenko piezolaminated beam elements are validated by considering free vibrations of both the simply supported (SS) and the cantilever beams (CF). For comparison with the known results, both beams have the same modulus of elasticity $E = 10^8 Pa$, Possion's ratio $\nu = 0.3$, area of cross section $A = b \times h$, length $L = 1.0m$, width $b = 0.10m$, mass density $\rho = 1.0kg/m^3$, shear correction factor $\kappa = 5/6$ and all using 40 elements to compute the first 12 natural frequencies for different thickness $h = 0.001, 0.01, 0.1$. Non-dimensional natural frequencies are given by $\bar{\omega} = \omega L^2 \sqrt{\frac{\rho A}{EI_z}}$. Results are presented in Table 4–1 and Table 4–2. They are in excellent agreement with Euler beam exact solution [46] and more accurate, especially for the higher modes compared with Ferreiras result [47].

Table 4–1: Comparison of non-dimensional natural frequencies $\bar{\omega}$ for SS beam

Modes	Euler exact	Euler element	Timoshenko element		
			h/L=0.001	h/L=0.01	h/L=0.1
1	9.8696	9.8730	9.8772	9.8755	9.7148
2	39.478	39.533	39.600	39.574	37.202
3	88.826	89.103	89.445	89.309	78.620
4	157.91	158.79	159.88	159.44	129.92
5	246.74	248.88	251.56	250.48	187.93
6	355.31	359.74	365.37	363.10	250.48
7	483.61	491.84	502.40	498.12	316.17
8	631.65	645.71	664.01	656.54	384.12
9	799.44	821.99	851.81	839.54	453.82
10	986.96	1021.4	1067.8	1048.5	524.94
11	1194.2	1244.7	1314.1	1285.0	597.33
12	1421.2	1492.9	1593.5	1550.8	670.90

Table 4–2: Comparison of non-dimensional natural frequencies $\bar{\omega}$ for CF beam

Modes	Euler exact	Euler element	Timoshenko element		
			h/L=0.001	h/L=0.01	h/L=0.1
1	3.51602	3.51598	3.51628	3.51600	3.48862
2	22.0345	22.0463	22.0683	22.0561	20.9368
3	61.6972	61.8034	61.9689	61.8871	55.1956
4	120.902	121.340	121.978	121.680	100.441
5	199.860	201.101	202.857	202.059	153.467
6	298.556	301.391	305.344	303.579	211.796
7	416.991	422.612	430.409	426.961	273.824
8	555.165	565.250	579.255	573.090	338.499
9	713.079	729.876	753.342	743.022	405.101
10	890.732	917.148	954.416	937.993	473.075
11	1088.12	1127.81	1184.54	1159.43	541.863
12	1305.26	1362.70	1446.15	1408.97	610.497

Another useful result observed from the above accuracy comparation of dimensionless frequencies is that Euler element should be used for a thin beam ($h/L < 0.001$) and Timoshenko element is for a moderate thickness beam ($h/L \geq 0.001$). The higher order frequencies cannot be well predicted by employing less elements using a lower order theory.

Next, the lowest buckling loads are computed using both present classical Euler and first order shear deformable Timoshenko piezolaminated beam elements for the simply supported and the cantilever beams. Both beams have the same modulus of elasticity $E = 10^7 Pa$, Possion's ratio $\nu = 1/3$, area of cross section $A = b \times h$, length $L = 1.0m$, width $b = 0.10m$, mass density $\rho = 1.0kg/m^3$, shear correction factor $\kappa = 5/6$ and all using 40 elements to compute the first 12 natural frequencies for different thickness cases $h = 0.001$, 0.01, $0.1m$.

The exact solution [48] is

$$P_{cr} = \frac{\pi^2 EI}{L_{eff}^2}\left[\frac{1}{1+\frac{\pi^2 EI}{L_{eff}^2 \kappa GA}}\right]$$

where L_{eff} is the effective beam length. For SS or pinned-pinned beams ($L_{eff} = L$) and for CF or clamped-free beams ($L_{eff} = 2L$).

Table 4–3 shows the buckling loads for SS and CF beams computed using 40 elements of present Euler and Timoshenko elements. They show an excellent agreement with the exact solution and results of Ferreira code [47].

Table 4–3: Comparison of beam critical loads

	Simply support			Cantilever		
h/L	0.001	0.01	0.1	0.001	0.01	0.1
Exact	0.0082	8.2230	8013.8	0.0021	2.0560	2042.7
Present Euler element	0.0082	8.2247	8224.7	0.0021	2.0562	2056.2
Present Timoshenko	0.0082	8.2303	7959.6	0.0021	2.0565	2039.1
Ferreira Timoshenko	0.0082	8.2310	8021.8	0.0021	2.0566	2050.0

4.4 Case Studies

Three case studies are presented to demonstrate the validity and efficiency of the proposed finite element analysis models and both active vibration suppression and buckling control designs.

4.4.1 Active Vibration Control of an Experimental Cantilever Beam

The same experimental beam (Figure 4–1) tested by Yousefi-Koma [49] is studied first.

The dimensions and mechanical-piezoelectric properties are listed in Table 4–4 and Table 4–5. The finite element model is given in Figure 4–2

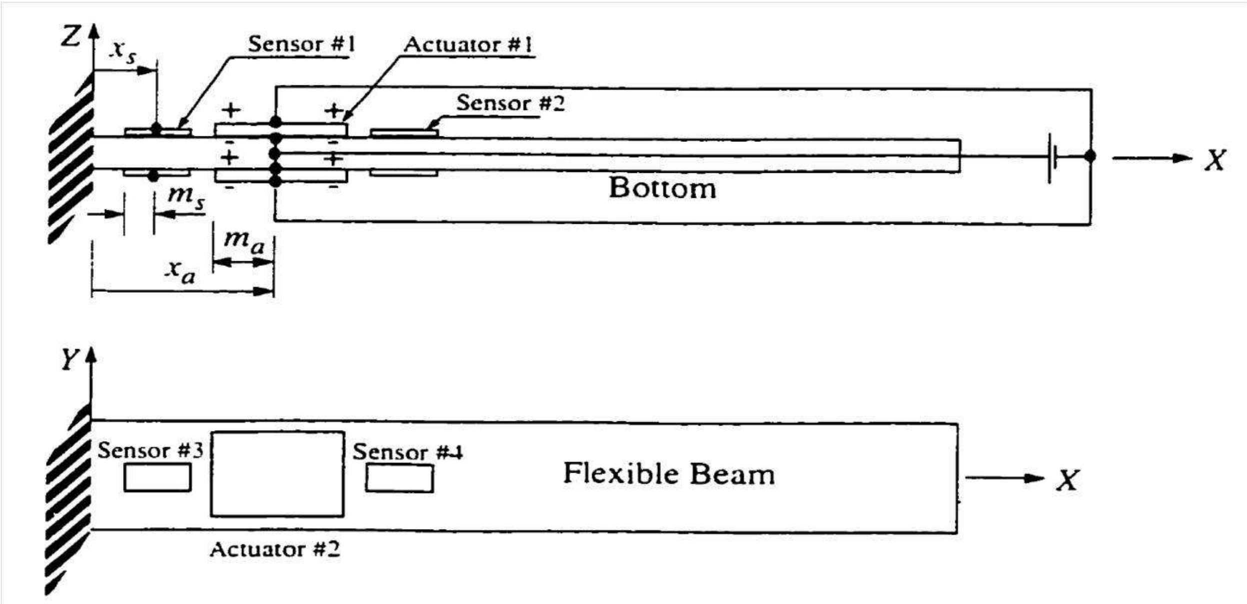

Figure 4–1: Physical model of a cantilever beam with sensors and actuators

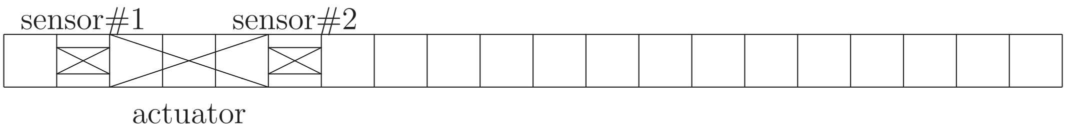

Figure 4–2: 20 elements analysis model of the experimental beam

Table 4–4: Piezoelectric material properties and geometric specifications

	PZT actuators		PVDF sensors			
Side/No.(T:top, B:bottom)	T/1	B/2	T/1	T/2	B/3	B/4
Mid point position $x_a, x_s(mm)$	89.0	89.0	35.4	142.6	35.4	142.6
Half the length $m_a, m_s(mm)$	38.1	38.1	13.5	13.5	13.5	13.5
Width $W_a, W_s(mm)$	25.4	25.4	13.0	13.0	13.0	13.0
Thickness $t_a, t_s(mm)$	0.305	0.305	0.028	0.028	0.028	0.028
Density (Kg/m^3)	7350.0		1780.0			
Elastic modulus (Pa)	71.4×10^9		2.0×10^9			
Electric permittivity $\epsilon_p(F/m)$	150.4×10^{-10}		1.06×10^{-10}			
Piezoelectric strain constant $d_{31}(m/v)$	200.0×10^{-12}		23.0×10^{-12}			
Maximum electric field $(v/\mu m)$	1.0		30.0			

Table 4–5: Aluminium beam properties and geometric specifications

Length $L_b(mm)$	508.0
Width $W_b(mm)$	25.4
Thickness $t_b(mm)$	0.8
Density (Kg/m^3)	2710.0
Elastic modulus(Pa)	72.0×10^9
Poisson's ratio	0.3333

Using the same first two modal damping ratios (ζ) obtained from the experiment which are 0.011 and 0.055, the first two natural frequencies of the experimental beam are presented in Table 4–6 for the beam without any piezo-elements and Table 4–7 with bonded piezo-elements respectively.

Table 4–6: Frequencies of the experimental beam without any piezo-elements

	Natural frequencies(Hz)	
	mode 1	mode 2
Analytical [50]	2.58	16.30
Abaqus [50]	2.59	16.29
ANSYS [50]	2.59	16.27
Present Euler element	2.5812	16.1762
Present Timoshenko element	2.5832	16.3313

Table 4–7: Frequencies of the experimental beam with bonded piezo-elements

		Natural frequencies (HZ)			
Mode	ζ_i	Experiment [49]	Abaqus [50]	ANSYS [51]	Proposed FSDT
1	0.011	3.41	3.30	3.11	3.2972
2	0.055	16.90	16.21	16.07	16.1782

In the case of beam bonded with piezo-elements, the shear stress and shear deformation between the beam and piezo-elements have to be considered on account of the coupled piezoelectric-mechanical field. Timoshenko element should be used to obtain better results. It is seen that the proposed First order Shear Deformable Theory (FSDT) piezo-laminated beam element analysis results (all with 20 elements) are quite closer to the experimental data compared with the other two commercial finite element analysis programs results [50].

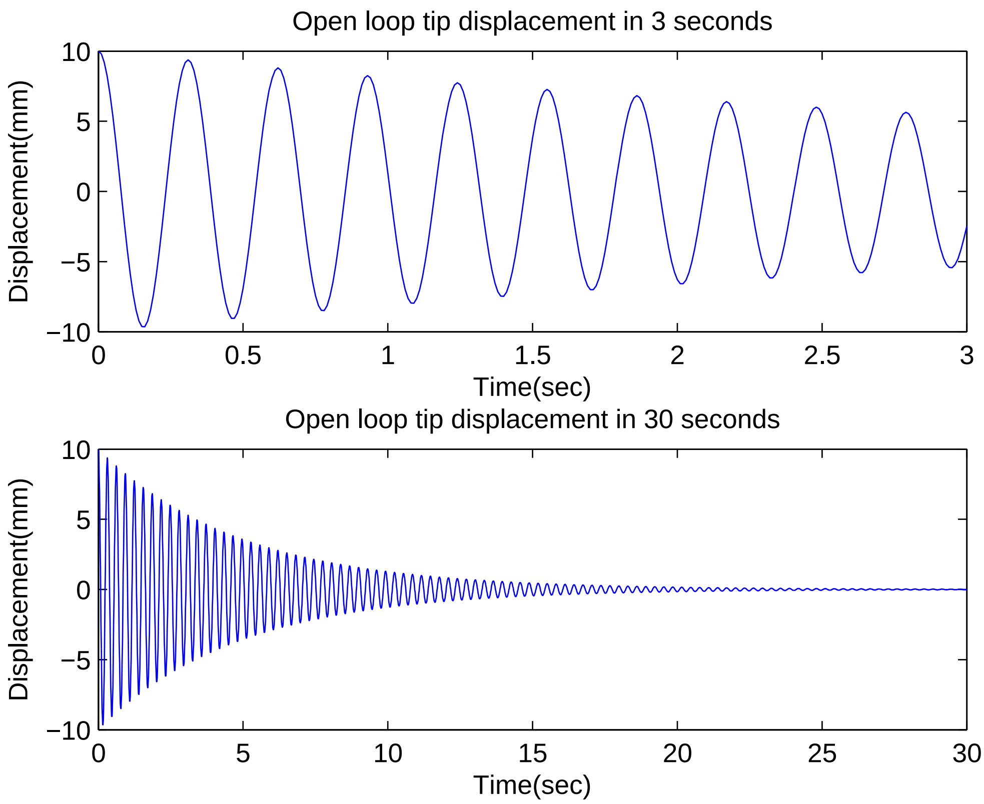

Figure 4–3: Open loop responses of tip displacement in 3 and 30 seconds

As in the experimental study, the beam is under an initial tip displacement of 10mm and only the first two modes are included in the numerial simulation.

Figure 4–3 shows the no control open loop tip displacement of the free vibration beam for 3 and 30 seconds respectively. Figure 4–4 gives the output voltage of the sensor #1 in a 3 seconds period for the beam. It shows good agreement with the experiment results [49].

For the LQR control, we have four equal states and sensors as only the first two modes are considered. A full state feedback LQR controller can be designed.

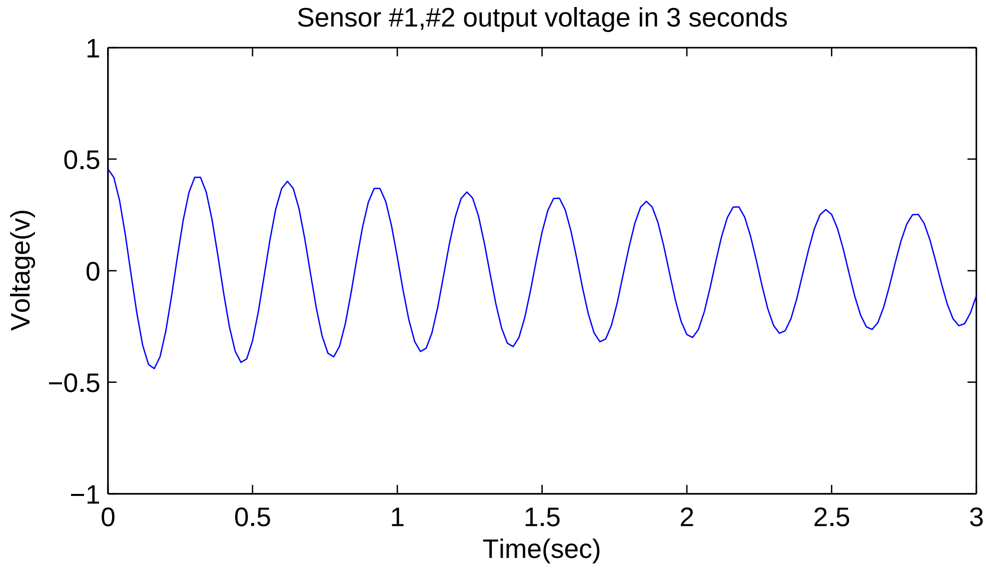

Figure 4–4: Open loop output voltage of sensor #1, #2 in 3 seconds

The state weight matrix Q and control input weight matrix R are chosen based on the balance of desired control performance and control input limit. As the tip vertical displacement is set as performance output, Q can be computed from output matrix C with $Q = C^TC$. $\bar{Q} = I_{4\times4}$ is chosen as a diagonal matrix with equal elements for considering all of the sensor signals to be of equal importance. $R = \beta I$ with $\beta = 1.3$ and $\alpha = 10^8$ are chosen such that the settling time of one second of the tip displacement as the control performance while the control voltage remains below the breakdown voltage ($V_{max} = h_a * 1.0v/\mu m = 305v$) of the piezoelectric PZT-actuator (i.e. $-305v < V_{control} < 305v$).

The Matlab control toolbox was used in simulation to obtain the control state feedback gains G. Using full state feedback control law equation (3.18), control voltage of the actuators can be obtained. The closed loop response of the beam tip displacement in Figure 4–5 has a 1 second settling time which is 20 times faster than the 20 seconds open loop case. Figure 4–7 plots the output voltage of the sensor #1 and #2 (they are very close from the simulation results). Figure 4–8 plots the output current of the sensor #3 and #4. Figure 4–6 shows the corresponding control voltage of the actuators, which has an absolute value less than $V_{max} = 305v$. Fairly good agreements on beam tip displacement response, sensor outputs, and applied control input force are observed between the experiment and simulation results.

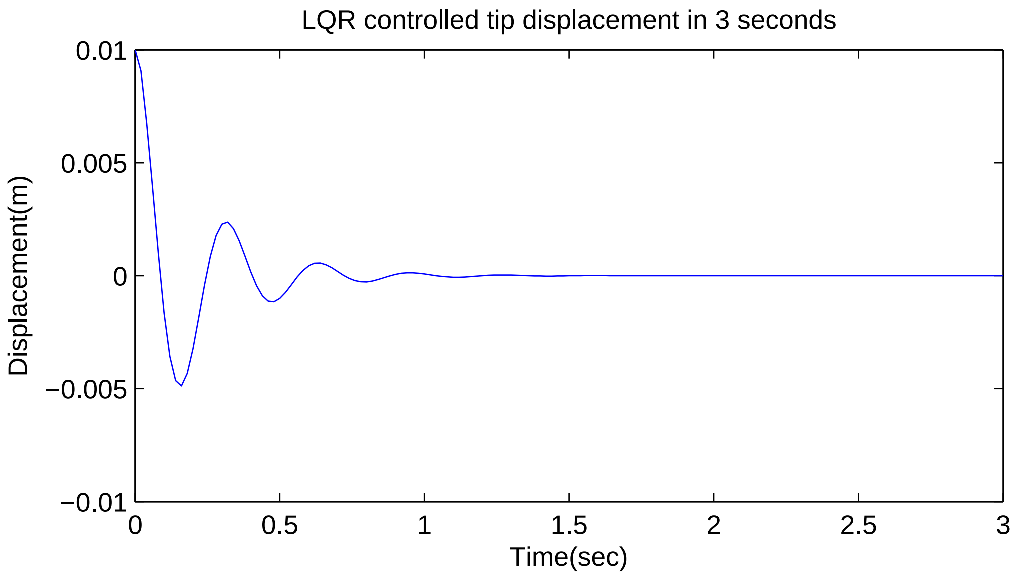

Figure 4–5: LQR controlled tip displacement in 3 seconds

The piezoelectric materials are very sensitive to the environment noise and process or plant disturbances. The output measurements of the sensors may absorb all kind of acoustic, thermal, mechanical, and electrical disturbances. The previous LQR controller was designed for the noise-free environment and cannot

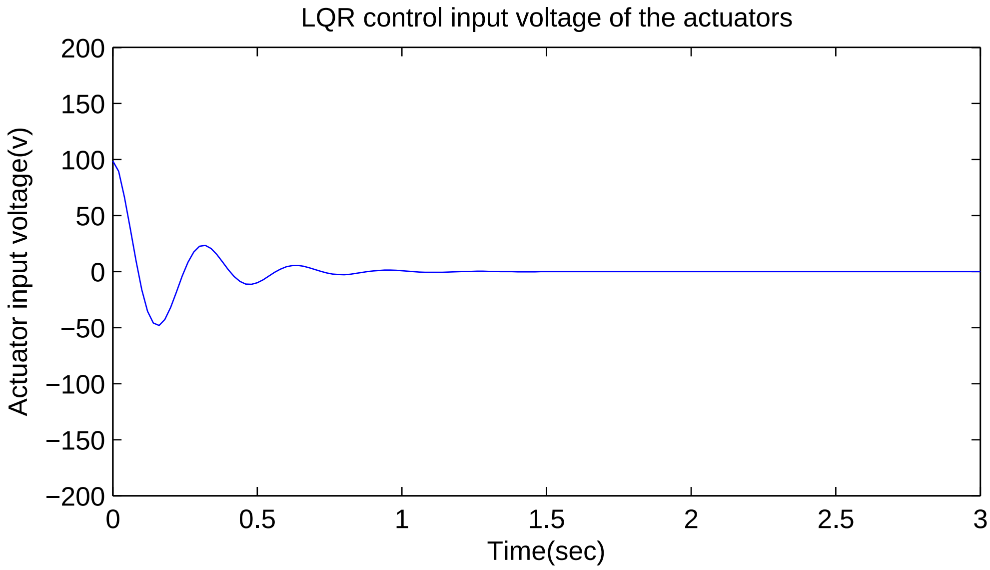

Figure 4–6: LQR control input voltage of the actuators

compensate for the noises. LQG compensator was then designed to serve both the vibration control and disturbance rejection purposes.

Figure 4–9 and 4–10 show the LQG controlled tip displacement and control input voltage respectively. As we see the closed loop response is very smooth and the LQG has compensated the noise completely. The controlled results and the required control voltage are almost identical to that of the LQR control system without any noise, as is evident from comparison with the figures 4–5 and 4–6. Figure 4–11 shows the LQR control system cannot dampen both the noise and vibration. Also from Figure 4–12, the required control voltage ($|V_{control}| > 500v$) for the LQR system is high enough to destroy the piezoelectric PZT actuator ($V_{max} = 305v$), whereas the required control voltage of the LQG system is in the acceptable range.

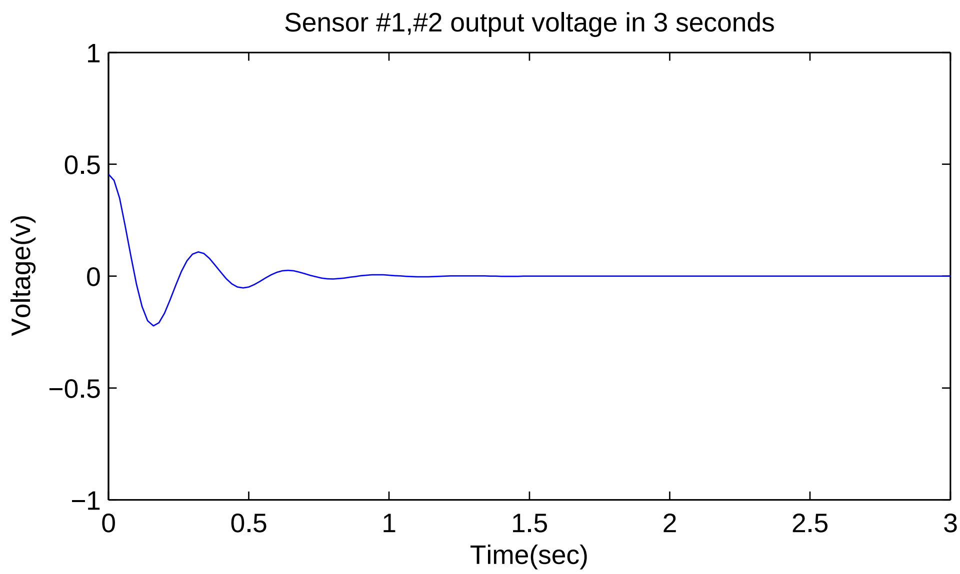

Figure 4–7: Sensor #1, #2 output voltage in 3 seconds

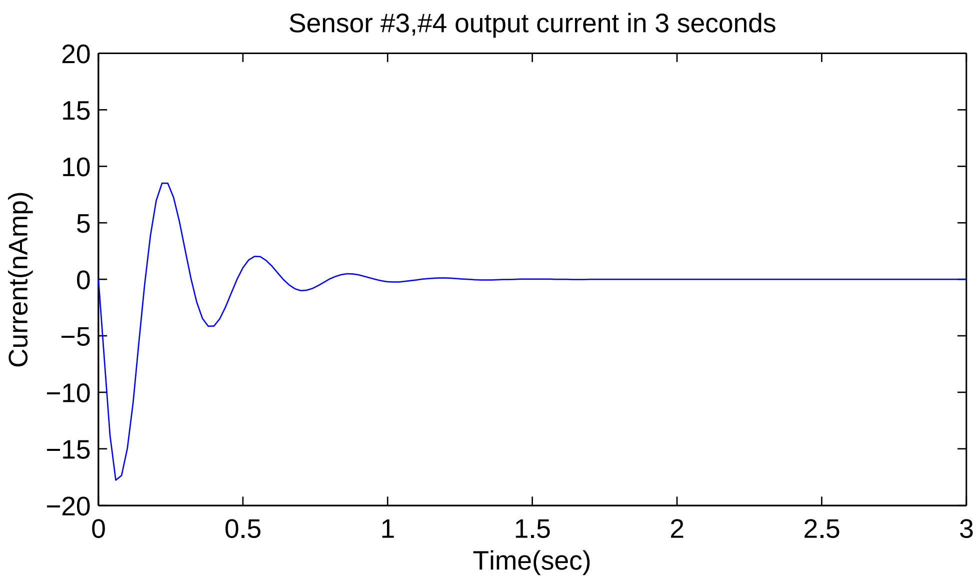

Figure 4–8: Sensor #3, #4 output current in 3 seconds

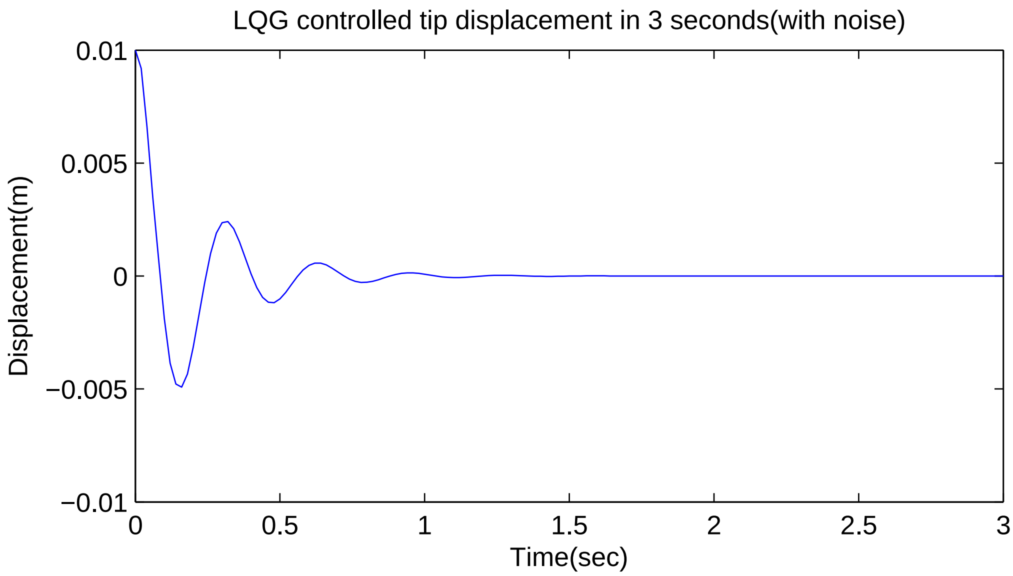

Figure 4–9: LQG controlled tip displacement with noise

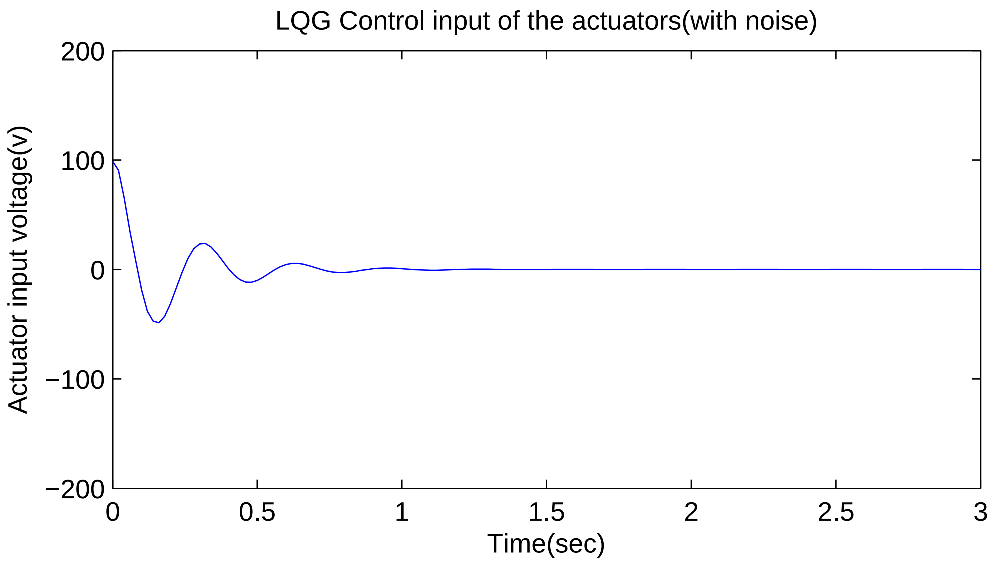

Figure 4–10: LQG control input voltage with noise

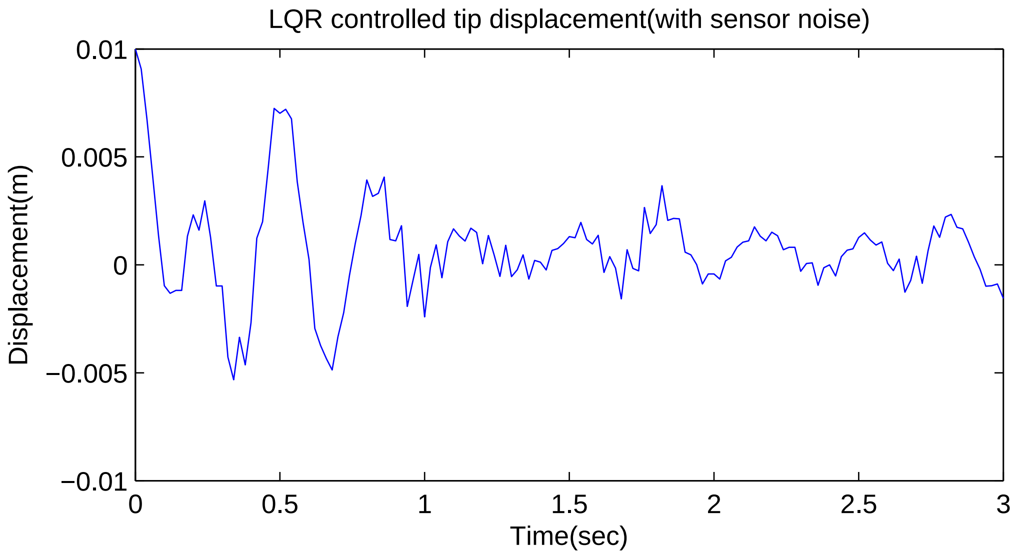

Figure 4–11: LQR controlled tip displacement with noise

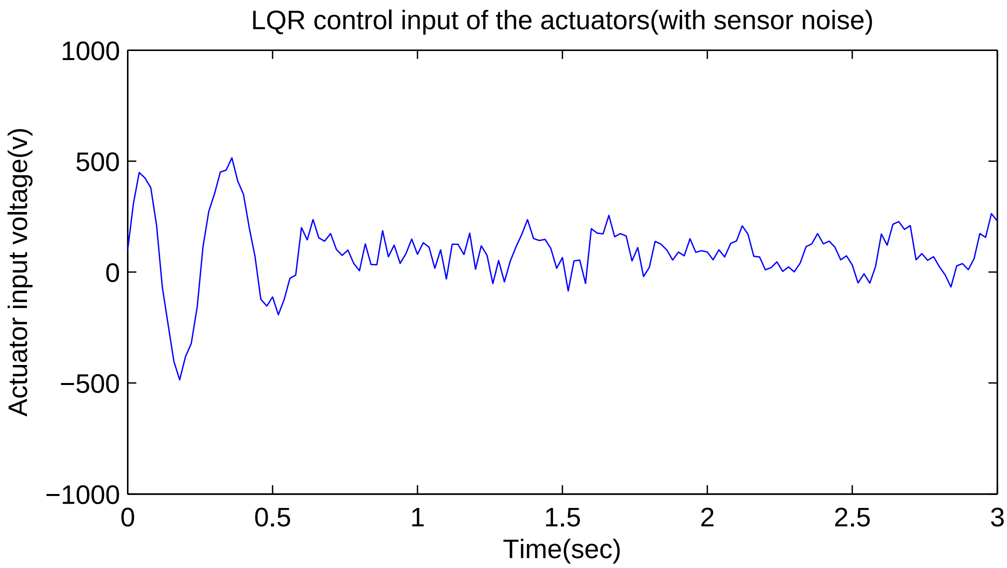

Figure 4–12: LQR control input voltage with noise

4.4.2 Active Buckling Control of a Simply Supported Beam

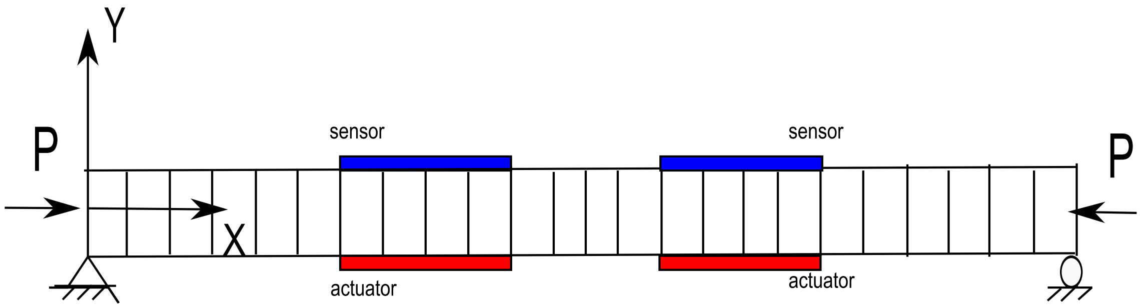

Figure 4–13: Physical model of a SS beam with sensors and actuators

The model studied, Figure 4–13, is a simply supported beam subjected to axial compression. This was also studied by Meressi and Paden [19] with the classical Euler-Bernoulli beam theory. The two sides of the beam are bonded with two pairs of collocated segmented piezoelectric PVDF sensor and actuator. The collocated sensor and actuator are identical in geometry and are the same PVDF piezoelectric material. The material properties and geometric specifications of the beam and the piezo-elements are in Table 4–8. For reducing the number of sensors, the sensor/actuator pairs are placed at $x = L_b/3$ and $x = 2L_b/3$ so that the third mode and its multiples are unobservable.

The beam is divided by 24 elements. Table 4–9 shows the first three critical loads computed using the proposed Timoshenko beam element. Structural damping coefficient of the first mode is assumed as $\zeta = 0.01$ and the other modes can then be obtained by Rayleigh damping method. The first two or four modes

Table 4–8: SS beam and piezoelectric PVDF properties

	beam	PVDF
Length $L_b(mm)$	152.4	25.4
Width $W_b(mm)$	25.4	25.4
Thickness $t_b(mm)$	1.0	0.110
Density (Kg/m^3)	1000.0	1780.0
Elastic modulus(Pa)	5.0×10^9	2.0×10^9
Piezoelectric strain constant $d_{31}(m/v)$	–	21×10^{-12}
Electric permittivity $\epsilon_p(F/m)$	–	1.06×10^{-10}
Maximum electric field $(v/\mu m)$	–	30

Table 4–9: The first three critical loads of the SS beam

Buckling mode	Present Timoshenko element		Exact solution
	24 elements	40 elements	
first	4.5492	4.5019	4.4968
second	18.8442	18.0634	17.9872
Third	45.0316	40.8527	40.4713

minimal realization model are used to realize an approximate reduced order modal model of the system for the first buckling mode or the first two buckling modes control respectively. The modal states are estimated from the two sensor measurements by a dynamic observer. Then corresponding LQR controllers with state observers are designed and active control designs are carried out to stabilize the first buckling mode and the first two buckling modes of the beam respectively. As the unmodeled dynamics can cause instability which are known as control and observation spillovers, an extended modes evaluation model is then constructed to see the spillover effects of the higher order residual modes.

First, an LQR controller is designed to stabilize the first buckling mode. For comparing with the results of [19], it is assumed that the two sensors and the two actuators are serially combined as one respectively so that the sums of their measurements are taken as the system output and control input correspondingly and the derivative of the sensor output can be computed. All even modes are uncontrollable as the symmetrical locations of the actuators while the third mode and its multiples are unobservable as the sensors are placed at nodes of these modes. Thus the first and the fifth modes are the first two modes in a minimal realization of the system. The weight matrices $Q = C^T C, R = I$ and control parameters $\alpha = 10^{14}$, $\beta = 2$ are used for the LQR controller design.

The feedback gain $[G]$ is computed for an axial load exceeding the second critical load P_{cr2}. The first buckling mode is then stabilized to the second buckling load P_{cr2} so that the beam is forced to buckle in the second mode. The stability of the system under any fixed axial loads less than P_{cr2} can be verified [19]. Figures 4–14 and 4–15 are the resulting closed-loop sensor output to a unit impulse load applied on the middlespan of the beam and the control input voltage for an axial compressive load $P = 0.9P_{cr2}$. The time and frequency responses of the unit impulse load for the axial compressive load $P = 0.9P_{cr2}$ in figures 4–16 and 4–17 show the uncontrolled and controlled buckling displacements (the control starting from 0.002 second as seen in the Figure 4–16). Thus the buckling load can be improved to 3.6 times of the first critical load.

Both Figure 4–14 and Figure 4–15 show that the closed-loop responses are consistent with the results of Meressi and Paden [19] for the axial load

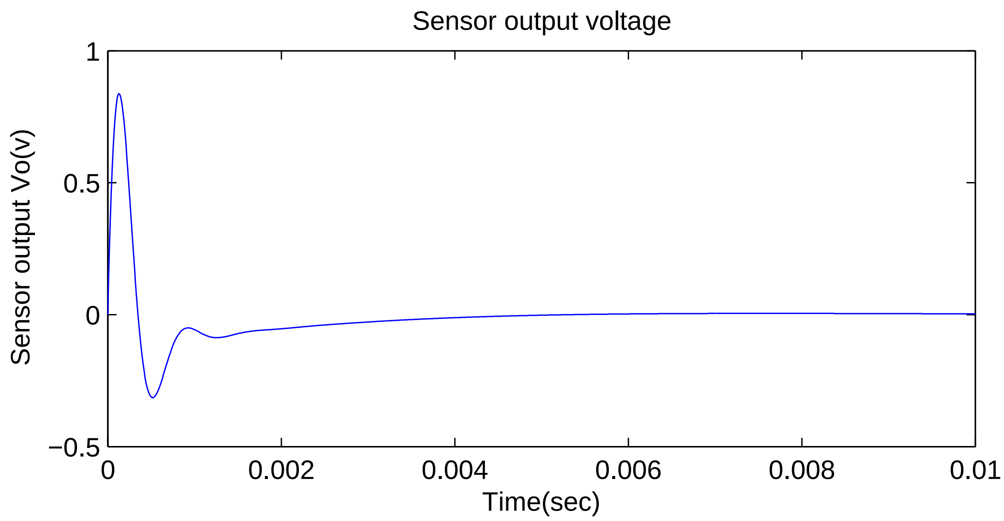

Figure 4–14: Closed-loop sensor output voltage for axial load $P = 0.9P_{cr2}$

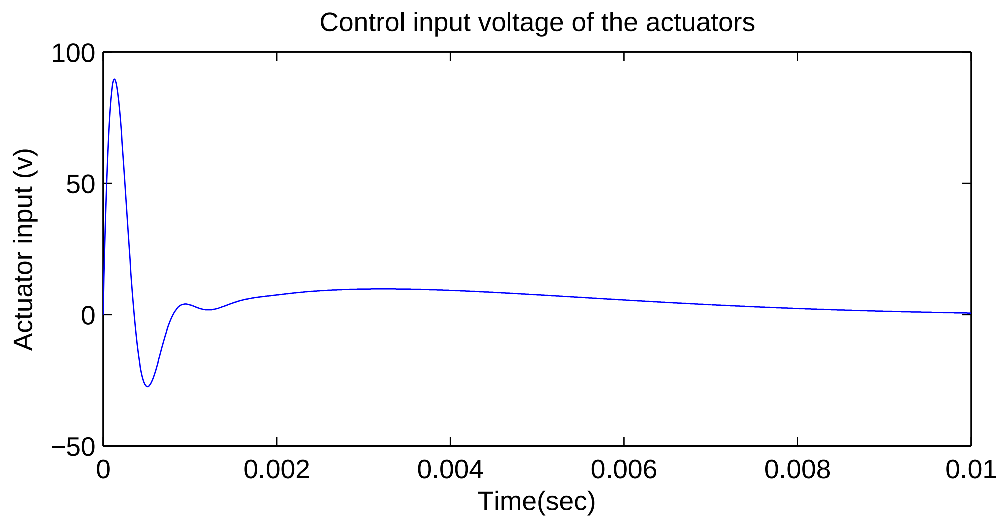

Figure 4–15: Actuator control input voltage for axial load $P = 0.9P_{cr2}$

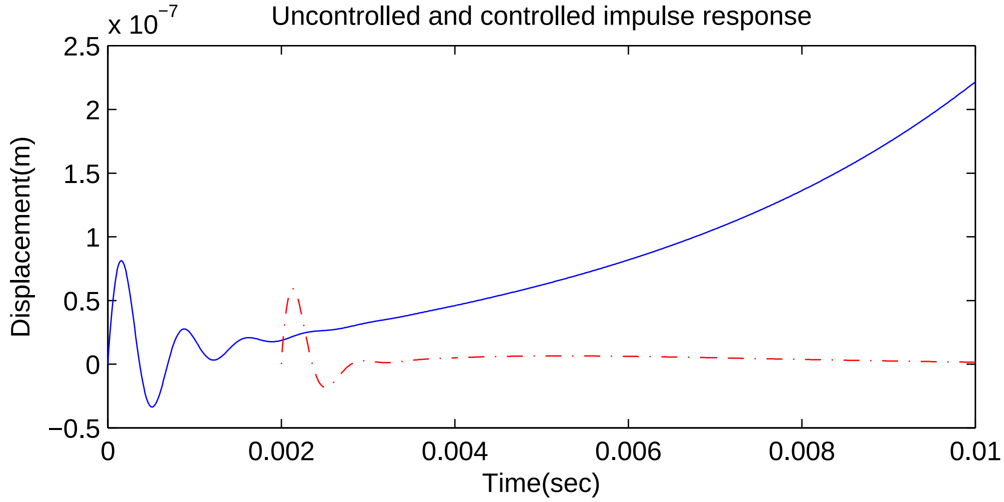

Figure 4–16: Time response of unit impulse load for axial load $P = 0.9P_{cr2}$

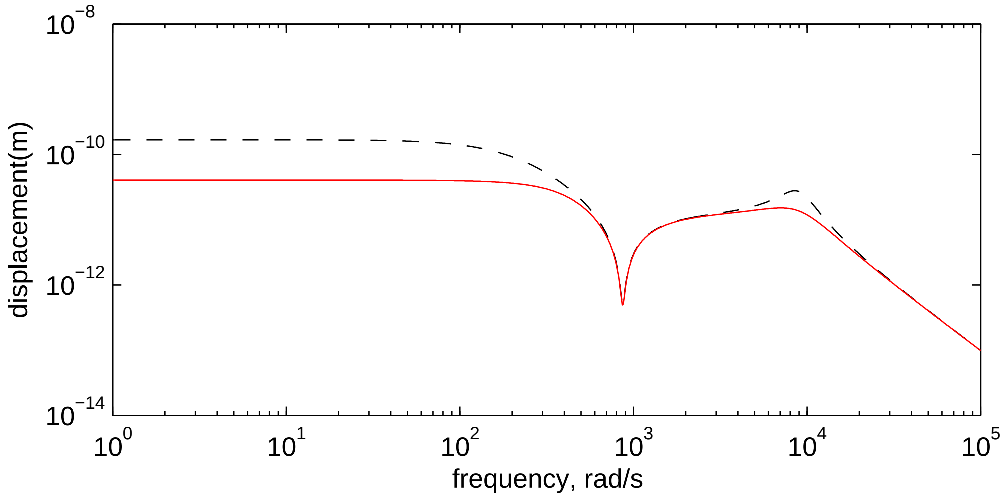

Figure 4–17: Frequency response of unit impulse load for axial load $P = 0.9P_{cr2}$

$P = 3.8P_{cr1}$. Comparing their control peak input voltages (about -90v–60v) with Figure 4–15 (-30v–80v) shows that the segmented actuator pairs (only 1/3 the length of the distributed actuator) at the optimal locations along the beam have better control effects than the distributed actuator.

Next, same as the first mode control, the second mode can be stabilized to the third buckling load P_{cr3}. Only the two sensors and the two actuators are not combined now. For any loads less than P_{cr3}, the stability of the system can also be proved. The first, second, fourth, and fifth modes are the first four modes in a minimal realization of the system. The same weight matrices $Q = C^TC, R = I$ and control parameters $\alpha = 10^{14}$, $\beta = 2$ are used for the LQR controller design.

The resulting closed-loop sensor outputs to the same unit impulse load and the control input voltages of the actuators for the axial compressive load $P = 0.9P_{cr3}$ are shown in figures 4–18, 4–19 and 4–20. Because of the symmetrical locations of the sensors, they have the same output voltage. The two actuators are used to control two different modes separately. The actuator 1 is for the fourth mode control input and the actuator 2 is for the fifth mode control input. The time and frequency responses of the unit impulse load for the axial compressive load $P = 0.9P_{cr3}$ are shown in figures 4–21 and 4–22.

Both the control peak input voltages (about -600v–600v and -1000v–1000v) are in the safe range which below the breakdown voltage ($V_{max} = h_a \times 30.0v/\mu m = 3300v$) for the present 0.110mm thickness PVDF actuator. The time response of the impulse load shows that the displacement dies down after a short settling time when the control is applied. The designed compensator has stabilized the first two

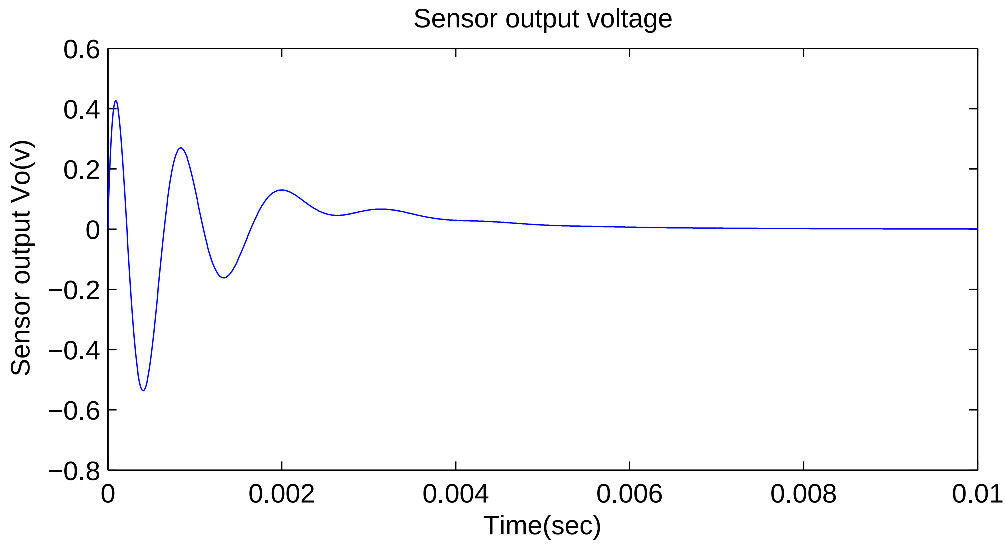

Figure 4–18: Closed-loop sensor output voltage for axial load $P = 0.9P_{cr3}$

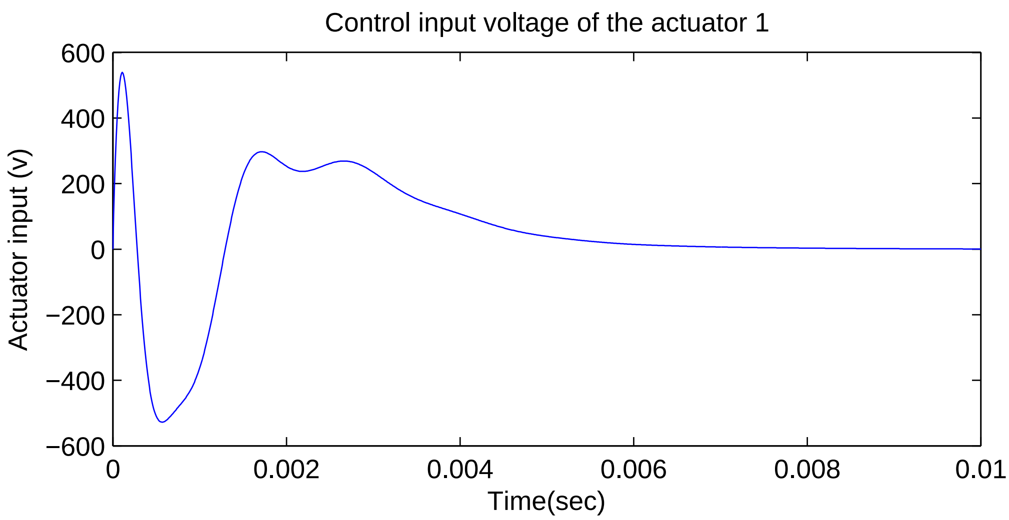

Figure 4–19: Actuator 1 control input voltage for axial load $P = 0.9P_{cr3}$

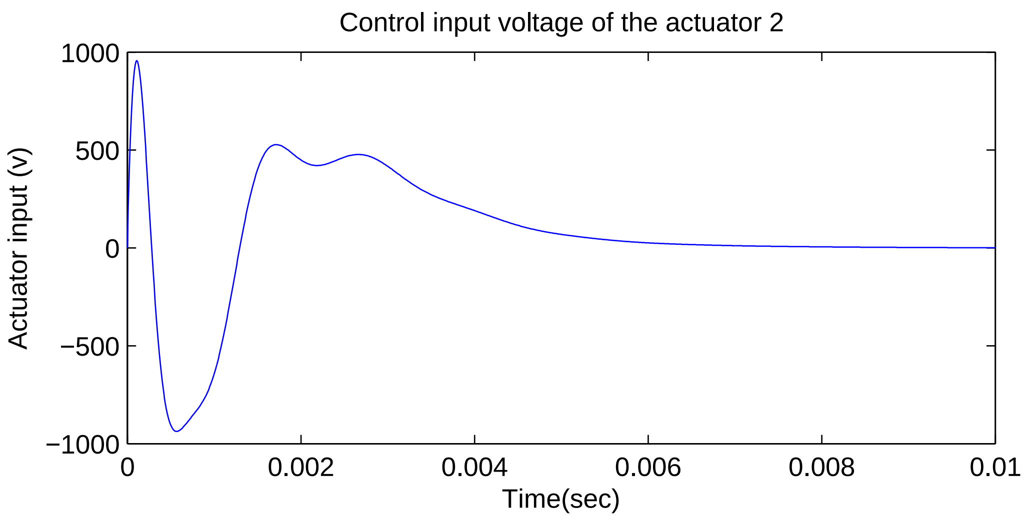

Figure 4–20: Actuator 2 control input voltage for axial load $P = 0.9P_{cr3}$

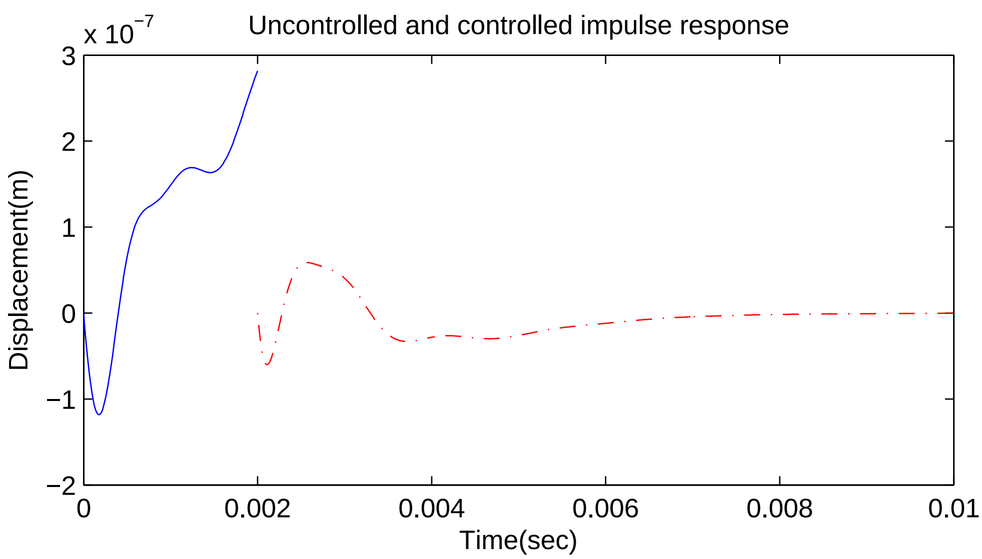

Figure 4–21: Time response of unit impulse load for axial load $P = 0.9P_{cr3}$

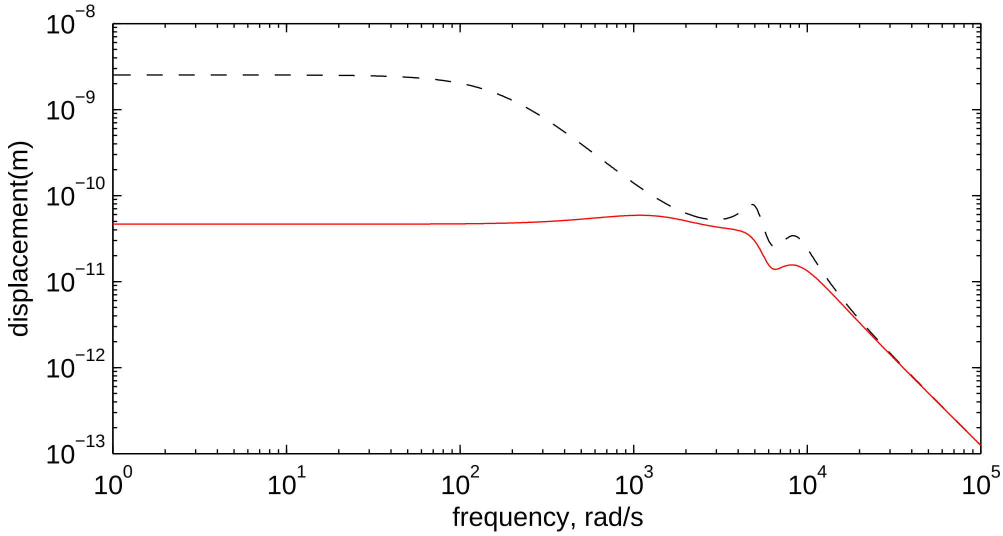

Figure 4–22: Frequency response of unit impulse load for axial load $P = 0.9P_{cr3}$

buckling modes for any $P \leq P_{\max}= P_{cr3}$ and therefore is a robust control. Thus the buckling load is improved to 8.1 times of the first buckling load.

In the above system models, modal control of the beam is based on the first few modes of vibration. However the un-modeled dynamics can cause instability through what are known as control and observation spill-overs. To see the effect of spill-over, an extended evaluation model containing modes 7 and 11 in addition to modes 1 and 5 for the first buckling mode control is realized. The sensor output in Figure 4–23, control input in Figure 4–24 and the time and frequency responses of the unit impulse load for the axial compressive load $P = 0.9P_{cr2}$ in figures 4–25 and 4–26 show that there is no significant effect of the uncontrolled modes on the dynamics of the controlled modes. Therefore the spill-over has not posed a serious problem which is consistent to the theoretical analysis and known simulation results [19]. For the real case control design, the controller can be designed using a low-order reduced model and its stability can be verified for a high-order model.

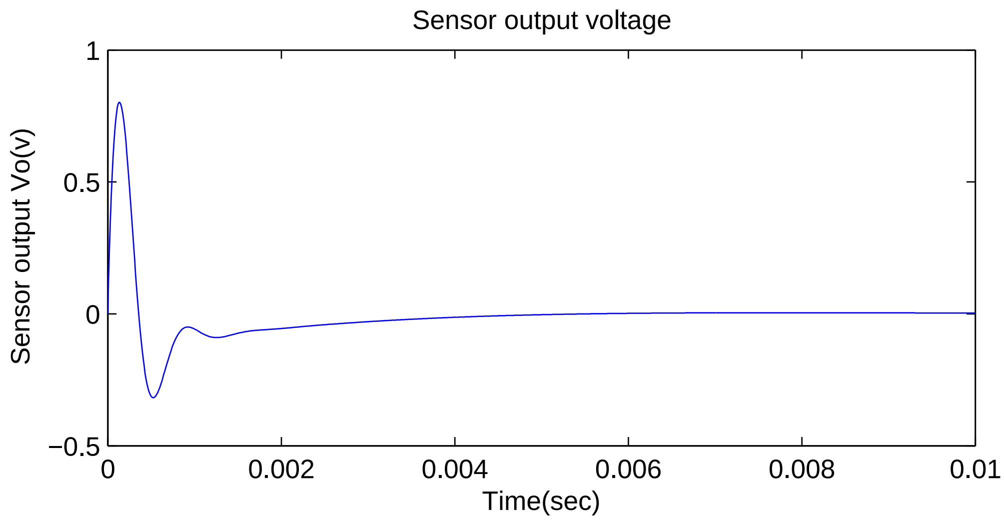

Figure 4–23: Extended model sensor output voltage for axial load $P = 0.9P_{cr2}$

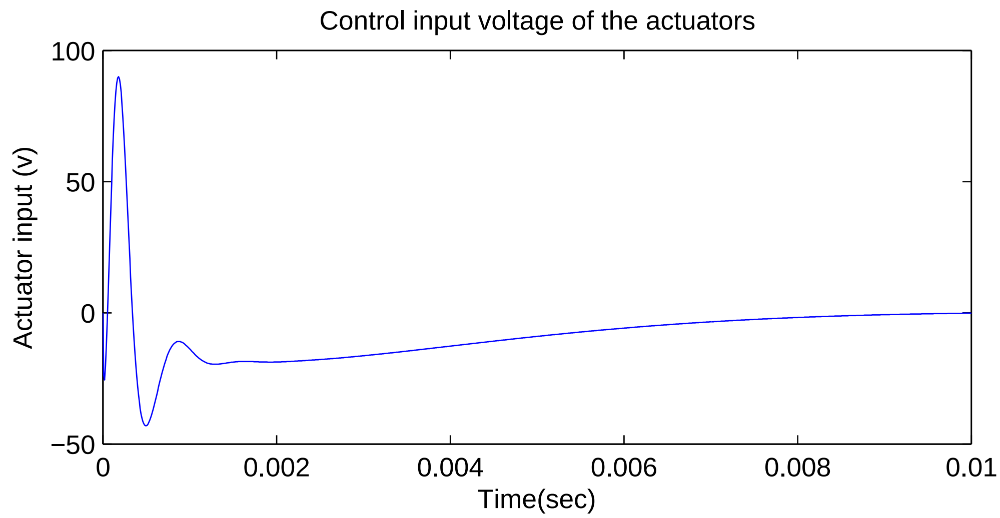

Figure 4–24: Extended model actuator control input for axial load $P = 0.9P_{cr2}$

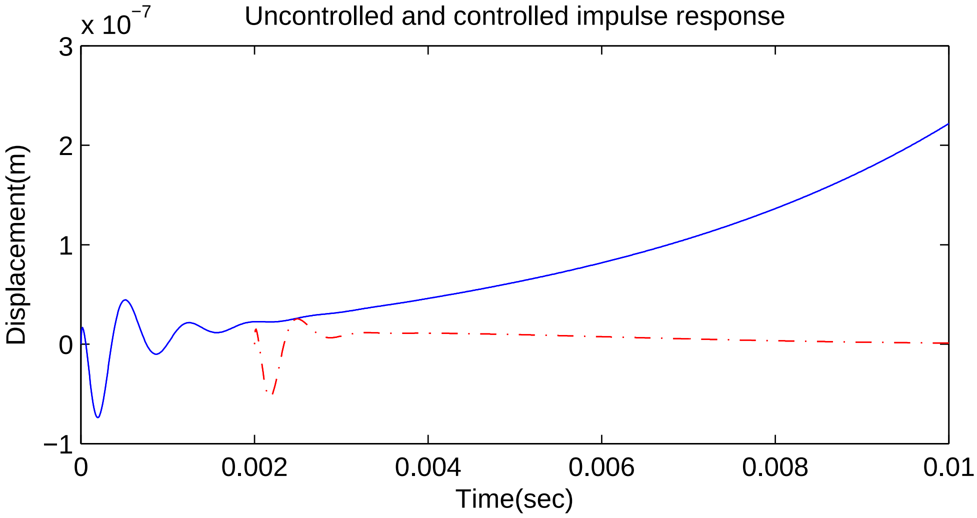

Figure 4–25: Extended model time response for axial load $P = 0.9P_{cr2}$

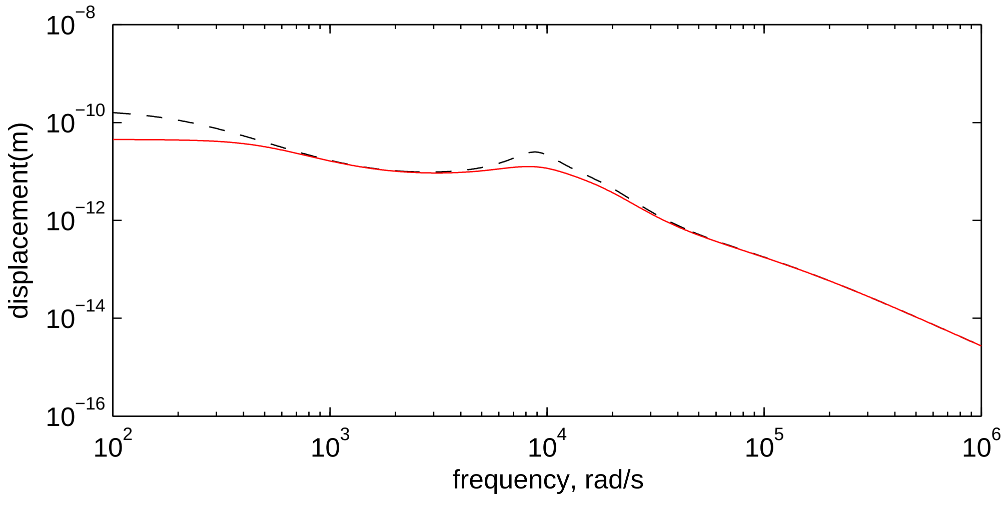

Figure 4–26: Extended model frequency response for axial load $P = 0.9P_{cr2}$

4.4.3 Comparison of Active Vibration and Buckling Control of a Simply Supported Beam

All first 6 modes were included in a reduced-order modal model to design an LQR controller with a dynamic observer for the active vibration and buckling control of the same simply supported beam as in the last case. It is seen that both vibration suppression and buckling control are based on the same dynamic modal mode control method so that the same control designs can be carried out.

The figures 4–27 to 4–42 shown here are for the free vibration suppression without an axial compression load $P = 0$ and with an axial load $P = 0.9P_{cr1}$, the first buckling mode control with $P = 0.9P_{cr2}$, and the first two buckling modes control with $P = 0.9P_{cr3}$ with the same control parameters.

The following comparison results can be observed:

- The Bode plots show that only the first three modes have great significance. The other higher frequencies do not show clear poles.
- The sensor output and the actuator input voltage decreased as the axial compressive load increased till the first buckling load and increased slowly thereafter with the increase in the compressive load.
- Both the uncontrolled and controlled impulse response time and frequency plots show that multimode control with selected minimal targeting modes as in the last case has better overall control results and lower control efforts compared with all the six modes included in this case.
- The buckling control has no difference compared with the vibration suppression. Only the targeting vibration and buckling frequencies, mode shapes,

and damping ratios are varied as the geometric stiffness varied with the increased axial compressive load.

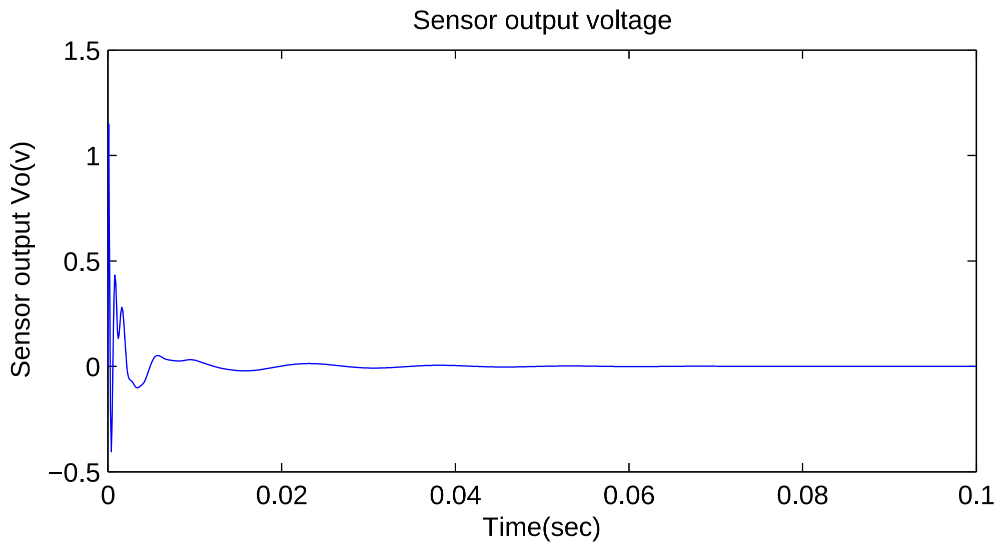

Figure 4–27: Closed-loop sensor output voltage for axial load $P = 0$

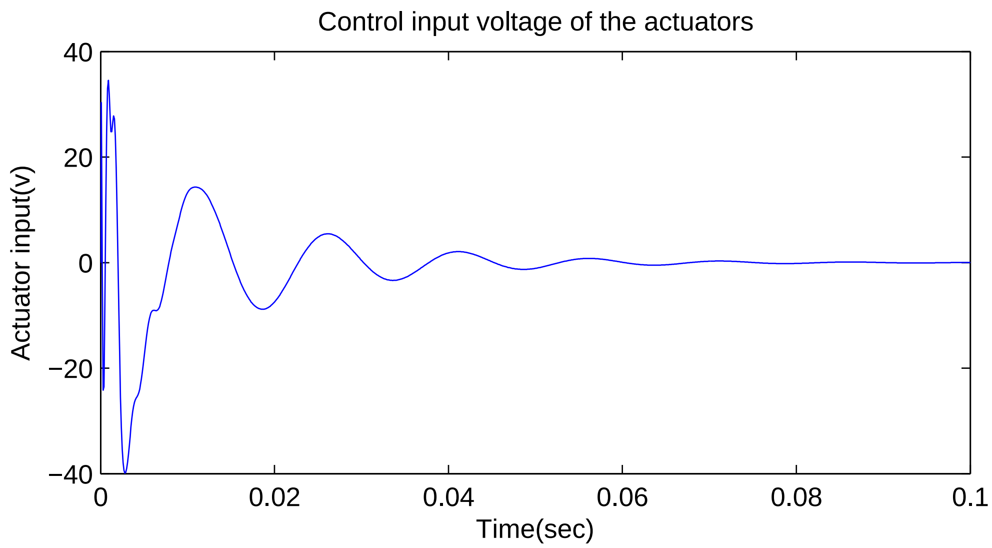

Figure 4–28: Actuator control input voltage for axial load $P = 0$

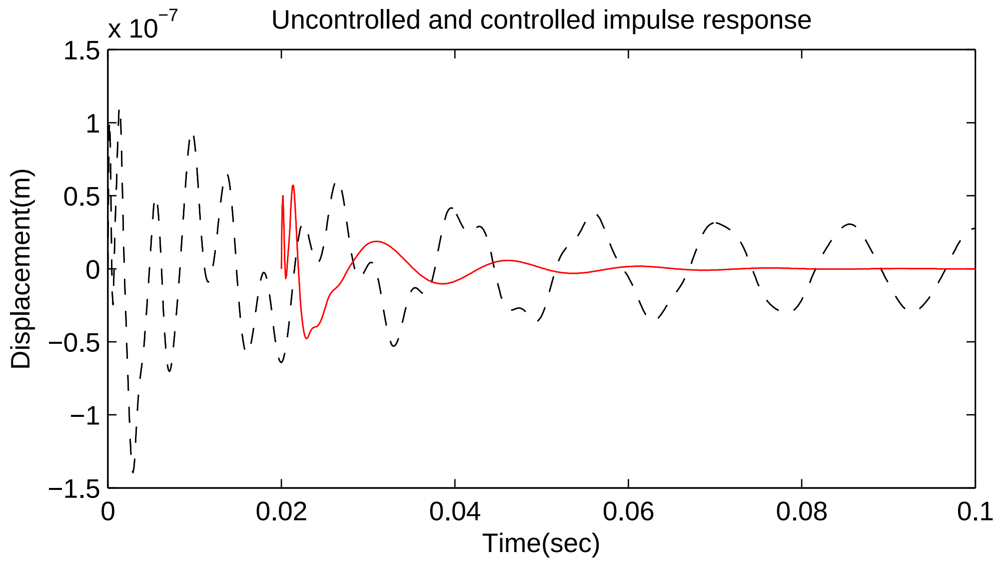

Figure 4–29: Time response of unit impulse load for axial load $P = 0$

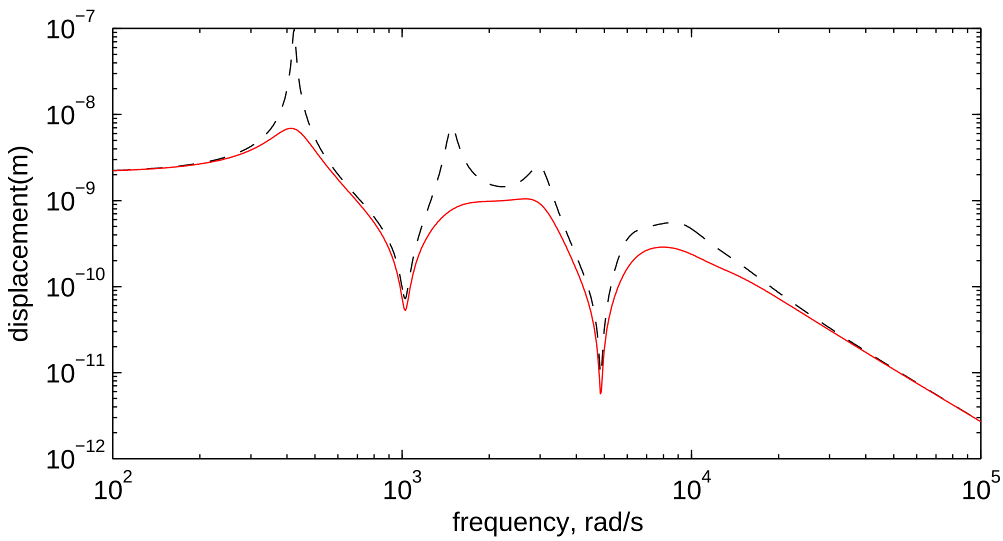

Figure 4–30: Frequency response of unit impulse load for axial load $P = 0$

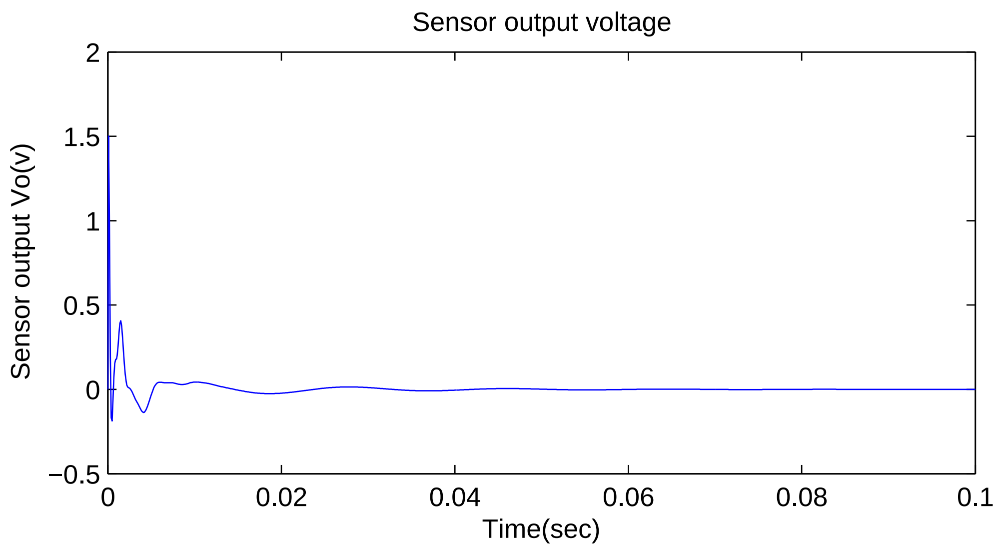

Figure 4–31: Closed-loop sensor output voltage for axial load $P = 0.9P_{cr1}$

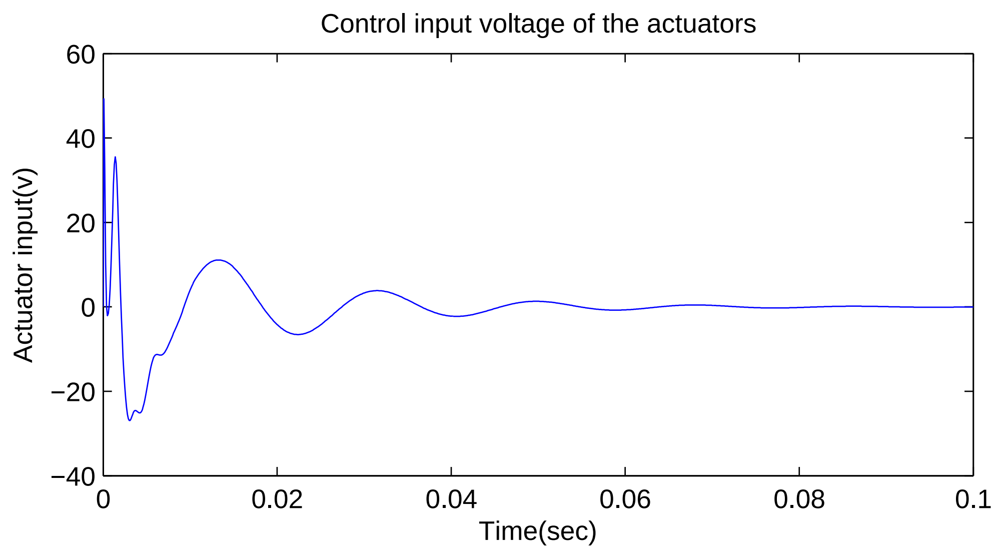

Figure 4–32: Actuator control input voltage for axial load $P = 0.9P_{cr1}$

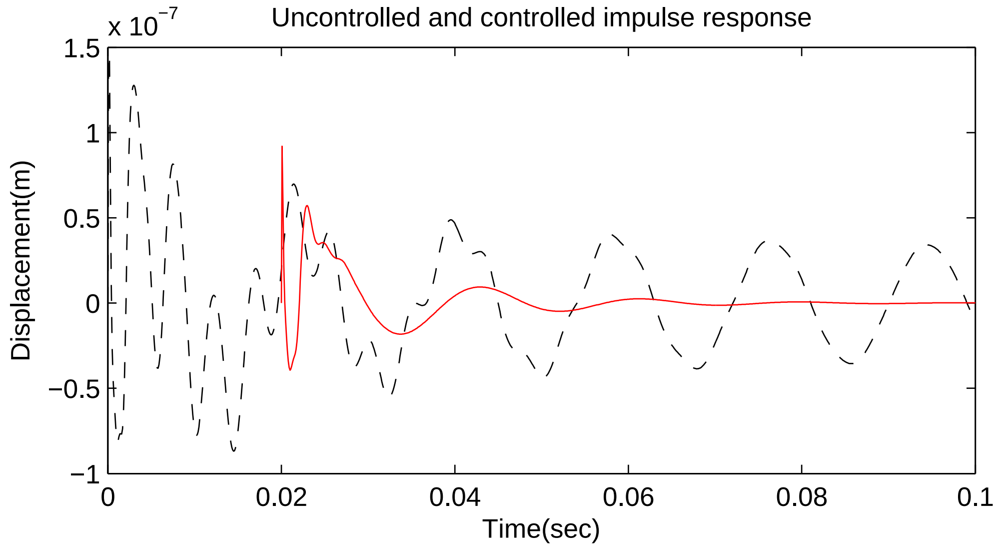

Figure 4–33: Time response of unit impulse load for axial load $P = 0.9P_{cr1}$

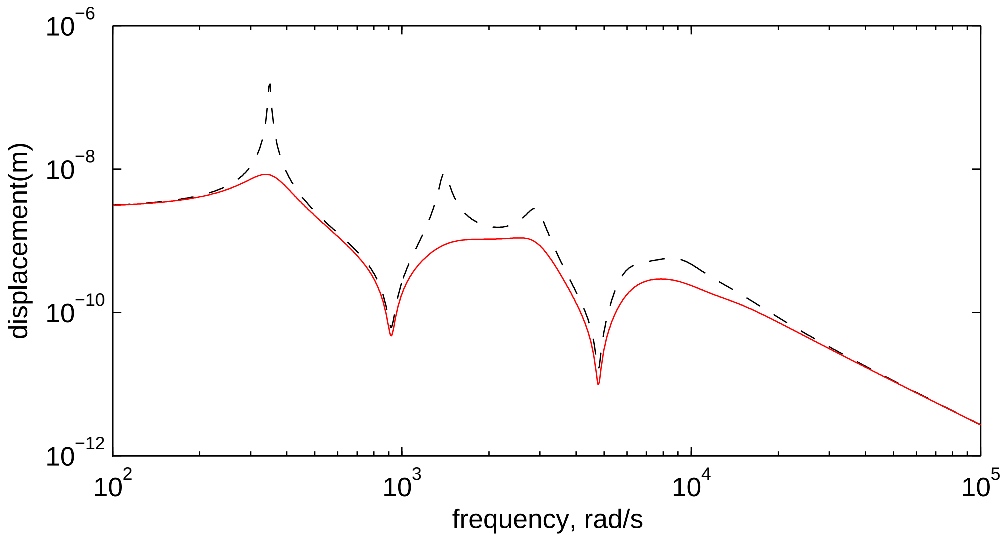

Figure 4–34: Frequency response of unit impulse load for axial load $P = 0.9P_{cr1}$

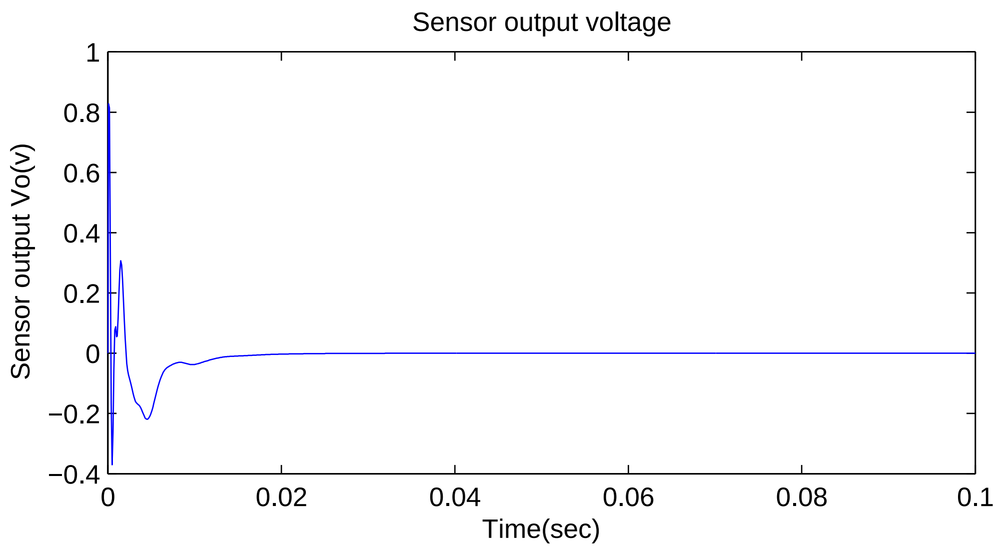

Figure 4–35: Closed-loop sensor output voltage for axial load $P = 0.9P_{cr2}$

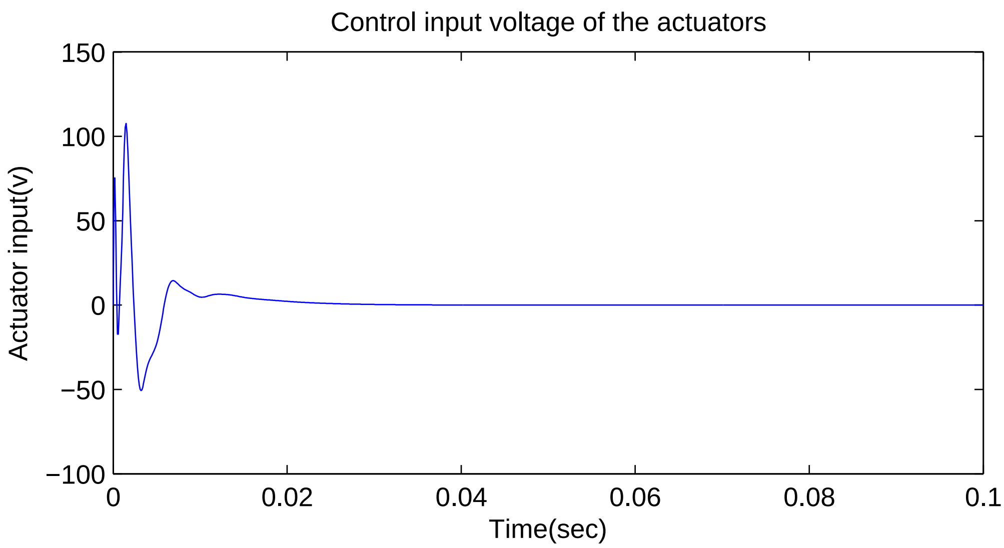

Figure 4–36: Actuator control input voltage for axial load $P = 0.9P_{cr2}$

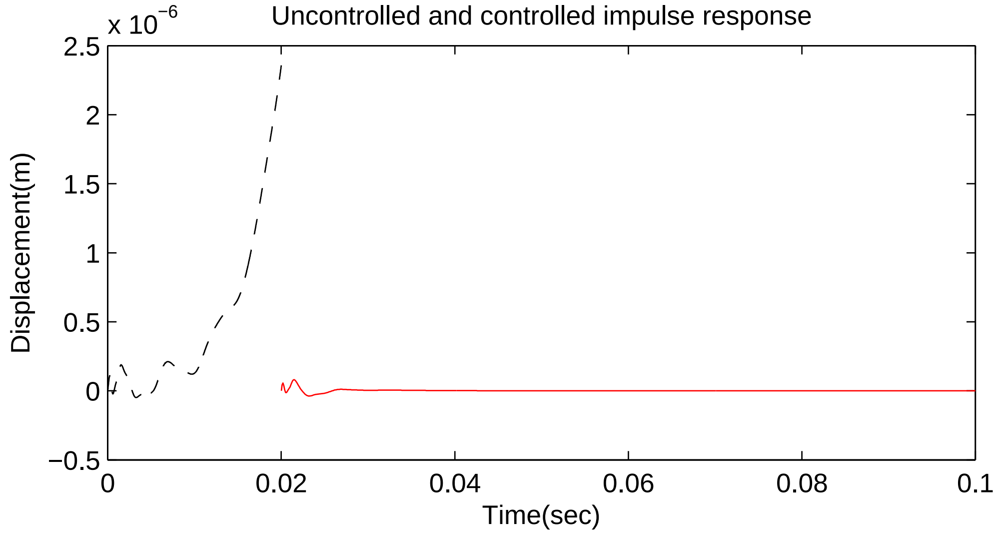

Figure 4–37: Time response of unit impulse load for axial load $P = 0.9P_{cr2}$

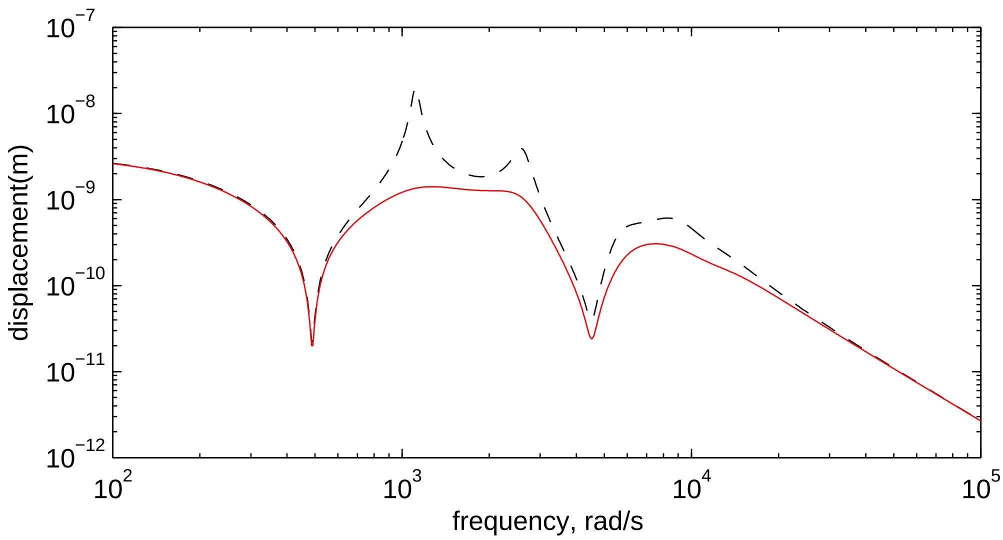

Figure 4–38: Frequency response of unit impulse load for axial load $P = 0.9P_{cr2}$

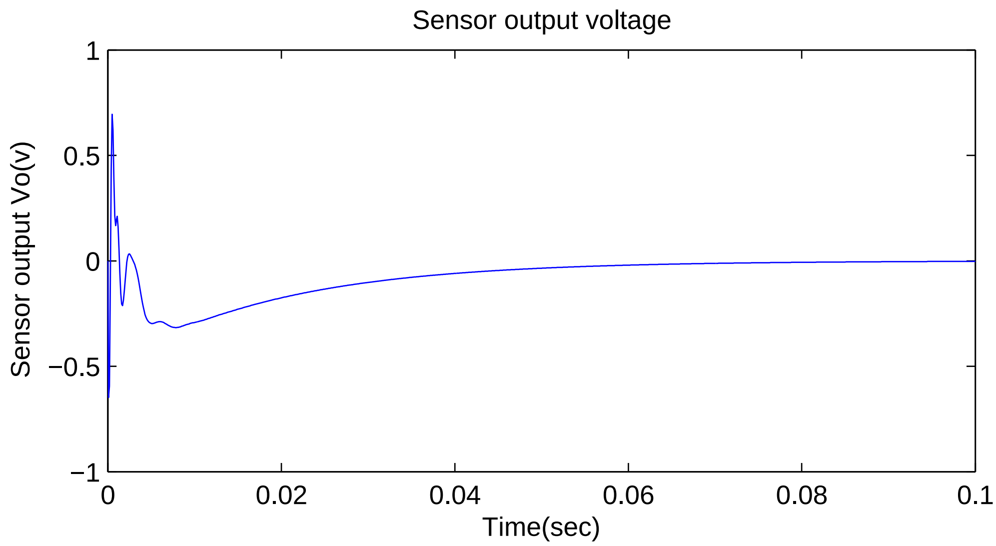

Figure 4–39: Closed-loop sensor output voltage for axial load $P = 0.9P_{cr3}$

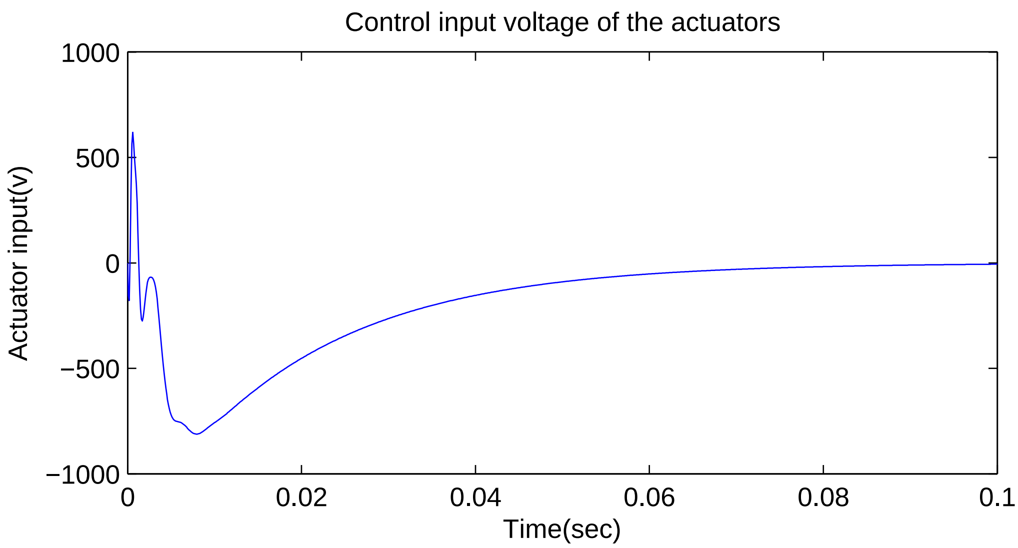

Figure 4–40: Actuator control input voltage for axial load $P = 0.9P_{cr3}$

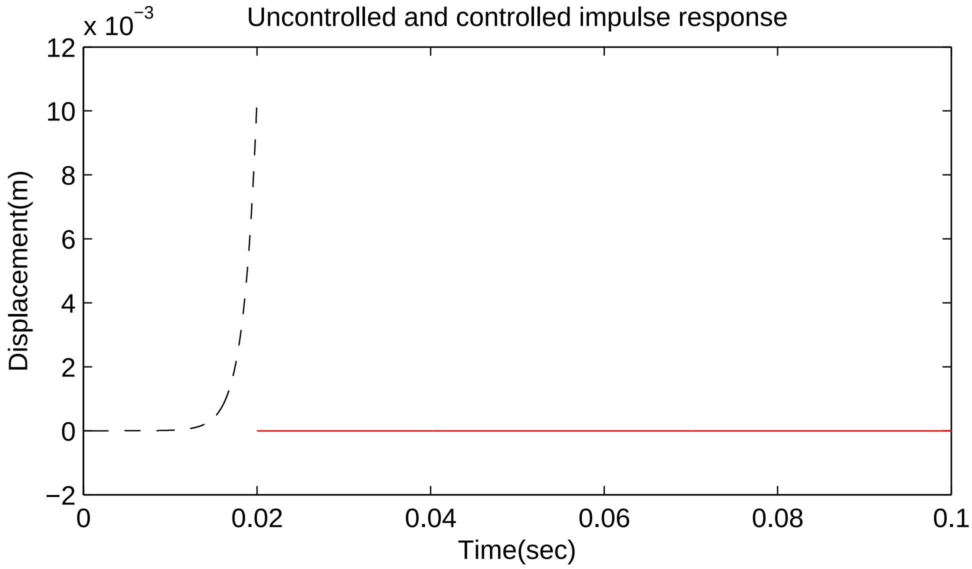

Figure 4–41: Time response of unit impulse load for axial load $P = 0.9P_{cr3}$

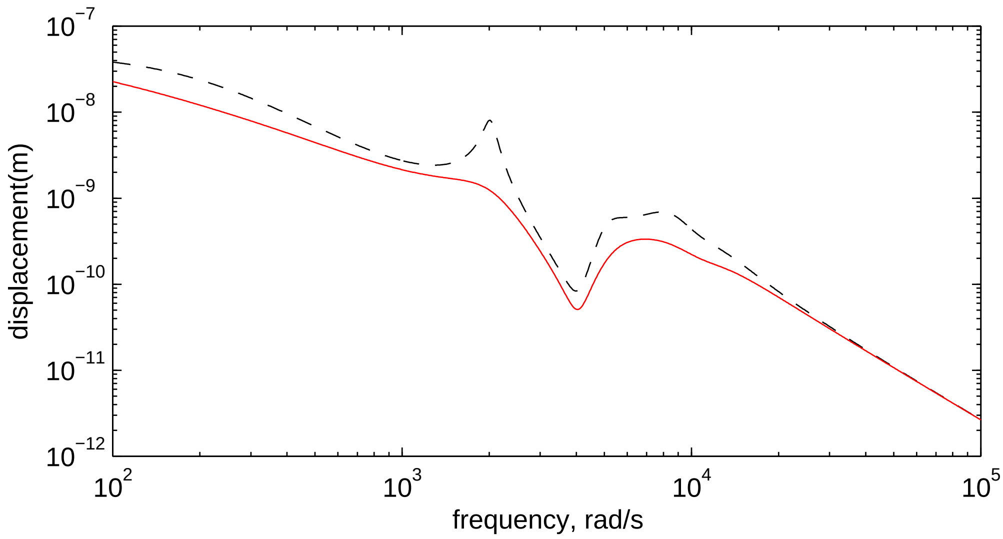

Figure 4–42: Frequency response of unit impulse load for axial load $P = 0.9P_{cr3}$

4.5 Conclusions

1. The finite element analysis and the active control simulation results are consistent with both theoretical analysis results and experimental data.
2. The modal model approach with an LQR/LQG control technique gives very efficient control results to both the vibration suppression and buckling control.
3. The model size reduction technique is necessary in the design of complex real-life structures to determine the smallest model while keeping accurate representation of the frequency response characteristics. Therefore, for large finite element analysis structures, approximate reduced modal model of some selected modes and dynamic states estimator design are a must.
4. The well-tuned LQR optimal controller can trade off requirements of good control results or dynamic performance and smallest control efforts. Therefore, by choosing the state weight matrix Q and control weight matrix R, or the control parameters α and β, the vibration can be damped quickly within the desired settling time while the control voltage remains below the breakdown voltage of the piezoactuators as the worked out cases have shown.
5. The LQG compensator can be designed to eliminate the effect of noise such as the environment disturbances and piezoelectric sensor noise. Numerical simulations show that the required control voltage of LQR controller is very high in the presence of noise, whereas the LQG control voltage is in the acceptable range. Therefore, the LQG technique can compensate for the noise successfully.

6. The segmented piezoelectric actuaors can be designed to control each individual mode independently. As in the case 2, two buckling modes can be controlled simultaneously with two piezoactuators, each has its suitable control input voltage to control the specific mode separately.
7. The first two buckling modes of a simply-supported beam can be stabilized by feedback control using piezoelectric sensors and actuators. Therefore the controlled beam can support a load up to the third buckling load.
8. The designed controller which is based on a fixed axial load P_{cr} can stabilize the modeled modes for any $P \leq P_{cr}$. Therefore, the control is robust to slow load variations.
9. There is no significant effect of the uncontrolled modes on the dynamics of the controlled modes. Therefore, controller can be designed using a low-order model and the stability can be verified for a high-order model.
10. The numerical results show that proper placement of sensors and actuators can maximize the control effect. In the future, more research should be done to design an efficient controlled structure system with optimal piezoelectric patches placements.

CHAPTER 5

Active Vibration and Buckling Control of Piezoelectric Laminated Composite Plates and Shells

5.1 Summary

The basic analysis model of a smart structure is a host structure with surface-bonded or embedded piezoelectric sensor and actuator layers. The sensors, actuators, and substrate are integrated as plies of a laminated structure undergoing consistent deformations. In this chapter, a curvilinear shell element is developed for the vibration and buckling analysis of piezoelectric coupled laminated composite plates and shells.

Finite element formulations are derived based on the nonlinear Layer-Wise Shear Deformation Theory (LWSDT) for laminated doubly curved shells and the linear coupled piezoelectric constitutive equations. The independent kinematic field variables (or the total degrees of freedom of the system), are the three displacements of the base layer and the cross section rotations of all the layers, are discretized with eight-node serendipity quadratic elements. An orthotropic laminated composite material for the base layers combined with an orthotropic piezoelectric material properties for the sensor and actuator layers is formulated to model the material nonlinearities and piezoelectro- mechanical coupling terms.

The proposed finite element analysis model is then applied to both thin and moderately thick piezoelectric laminated plates and shells for both vibration and buckling analysis. The plates, which are flat shells, can be modeled as a special case of the proposed doubly curved shell element by setting the two principal radii of curvature to infinity. Modeling accuracy is evaluated by comparing with theory and experimental results. It has been showed to be consistently good compared with the known results and has some advantages in coping with the nonlinearities and coupling effects.

5.2 Nonlinear Layer-Wise Shear Deformation Theory for Laminated Doubly Curved Shells

For moderately thick laminated composite shells, because of the anisotropic material, there is a bending-stretching coupling. The shear deformation and rotary inertia cannot be neglected. Many shear models have been introduced ,such as First-order Shear Deformation Theory (FSDT), Higher-order Shear Deformation Theory (HSDT), and Layer-Wise Shear Deformation Theory (LWSDT).

The FSDT is based on the Reissner-Mindlin theory. Transverse shear strains are assumed to have a uniform distribution through the shell thickness, which gives uniform shear stresses. There is nonzero shear stresses at top and bottom free surfaces which violates the physical boundary condition. A shear correction factor has to be applied for the free surfaces equilibrium considerations and reduced integration technology is introduced in order not to overestimate the shear forces for the application to the thin shells.

For the HSDT, a cubic variation of in-plane displacement through the thickness results in a quadratic variation of transverse shear strain. This assumed distribution satisfies the traction-free boundary condition on free surfaces but lacks accurate representation of layer-wise variation of shear strain caused by different material properties of laminae as the FSDT.

For the LWSDT, attributed to Reddy [52] as well as Sun and Whitney [53], the in-plane displacement is assumed piecewise linearly along the thickness in each layer. So there is a shear strain variation from layer to layer even though it is assumed uniform in each layer.

Clearly only LWSDT appears appropriate to model the layer-variations of material stiffness. In the case of a single layer, the LWSDT reduces to the FSDT. Many researchers have shown that to analyze the piezoelectric laminated structures accurately, it is important to model the transverse shear of each layer using the LWSDT and incorporate piezoelectric-mechanical coupling effects [54].

A doubly curved laminated shell with rectangular base is considered, as shown in Figure 5–1.

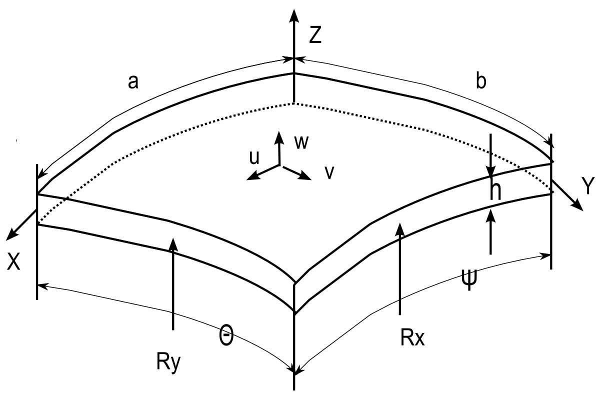

Figure 5–1: Doubly curved shell with rectangular base

The coordinate system is chosen such that x and y are principal lines of curvature of the midplane, which is obtained for $z = 0$, and z is taken always perpendicular to the midplane. The laminated shell is made of a finite number of orthotropic layers, oriented arbitrarily with respect to the shell curvilinear coordinate system (x, y, z). R_x and R_y are the constant principal radii of curvature.

According to the LWSDT, the displacement field in each single layer is based on the first-order shear deformation theory (FSDT). The displacements of a generic point (x, y, z) in k^{th} layer are related to the midplane displacements (u^k, v^k, w) of the layer by [55]

$$\begin{aligned} u_1^k(x,y,z) &= (1+\frac{z}{R_x})u^k(x,y) + z\phi_x^k(x,y) \\ u_2^k(x,y,z) &= (1+\frac{z}{R_y})v^k(x,y) + z\phi_y^k(x,y) \\ u_3^k(x,y,z) &= w(x,y) \end{aligned} \tag{5.1}$$

where the transverse displacement w is assumed to be uniform through the thickness, ϕ_x^k and ϕ_y^k are the rotations of transverse normals about the y and x axes in k^{th} layer respectively. R_x and R_y are constant principal radii of curvature. The plate is the “flat shell” special case with $R_x = R_y = \infty$.

5.3 Piezoelectric Laminated Composite Shell Element

5.3.1 Element Model

The element developed is composed of a nonpiezoelectric composite layer sandwiched by two piezoelectric layers, shown in Figure 5–2. The respective layers are similarly discretized with one element through the thickness regardless of the number of layers for efficient computation. The following two assumptions are made in the element formulation:

1. No slippage between each layer and all sublayers are perfectly bonded.This means that shear continuity is always satisfied.
2. Transverse displacement of each layer is assumed to be the same as the midplane layer.

With LWSDT, the element formulation is derived with full satisfaction of these assumptions.

The local coordinate system of the element is defined so that (ξ, η) are curvilinear and originate at the center of the element midplane.

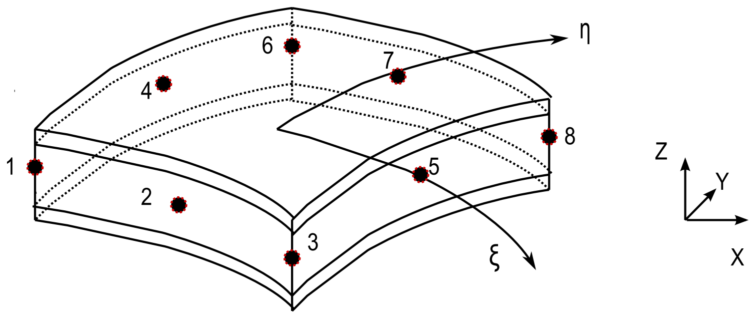

Figure 5–2: Doubly curved 8-node quadratic serendipity composite shell element

By using the constraining equations, the in-plane displacements of layers other than the midplane layer can be defined in terms of the in-plane displacements of the midplane layer and the cross-sectional rotations of all layers. Numbers of the total system degrees of freedom are reduced and the independent nodal degrees of freedom vector is the $\{q\}$ (equation (2.41)).

5.3.2 Element Shape Functions

Using standard discretization techniques, the element independent kinematic field variables vector q (2.41) can be approximated by element shape functions as

$$\{q\} = \sum_{i=1}^{ne}(\begin{bmatrix} N_i & 0 & 0 & \cdots & 0 \\ 0 & N_i & 0 & \cdots & 0 \\ 0 & 0 & N_i & \cdots & 0 \\ \vdots & \vdots & \vdots & \ddots & \cdots \\ 0 & 0 & 0 & \cdots & N_i \end{bmatrix}\{q_i\}) = [N]\{u\} \tag{5.2}$$

with $[N] = [[N_1], [N_2], \cdots, [N_{ne}], [N_i] = N_i[I]]$, and $\{u\} = (\{q_1\}^T, \{q_2\}^T, \cdots, \{q_{ne}\}^T)^T$. where ne is the number of nodes per element. N_i and $\{q_i\}$ are the shape function and the independent variables vector for the i^{th} node respectively. $[I]$ is a $ni \times ni$ identity matrix. ni is the number of element independent variables $\{q\}$. The superscript e which denotes the parameter at the element level is dropped here for simplicity.

A eight-node serendipity isoparametric quadrilateral shell element is implemented here. Natural coordinates and nodal convention of the shape function are shown in Figure 5–2. Nodal shape functions are derived using the same interpolation polynomial for both the coordinates and kinematic fields as the following:

$$\widehat{u} = \alpha_1 + \alpha_2\xi + \alpha_3\eta + \alpha_4\xi^2 + \alpha_5\xi\eta + \alpha_6\eta^2 + \alpha_7\xi^2\eta + \alpha_8\xi\eta^2 \tag{5.3}$$

Derived nodal shape functions are,

$$N_i = \frac{1}{4}(1+\xi\xi_i)(1+\eta\eta_i)(\xi\xi_i+\eta\eta_i-1) \quad (i=1,3,6,8) \tag{5.4}$$

$$N_i = \frac{1}{2}(1-\xi^2)(1+\eta\eta_i) \quad (i=2,7) \tag{5.5}$$

$$N_i = \frac{1}{2}(1+\xi\xi_i)(1-\eta^2) \quad (i=4,5) \tag{5.6}$$

Since all nodes are defined at the element boundary, the serendipity element makes the construction of the element connectivity matrix straight forward.

5.3.3 Displacement-Strain Relations

Using the displacement equation (5.1) of LWSDT, strain equations for the k^{th} layer can be written as

$$\{\epsilon^k\} = \left\{ \begin{array}{c} \epsilon_m^k \\ 0 \end{array} \right\} + \left\{ \begin{array}{c} z\epsilon_b^k \\ \epsilon_s^k \end{array} \right\} \tag{5.7}$$

where the mid-surface membrane strains ϵ_m^k, the bending strains ϵ_b^k, and the shear strains ϵ_s^k are [55]

$$\{\epsilon_m^k\} = \left\{ \begin{array}{c} u_{,x}^k + (w/R_x) \\ v_{,y}^k + (w/R_y) \\ u_{,y}^k + v_{,x}^k \end{array} \right\} \tag{5.8}$$

$$\{\epsilon_b^k\} = -\left\{ \begin{array}{c} \theta_{x,x}^k \\ \theta_{y,y}^k \\ \theta_{x,y}^k + \theta_{y,x}^k - u_{,y}^k/R_x - v_{,x}^k/R_y \end{array} \right\} \tag{5.9}$$

$$\{\epsilon_s^k\} = \left\{ \begin{array}{c} -\theta_x^k + w_{,x} - u^k/R_x \\ -\theta_y^k + w_{,y} - v^k/R_y \end{array} \right\} \tag{5.10}$$

Substituting the discretized element independent displacement (5.2) to the constraint relations (2.39), element constrained displacement field can also be represented in terms of the element nodal coordinate vector u as:

$$\{\underline{q}\} = [C_q^k][S^k][N]\{u\} \tag{5.11}$$

where, S^k is the operators matrix related to the shell curvature part, $[C_q^k]$ is the stored constraining relations truncated from C_q matrix for the k^{th} layer.

Substituting these discretized element displacements $\{q\}$ (5.2) and $\{\underline{q}\}$ (5.11) into the above strains equation (5.7), element strains can be written as:

$$\{\epsilon^k\} = [C_q^k][H^k][N]\{u\} = [B^k]\{u\} \tag{5.12}$$

where, H^k represents both the strain differential operators matrix and the operators matrix S^k.

5.3.4 Potential and Kinetic Energy

The element mechanical strain energy for the k^{th} layer of composite shell is

$$\begin{gathered} U_\varepsilon^k = \frac{1}{2}\int_0^a\int_0^b\int_{z_{k-1}^e}^{z_k^e}(\sigma_{xx}^k\epsilon_{xx}^k + \sigma_{yy}^k\epsilon_{yy}^k + \tau_{xy}^k\gamma_{xy}^k + \kappa_x^2\tau_{xz}^k\gamma_{xz}^k + \kappa_y^2\tau_{yz}^k\gamma_{yz}^k) \\ \times(1+z/R_x)(1+z/R_y)dxdydz \end{gathered} \tag{5.13}$$

where, the shear correction factor $\kappa_x^2 = \kappa_y^2 = \frac{5}{6}$.

As in the previous chapters, $h-$type equation (2.7) is chosen as the actuator equation and $g-$type equation (2.6) is chosen as the sensor equation. These piezoelectric constitutive equations can be extended to the two dimensional plate/shell structure as:

$$\begin{Bmatrix} \sigma_{11}^{pz} \\ \sigma_{22}^{pz} \end{Bmatrix} = \begin{bmatrix} \frac{E_1^{pz}}{1-\nu_{12}^{pz}\nu_{21}^{pz}} & \frac{E_1^{pz}\nu_{21}^{pz}}{1-\nu_{12}^{pz}\nu_{21}^{pz}} \\ \frac{E_2^{pz}\nu_{12}^{pz}}{1-\nu_{12}^{pz}\nu_{21}^{pz}} & \frac{E_2^{pz}}{1-\nu_{12}^{pz}\nu_{21}^{pz}} \end{bmatrix} \begin{Bmatrix} \epsilon_{11}^{pz} \\ \epsilon_{22}^{pz} \end{Bmatrix} - \begin{bmatrix} h_{31} \\ h_{32} \end{bmatrix} \{D_3\} \tag{5.14}$$

$$E_3 = \begin{bmatrix} -g_{31} & -g_{32} \end{bmatrix} \begin{Bmatrix} \sigma_{11}^{s} \\ \sigma_{22}^{s} \end{Bmatrix} + \beta_{33}^{T}\{D_3\} \tag{5.15}$$

where, E_1^{pz} and E_2^{pz} are Young's moduli of the piezo layer in the 1 and 2 directions, ν_{12}^{pz} is Poisson's ratio, D_3 and E_3 are the electric displacement and electric field in the 3 direction, h_{31}, h_{32}, g_{31}, and g_{32} are the piezoelectric constants in 31 and 32 directions and $\sigma_{33} = D_1 = D_2 = E_1 = E_2 = 0$ is assumed.

From equations (2.20), (5.14), and (5.15), the element electromechanical couple potential energy of the piezo layer can be written as:

$$U_{pc} = \frac{1}{2}\int_{\Omega^e} \left[\int_{z_{k-1}^e}^{z_k^e} \begin{bmatrix} -h_{31} & -h_{32} \end{bmatrix} \begin{Bmatrix} \epsilon_{11}^{pz} \\ \epsilon_{22}^{pz} \end{Bmatrix} \{D_3\} dz \right] dxdy \tag{5.16}$$

From equations (2.19), (5.14), and (5.15), the element dielectric potential energy of the piezo layer can be written as:

$$U_{pe} = \frac{1}{2}\int_{\Omega^e} \left[\int_{z_{k-1}^e}^{z_k^e} (\beta_{33}^{T} + g_{31}h_{31} + g_{32}h_{32})\{D_3\}^2 dz \right] dxdy \tag{5.17}$$

From equation (2.17), the element kinetic energy for the k^{th} layer of the composite shell, including rotary inertia, can be written as:

$$T_{se}^k = \frac{1}{2}\rho^k \int_0^a \int_0^b \int_{z_{k-1}^e}^{z_k^e} (\dot{u}_1^2 + \dot{u}_2^2 + \dot{u}_3^2) \times (1 + z/R_x)(1 + z/R_y) dxdydz \tag{5.18}$$

where ρ^k is the mass density of the k^{th} layer of the shell and the overdot denotes time derivative.

By substituting the displacement equation (5.1) into (5.18), and assuming uniform thickness and the same density for all the layers of a laminate in particular, the element total kinetic energy for all layers can be simplified as:

$$\begin{aligned} T_s^k = \tfrac{1}{2}\textstyle\int_0^a\int_0^b &\{\rho h(\dot{u}^2 + \dot{v}^2 + \dot{w}^2) + \tfrac{\rho h^3}{12}\left[\dot{\phi}_x^2 + \dot{\phi}_y^2 + 2\dot{\phi}_x\dot{u}(\tfrac{2}{R_x} + \tfrac{1}{R_y})\right] \\ +\tfrac{\rho h^3}{12} &\left[2\dot{\phi}_y\dot{v}(\tfrac{1}{R_x} + \tfrac{2}{R_y}) + 3(\tfrac{\dot{u}^2}{R_x} + \tfrac{\dot{v}^2}{R_y})(\tfrac{1}{R_x} + \tfrac{1}{R_y}) + \tfrac{\dot{w}^2}{R_x R_y}\right] + O(h^4)\}dxdy \end{aligned} \tag{5.19}$$

where, h is the shell thickness.

5.3.5 Element Stiffness and Mass Matrices

According to the Hamilton principle (2.11), the Hamilton equation for the piezoelectric laminated composite shell can be written as

$$\delta \int_{t_1}^{t_2} [T_s^k - \sum_{k=1}^{n}(U_\varepsilon^k) - U_{p\varepsilon} - U_{pe} - U_{pc} + W_d]dt = 0 \tag{5.20}$$

By substituting the discretized element independent displacement (5.2) and element constaining layers displacement (5.11) into the element kinetic energy (5.18) and substituting strains (5.12) and stress-strain relation (2.49) into the mechnical strain energy equation (5.13) and electromechanical couple potential energy of the piezo layer (5.16), the application of the Hamilton principle (5.20) yields element governing dynamic equations of motion as:

$$[M]^e\{\ddot{u}^e\} + [K_{uu}]^e\{u^e\} + [K_{uQ}^a]^e\{Q^a\}^e + [K_{uQ}^s]^e\{Q^s\}^e = \{F_M\}^e \tag{5.21}$$

where, $\{u^e\}$ is the element nodal displacement, $\{Q^a\}^e$ is the element actuator charge, $\{Q^s\}^e$ is the element sensor charge, and $\{F_M\}^e$ is the applied element mechanical external force.

The lement mass matrix is

$$[M]^e = \int_{\Omega^e} \left[\int_{z_{k-1}^e}^{z_k^e} \sum_{k=1}^{n} (\rho^k [N]^T [S^k]^T [C_q^k]^T [C_q^k][S^k][N]) dz \right] dxdy \tag{5.22}$$

The element stiffness matrices can be written as

$$[K_{uu}]^e = \int_{\Omega^e} \left[\int_{z_{k-1}^e}^{z_k^e} \sum_{k=1}^{n} ([N]^T [H^k]^T [C_q^k]^T [Q^k][C_q^k][H^k][N]) dz \right] dxdy \tag{5.23}$$

By applying the membrane, bending, and shear strains equations (5.8), (5.9), (5.10), the corresponding strain-displacement matrix membrane component $[B_m]$, bending component $[B_b]$, shear component $[B_s]$ can be obtained. Then, element stiffness can be integrated explicitly as

$$[K_{uu}]^e = [K_{mm}]^e + [K_{mb}]^e + [K_{bm}]^e + [K_{bb}]^e + [K_{ss}]^e \tag{5.24}$$

which $[K_{mm}]^e$ is the membrane part of the stiffness matrix, $[K_{mb}]^e$ and $[K_{bm}]^e$ are the membrane-bending coupling components, $[K_{bb}]^e$ is the bending part, and $[K_{ss}]^e$ is the shear part, defined as

$$[K_{mm}]^e = \sum_{k=1}^{n} \int_{S^e} [B_m]^T [A_{ij}][B_m] dxdy \ (i, j, 1, 2, 6) \tag{5.25}$$

$$[K_{mb}]^e = \sum_{k=1}^{n} \int_{S^e} [B_m]^T [B_{ij}][B_b] dxdy \tag{5.26}$$

$$[K_{bm}]^e = \sum_{k=1}^{n} \int_{S^e} [B_b]^T [B_{ij}][B_m] dxdy \tag{5.27}$$

$$[K_{bb}]^e = \sum_{k=1}^{n} \int_{S^e} [B_b]^T [D_{ij}][B_b] dxdy \tag{5.28}$$

$$[K_{ss}]^e = \sum_{k=1}^{n} \int_{S^e} [B_s]^T [A_{ij}][B_s] dxdy \ (i, j, 4, 5) \tag{5.29}$$

where, extensional, bending-stretching coupling, and flexural stiffness coefficients matrix of the laminate are (2.57), (2.58), and (2.59); transverse shear stiffness coefficients matrix of the laminate is (2.60).

Element coupled stiffness matrices are

$$[K^a_{uQ}]^e = \frac{1}{2S^e} \int_{\Omega^e} \left[\int_{z^e_{k-1}}^{z^e_k} \begin{bmatrix} -h_{31} & -h_{32} \end{bmatrix} [C^a_q][H^a][N])dz \right] dxdy \tag{5.30}$$

$$[K^s_{uQ}]^e = \frac{1}{2S^e} \int_{\Omega^e} \left[\int_{z^e_{k-1}}^{z^e_k} \begin{bmatrix} -h_{31} & -h_{32} \end{bmatrix} [C^s_q][H^s][N])dz \right] dxdy \tag{5.31}$$

where, S^e is the element area of the piezo layer in the $xy-$plane.

Element electric stiffness matrix for the piezo layer, or the dielectric inverse capacitance term can be explicitly written as

$$[K^{pz}_{QQ}]^e = \frac{h_{pz}}{S^e}(\beta^T_{33} + g_{31}h_{31} + g_{32}h_{32}) \tag{5.32}$$

5.3.6 Control Equations of Motion

For the vibration analysis and control of the piezoelectric laminated shell, after assembly of element matrices and vectors of the previous element dynamic governing equation (5.21) with the damping term added, the global governing equation can be written as:

$$[M]\{\ddot{U}\} + [C_d]\{\dot{U}\} + [K_{UU}]\{U\} + [K^a_{UQ}]\{Q^a\} + [K^s_{UQ}]\{Q^s\} = \{F_M\} \tag{5.33}$$

Considering the same three layers piezoelectric structure as in Figure 2–4, substituting the sensor charge (2.61) and actuator charge (2.62), the global dynamic governing equations of the piezoelectric laminated shell can be written in the same way as (2.63).

For the buckling analysis and control of the piezoelectric laminated shell, the global dynamic buckling equations are

$$[M]\{\ddot{U}\} + [C_d]\{\dot{U}\} + [K^\star]\{U\} - P[K_G]\{U\} = \{F_M\} - [K^a]\{\Phi_a\} \tag{5.34}$$

where, the new term is the geometric stiffness matrix K_G and P is the in-plane buckling load.

Considering small lateral displacement of the piezoelectric laminated plate ($R_x = R_y = \infty$), the strain energy for an initially stressed plate with in-plane compressive stress load $\widehat{\sigma}^0$ is [59]

$$U_G = \int_V (\widehat{\sigma}^0)^T \varepsilon^L dV \tag{5.35}$$

after neglecting terms with third and higher powers in displacement gradients,

$$\varepsilon^L = \begin{bmatrix} \frac{1}{2}((\frac{\partial u}{\partial x})^2 + (\frac{\partial v}{\partial x})^2 + (\frac{\partial w}{\partial x})^2) \\ \frac{1}{2}((\frac{\partial u}{\partial y})^2 + (\frac{\partial v}{\partial y})^2 + (\frac{\partial w}{\partial y})^2) \\ \frac{\partial u}{\partial x}\frac{\partial u}{\partial y} + \frac{\partial v}{\partial x}\frac{\partial v}{\partial y} + \frac{\partial w}{\partial x}\frac{\partial w}{\partial y} \end{bmatrix} \tag{5.36}$$

Substituting the discretized displacement (5.2) into (5.36) and integrating over the layers, will yield element geometric stiffness matrix K_G^e. After element assembly, the global geometric stiffness matrix K_G can be written as [59]:

$$K_G = K_{Gb} + K_{Gs} \tag{5.37}$$

In the above, the bending contribution is given by

$$K_{Gb} = \int_{-1}^{1}\int_{-1}^{1} G_b^T \sigma^0 G_b h \left|J\right| d\xi d\eta \tag{5.38}$$

where,

$$\sigma^0 = \begin{bmatrix} \sigma_x^0 & \tau_{xy}^0 \\ \tau_{xy}^0 & \sigma_y^0 \end{bmatrix} \tag{5.39}$$

and for a given node i,

$$G_b^i = \begin{bmatrix} \frac{\partial N_i}{\partial x} & 0 & 0 \\ \frac{\partial N_i}{\partial y} & 0 & 0 \end{bmatrix} \tag{5.40}$$

The shear contribution is given as

$$K_{Gs} = \int_{-1}^{1}\int_{-1}^{1} G_{s1}^T \sigma^0 G_{s1} \frac{h^3}{12} \left|J\right| d\xi d\eta + \int_{-1}^{1}\int_{-1}^{1} G_{s2}^T \sigma^0 G_{s2} \frac{h^3}{12} \left|J\right| d\xi d\eta \tag{5.41}$$

for a given node i,

$$G_{s1}^i = \begin{bmatrix} 0 & \frac{\partial N_i}{\partial x} & 0 \\ 0 & \frac{\partial N_i}{\partial y} & 0 \end{bmatrix} \tag{5.42}$$

$$G_{s2}^i = \begin{bmatrix} 0 & 0 & \frac{\partial N_i}{\partial x} \\ 0 & 0 & \frac{\partial N_i}{\partial y} \end{bmatrix} \tag{5.43}$$

Although the shear contribution for the geometric stiffness matrix is negligible for thin plates, its effects can be significant for thicker plates.

5.4 Model Validation

The proposed doubly curved eight-node piezolaminated composite shell element (Q8) is first validated by considering both a simply supported on all sides(SSSS) laminated composite plate and a clamped on all sides(CCCC) laminated composite plate free vibration problems. Both plates have the same geometry and material properties and are modeled with the present shell element with the principal radii of curvature $R_x = R_y = \infty$. The material properties for all layers of the laminates are identical: moduli of elasticity $E_{11}/E_{22} = 40$; moduli of shear $G_{23} = 0.5E_{22}$, $G_{13} = G_{12} = 0.6E_{22}$; Possion's ratios $\nu_{12} = 0.25$, $\nu_{21} = 0.00625$; mass density $\rho = 1.0kg/m^3$; shear correction factor $\kappa = \pi^2/12$ and the thickness of all layers are equal.

The first 6 natural frequencies are computed for symmetric three cross-ply ($0°/90°/0°$) rectangular laminates with different length-to-width ratios $a/b = 1, 2$, thickness-to-width ratios $t/b = 0.001, 0.2$. For comparison with the known results, non-dimensional natural frequencies are given by $\bar{\omega} = (\omega b^2/\pi^2)\sqrt{\frac{\rho h}{D_0}}$, where $D_0 = E_{22}h^3/12(1 - \nu_{12}\nu_{21})$.

The convergence study of frequency parameters $\bar{\omega}$ for SSSS plate is presented in Table 5–1, while the corresponding convergence study for CCCC plate is performed in Table 5–2. In both SSSS and CCCC cases, the results converge well to Liew's [56] [57] meshfree results and Ferreira's [47] finite element results using four-node bilinear quadrilateral element Q4 (30×30).

Table 5–1: Convergence study of non-dimensional frequencies $\bar{\omega}$ for SSSS plate

a/b	t/b	Q8 mesh	Modes					
			1	2	3	4	5	6
1	0.001	5×5	6.7314	11.8920	25.5751	26.3716	41.0443	43.1898
		10×10	6.6261	9.4612	16.2982	25.1296	26.6165	27.0241
		20×20	6.6255	9.4480	16.2083	25.1154	26.5004	26.6697
		Liew	6.6252	9.4470	16.2051	25.1146	26.4982	26.6572
	0.2	5×5	3.5342	5.7950	7.2343	8.6006	9.4259	10.3137
		10×10	3.5331	5.7753	7.2117	8.5640	9.2667	10.3135
		20×20	3.5331	5.7740	7.2102	8.5617	9.2556	10.3135
		Liew	3.5939	5.7691	7.3972	8.6876	9.1451	11.2080
2	0.001	5×5	2.5403	8.1811	9.3456	19.1729	20.8766	23.1012
		10×10	2.3628	6.6416	6.6738	9.6358	14.3856	14.4385
		20×20	2.3620	6.6257	6.6650	9.4488	14.2893	14.3869
		Liew	2.3618	6.6252	6.6845	9.4470	14.2869	16.3846
	0.2	5×5	1.9347	3.5457	4.9463	5.4471	5.8067	7.1705
		10×10	1.9340	3.5339	4.9243	5.3666	5.7760	7.0651
		20×20	1.9339	3.5331	4.9229	5.3610	5.7741	7.0590
		Liew	1.9393	3.5939	4.8755	5.4855	5.7691	7.1177

Table 5–2: Convergence study of non-dimensional frequencies $\bar{\omega}$ for CCCC plate

a/b	t/b	Q8 mesh	Modes					
			1	2	3	4	5	6
1	0.001	5×5	20.6676	33.1251	43.4429	51.3462	53.7696	64.1933
		10×10	14.7837	18.3406	26.5386	39.5027	39.5878	42.9800
		20×20	14.6668	17.6214	24.5353	35.5906	39.1626	40.7943
		Liew	14.6655	17.6138	24.5114	35.5318	39.1572	40.7685
	0.2	5×5	4.3889	6.7120	7.5500	9.1467	10.0776	11.2690
		10×10	4.3862	6.6808	7.5264	9.1008	9.8953	11.1123
		20×20	4.3860	6.6787	7.5248	9.0979	9.8824	11.1015
		Liew	4.4468	6.6419	7.6996	9.1852	9.7378	11.3991
2	0.001	5×5	9.9913	16.9988	17.9351	24.3452	27.3404	29.1293
		10×10	5.2982	11.1666	11.2488	17.4578	20.8329	21.2108
		20×20	5.1071	10.5342	10.5908	14.3643	19.5870	19.7219
		Ferreira	5.1221	10.6156	10.6727	14.4537	19.9064	20.0430
	0.2	5×5	3.0579	4.2183	5.8837	5.9200	6.6287	7.8328
		10×10	3.0549	4.2049	5.8017	5.8855	6.5869	7.5385
		20×20	3.0548	4.2040	5.7962	5.8832	6.5842	7.5166
		Liew	3.0452	4.2481	5.7916	5.9042	6.5347	7.6885

Table 5–3: Comparison of non-dimensional buckling parameter $\overline{N}_{cr}$ for a SSSS isotropic square plate under uniaxial load N_x^0

	h/a=0.001	h/a=0.01	h/a=0.05	h/a=0.1	h/a=0.2
Thin-plate theory	4.0	4.0	4.0	4.0	4.0
Exact solution	–	–	3.924	3.741	3.150
Closed form solution	4.0	–	3.944	3.786	3.264
10×10 Q4	4.0666	–	3.9930	3.7890	3.1665
Present element Q8	4.0360	4.0297	3.9597	3.7579	3.1399

Next, for an isotropic simply supported square plate (without any piezoelectric elements) under uniaxial N_x^0, which represents the initial compressive load per unit length applied in the x direction, the critical buckling load obtained by the proposed element is validated with existing solutions in the literature.

Table 5–3 summarizes results for plates of various length-to-thickness ratios and compares with the solutions of finite element formulation and code by Ferreira [47], exact solution by Srinivas and Rao [58], and closed form solution [59]. A 10×10 Q8 present shell element is used with the principal radii of curvature $R_x = R_y = \infty$. Non-dimensional buckling parameter $\overline{N}_{cr} = \widehat{N}_x^0 b^2/\pi D$ is presented, where $\widehat{N}_x^0$ represents the corresponding critical load.

The non-dimensional critical buckling load computed using the present element model is in good agreement with the exact solutions as shown in the table. Also as the h/a ratio increases, the solution based on the classical Kirchhoff plate theory results in significant error.

Furthermore, in order to verify the proposed element model for the buckling analysis of smart composite plates, both graphite/epoxy SSSS and CCCC rectangular orthotropic laminated plates are investigated.

To compare with Mandell's [60], [61] experimental results for uniaxial buckling load of SSSS orthotropic plates, a description of the plates tested is given in Table 5–4. The ply layup $5(0, 90)$ indicates that the stacking sequence is $0°/90°/0°90°/0°$ with respect to the load direction (i.e., the x-axis). 'Thornel' plates were made of graphite/epoxy with the same material properties specified as in [65], namely, $E_{11} = 30 \times 10^6 psi$, $E_{22} = 0.75 \times 10^6 psi$, $G_{12} = 0.375 \times 10^6 psi$, and $\nu_{12} = 0.25$.

Table 5–4: Description of orthotropic plates tested by Mandel

Plate number	Material	Fiber by volume	Layup of plies	Dimensions(in)
201	Thornel-25	40.0%	(0,90,90,0)	$10 \times 10 \times 0.055$
202	Thornel-25	40.0%	9(0,90)	$10 \times 10 \times 0.121$
204	Thornel-40	60.0%	5(0,90)	$10 \times 10 \times 0.043$
205	Thornel-40	60.0%	5(90,0)	$10 \times 10 \times 0.043$
206	Thornel-40	60.0%	(0,90,90,0)	$10 \times 10 \times 0.034$
207	Thornel-40	60.0%	(90,0,0,90)	$10 \times 10 \times 0.034$

As shown in Table 5–5, the critical loads obtained from present element model converge to the upper bound of the theoretical and experimental solutions. Limited by the speed and memory of the computer used, the convergence study is only executed to 15×15 elements. The values in parentheses of the 'Buckling mode' column are the number of half-waves of the first buckling mode shape. The critical buckling load for all plates was observed in the(1,1) mode, except for the plate No.207, which buckled first in the (2,1) mode as shown in Figure 5–3.

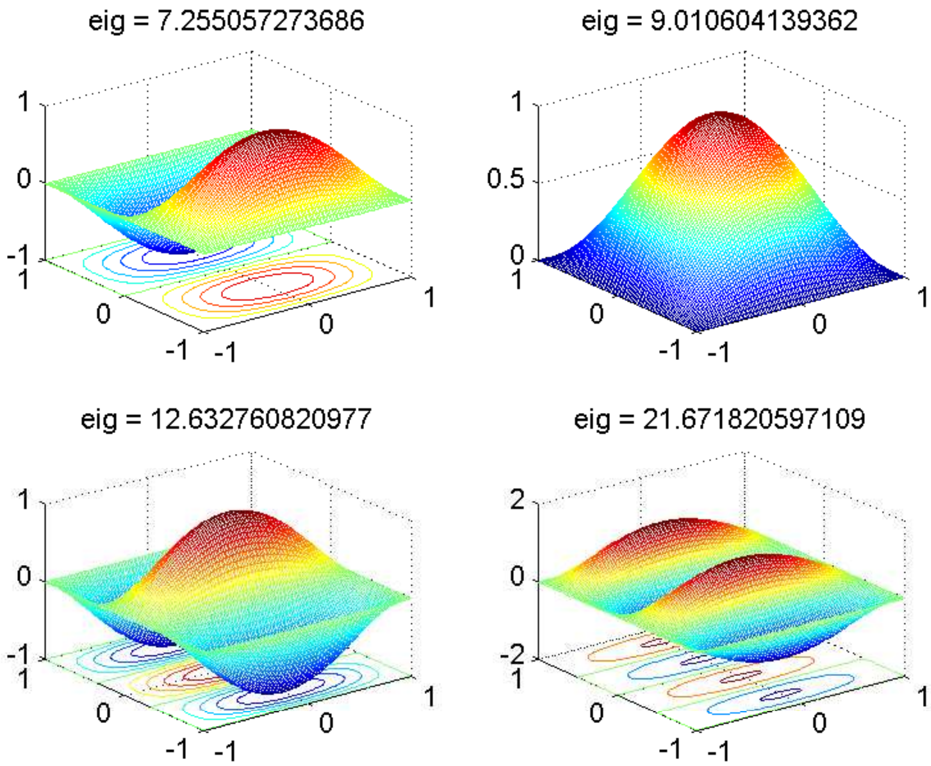

Figure 5–3: The first four buckling modes of Mandell's plate No.207

Table 5–5: Critical loads $-\overline{N}_{cr}, lb/in$ for Mandell's SSSS orthotropic plates

Plate No.	Buckling mode	Experimental	Theoretical	Present element	
				10×10	15×15
201	(1,1)	21.7	19.1	16.9656	16.9309
202	(1,1)	189	204	179.6950	179.3752
204	(1,1)	15.5	18.7	18.4742	17.5775
205	(1,1)	16.3	18.7	18.4742	17.5775
206	(1,1)	6.69	8.72	9.1356	9.1165
207	(2,1)	6.65	7.44	7.4840	7.2551

Table 5–6: Critical uniaxial buckling parameters $-\overline{\sigma}_{cr}b^2/E_{22}h^2$ for CCCC plates under uniaxial load σ_x^0

Laminate description Layup of four plies	cross-ply (0,90,0,90)			angle-ply (45,-45,45,-45)		
a/b	1.0	1.5	2.0	1.0	1.5	2.0
Zhang [64]	109.90	–	–	106.87	–	–
Chia ([62] [63])	112.65(1)	87.74(2)	76.83(3)	113.67(1)	95.73(2)	89.86(3)
Present Q8 (10×10)	111.6899	90.1845	86.6119	107.5126	97.1852	96.9318
Present Q8 (15×15)	110.31(1)	86.92(2)	81.10(3)	105.46(1)	92.76(2)	89.62(3)

Results are shown in Table 5–6 for a set of cross-ply and angle-ply ($\pm 45°$) CCCC plates, each composed of four plies graphite/epoxy with plate thickness $h = 0.091$ inch. They are consistent with the results by the Galerkin method obtained by Chia and Prabhakara [62], [63] with the displacement function carrying 6 sigificant figures and by Zhang and Mathews [64] with the displacement function carrying 15 siginificant figures. The values in parentheses are the number of half-waves of the first buckling mode shape in the load σ_x^0 (x-) direction.

Last, the Scordelis -Lo Roof test problem [67] for shell element is studied to verify the proposed element model for the static and vibration analysis of cylindrical shells.

The roof is shown in Figure 5–4. It has radius $R = 25$, length $L = 50$, thickness $t = 0.25$, subtended angle of 80°, Youngs modulus $E = 4.32 \times 10^8$, and Poisson's ratio $\nu = 0.0$ (all in consistent units). The roof is supported at each end by rigid diaphragms, and the other two edges are free. Uniform vertical gravity load of 90.0 per unit area is applied. The converged numerical solution of the vertical displacement at midside of free edge is 0.3024, as reported in [67]. The solution comparison is given in Table 5–7 and the solution of the proposed shell element agrees well with the analytical solution and other finite element solution.

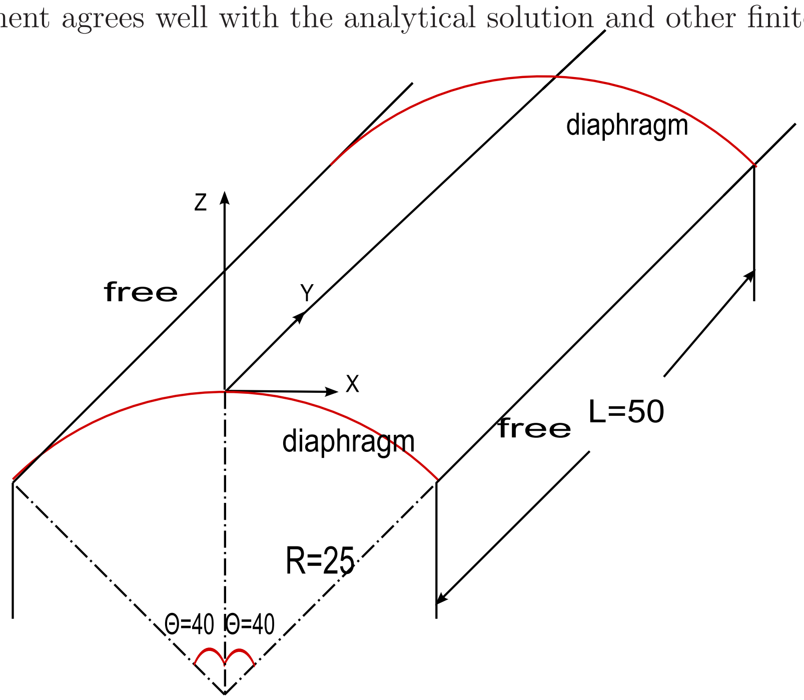

Figure 5–4: Scordelis -Lo Roof

Table 5–7: Scordelis -Lo roof deflection at roof centre of free edge

Element for a quarter roof Element for whole roof	4×4 8×8	8×8 16×16	16×16 32×32
EAS element [68] for a quarter roof	0.2897	0.2973	0.3024
Proposed element for the whole roof	0.2954	0.3027	0.3028
Analytical solution [67]		0.3024	

5.5 Case Studies

Active controls of both vibration and buckling of the same cantilevered laminated composite plate and active vibration control of a semicircular piezolaminated steel shell are studied.

As shown in Figure (5–5), a graphite/epoxy composite cantilever plate ($Rx = Ry = \infty$) with PZT piezoceramic senor and actuator bonded to both the upper and lower surfaces is considered. The plate consists of four composite layers ($-45°/45°/-45°/45°$) of $2.5\,mm$ thickness each. The two outer piezoelectric layers are of $0.1\,mm$ thickness each. The material properties are as in Table 5–8.

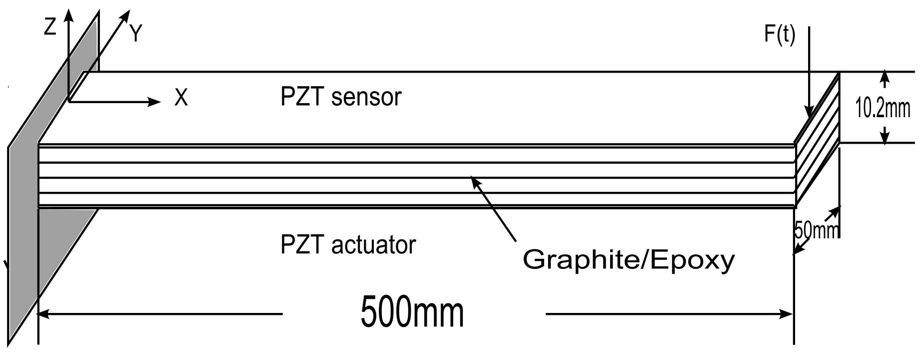

Figure 5–5: A composite cantilever plate with distributed PZT sensor and actuator

As shown in Figure (5–6), a semicircular steel shell embedded with PZT piezoceramic senor and actuator layers on the top and bottom surfaces is considered. The shell is $150mm$ wide and $6mm$ thick with the inner radius of $300mm$ or ($Rx = R = 300mm$, $Ry = Rxy = \infty$) for the proposed plate/shell element. One end of the shell is fixed and the other end is free. The thicknesses of the two outer piezoelectric layers are $0.25mm$. The material properties are as Table 5–8.

Table 5–8: Graphite/epoxy, PZT piezoceramic and Steel material properties

Properties	Piezoceramic PZT-G1195N	Graphite/epoxy T300/976	Steel
Elastic modulus $E_{11}(Pa)$	63.0×10^9	150.0×10^9	2.1×10^{11}
Elastic modulus $E_{22} = E_{33}(Pa)$	63.0×10^9	9.0×10^9	2.1×10^{11}
Shear modulus $G_{12}(Pa)$	24.2×10^9	7.1×10^9	$--$
Shear modulus $G_{13} = G_{23}(Pa)$	24.2×10^9	2.5×10^9	$--$
Poisson's ratio $\nu_{12} = \nu_{13} = \nu_{23}$	0.3	0.3	0.3
Density $(\rho Kg/m^3)$	7600.0	1600.0	7800.0
Electric permittivity $(\epsilon_{11} = \epsilon_{22}(F/m))$	1.53×10^{-8}	$--$	$--$
Electric permittivity $\epsilon_{33}(F/m)$	1.50×10^{-8}	$--$	$--$
Piezoelectric strain constant $(d_{31} = d_{32}(m/V))$	2.54×10^{-10}	$--$	$--$

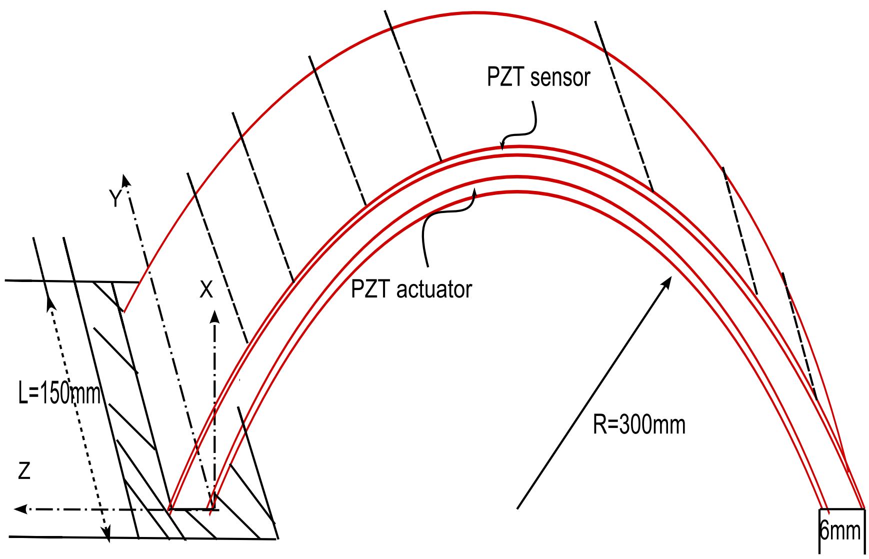

Figure 5–6: A semicircular piezolaminated shell with one end fixed

5.5.1 Active Vibration Control of a Cantilever Composite Plate

This case was also studied by Balamurugan and Narayanan [24]. In their paper, a nine-noded quadrilateral shell element was derived and different classical control laws, including constant gain negative velocity feedback, direct proportional feedback and Lyapunov feedback are applied to compare the vibration control performance. As shown here, consistent results are obtained.

Table 5–9 shows the first six natural frequencies comparation. The first four modes are well matched, only the two higher modes shift away. Also the first four mode shapes are showed in Figure 5–7.

Table 5–9: The first six natural frequencies (Hz) for a cantilever composite plate

Mode	Q9 shell element [24]	Present Q8 shell element(40×4)
1	27.05	26.3616
2	127.11	123.8683
3	169.17	164.1050
4	475.86	455.8193
5	780.64	640.6344
6	797.76	761.5805

From the results of the first case study about the vibration control of a cantilever beam of the previous chapter, while only first two modes are used to design the LQR/LQG controller, still effective control results have been obtained. The intuitive choice is proved to be consistent with the physical and experimental results. For the more complex composite laminated plate case, first we have to determine the smallest states model which can keep an accurate representation of the frequency response characteristics.

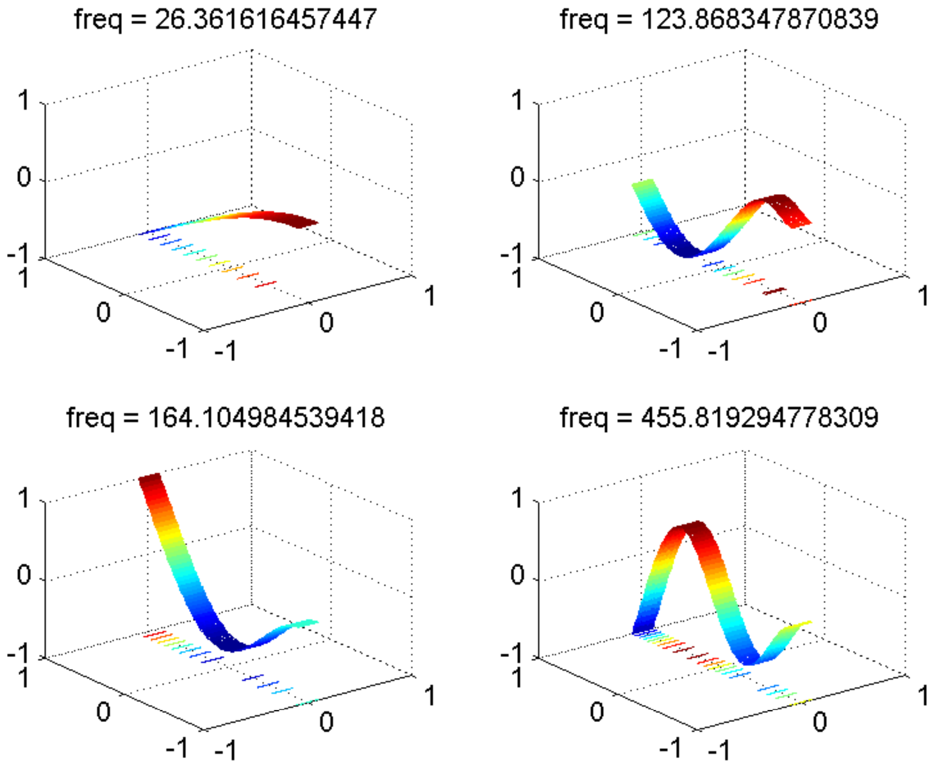

Figure 5–7: The first four vibration modes of a composite cantilever plate with distributed PZT sensor and actuator

Suppose the first six modes are chosen to build an approximate reduced model. Then a balanced LQG state space representation can be given. By the definition of the previous section "The balanced LQG compensator", λ_i, $i = 1, \cdots, 6$ are LQG singular values of the structure system and its approximate LQG singular values $\lambda_{approx} = \sqrt{S_c \times S_e}$. From the control Grammian G_c in equation 3.15 and the observer Grammian G_o in equation 3.23, Hankel singular values can be obtained as $\gamma = \sqrt{G_c \times G_o}$. Then the approximate reduced LQG compensator singular values $\sigma = \gamma \times \lambda_{approx}$ can be obtained. Figure 5–8 shows all the singular values sorted in increasing or decreasing order. It can be seen that the approximate LQG singular values of the reduced model are the same as the LQG singular values of the structure system and this means that the six modes reduced model can accurately represent the full states finite element model. Furthermore, the sorted approximate LQG compensator singular values show that only the first mode has a large contribution to the impulse response of the tip displacement, the other modes can be reduced.

Next, only the first mode is used to design an LQR/LQG compensator to control the vibration of the cantilever composite plate. An impulse load of $0.1N$ is applied at the free end of the plate. The dynamic response is calculated by using only the first mode. As in the study by Balamurugan and Narayanan [24], the damping is ignored.

To design an LQR/LQG compensator, we have one mode (or two states) least reduced model to control. As the derivative of the sensor output is assumed to be computed, with one surface bonded sensor and one surfaced bonded actuator,

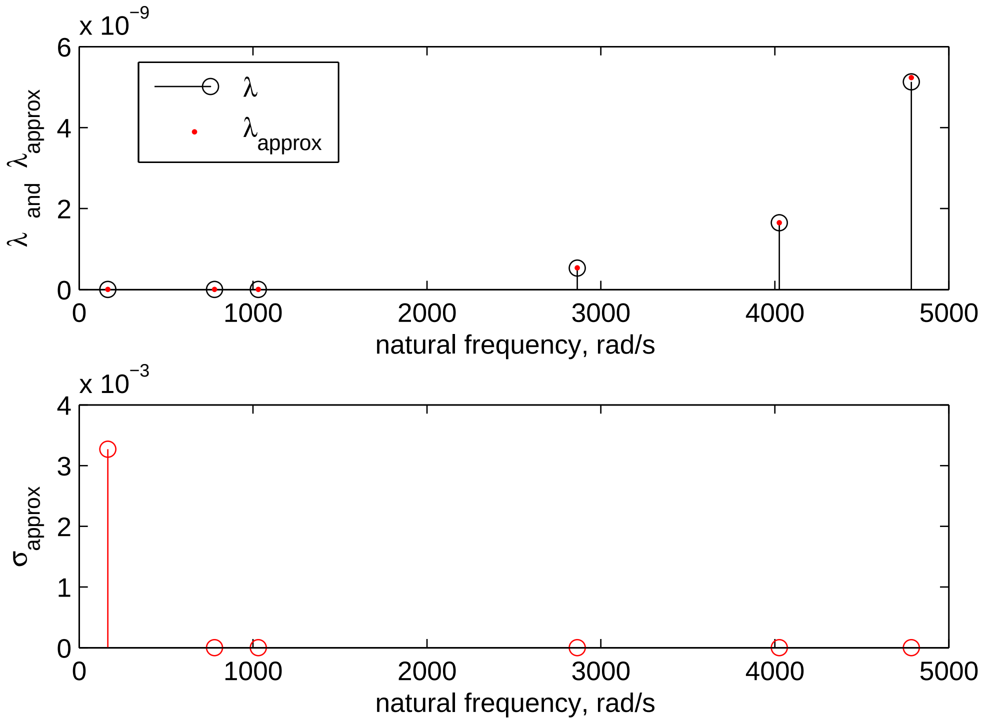

Figure 5–8: LQG singular values, approximate LQG singular values and approximate LQG compensator singular values

a full state feedback LQR controller can be designed. While the tip vertical displacement is set as performance output, the state weight matrix Q can be computed from output matrix C with $Q = C^T C$ and control parameters are taken as $\alpha = 10^4$ and $\beta = 1$.

Figure 5–9 shows the impulse response of the plate's tip displacement, for which the control is started after a lapse of $0.5s$ in order to compare both the controlled and uncontrolled responses. It shows good agreements with the study [24]. The corresponding frequency response of the uncontrolled and controlled tip displacement is shown in Figure 5–10. The sensor output voltage and the actuator control voltage are shown in Figures 5–11 and 5–12. It is seen that the actuator control voltage has an absolute value less than the breakdown voltage ($V_{max} = h_a \times 1.0v/\mu m = 100v$) of the piezoelectric PZT-actuator (i.e. $-100v < V_{control} < 100v$). The designed LQR/LQG controller has suppressed the vibration of the plate under the tip impulse load.

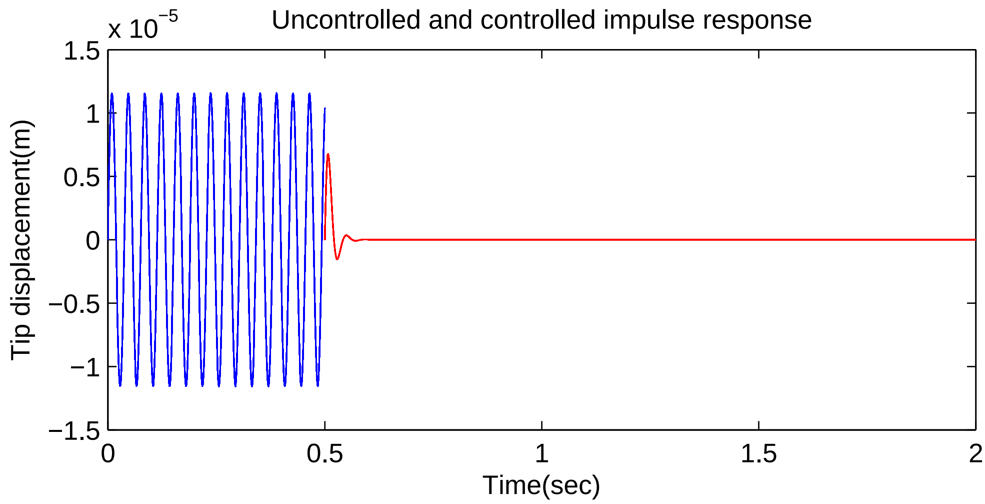

Figure 5–9: Tip displacement of the smart composite plate

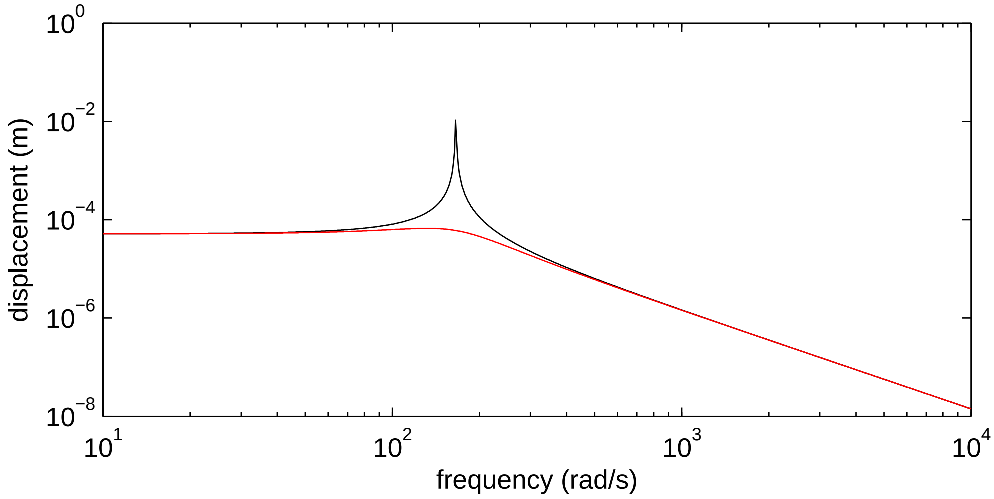

Figure 5–10: Frequency responses of the smart composite plate

Then the active vibration control of the plate subjected to random loading is studied. The random load as in Figure 5–13, which is a band limited white noise of Power Spectral Density ($PSD = 1.1722 \times 10^{-6} N^2/(rad/s)$) in the frequency range of 0-1000Hz, is applied on the tip of the cantilever plate. The uncontrolled and controlled responses at the free end of the plate are shown in figures 5–14 and 5–15. Figure 5–16 shows the control input of the actuator is well below the breakdown voltage. The mean square response (MSR) for the both uncontrolled and controlled cases are 7.4421×10^{-8} and 2.0486×10^{-10}, respectively. The MSR reduction factor is about 363, which indicates that the distributed sensors and actuators are effective in controlling the random vibration also.

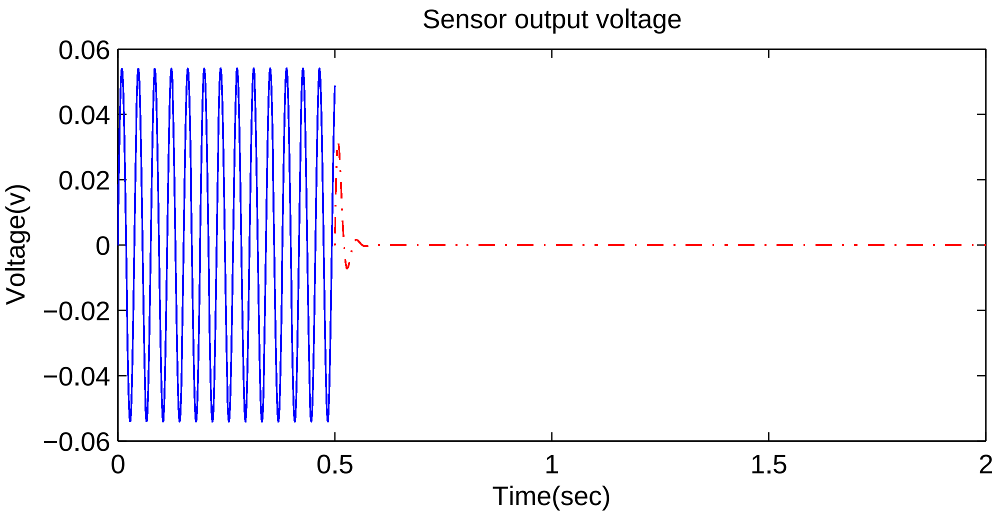

Figure 5–11: Sensor output voltage

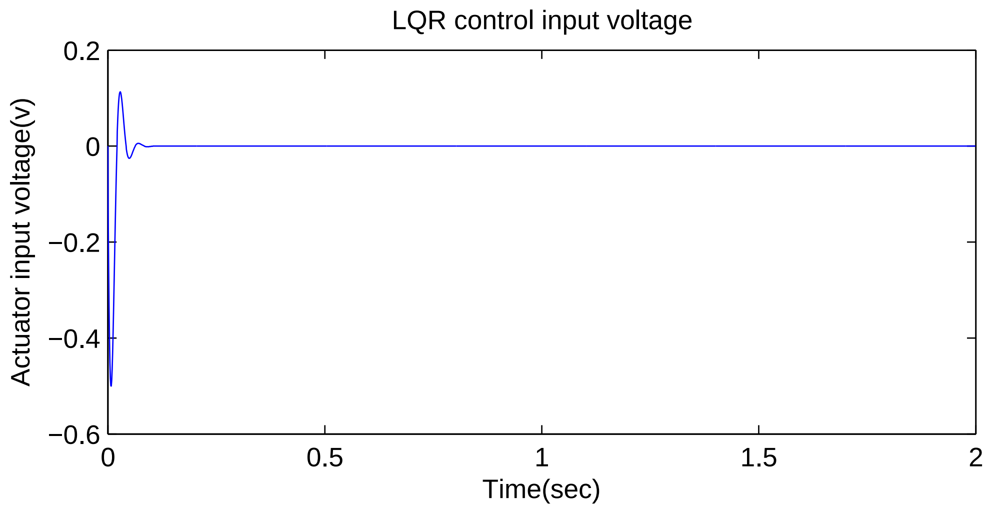

Figure 5–12: Actuator control input voltage

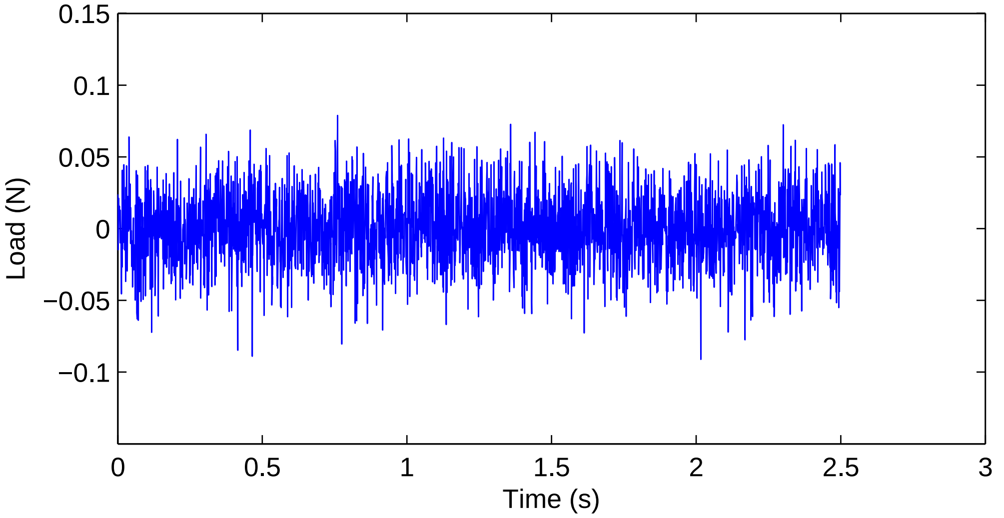

Figure 5–13: Random load history in the frequency range of 0–1000Hz

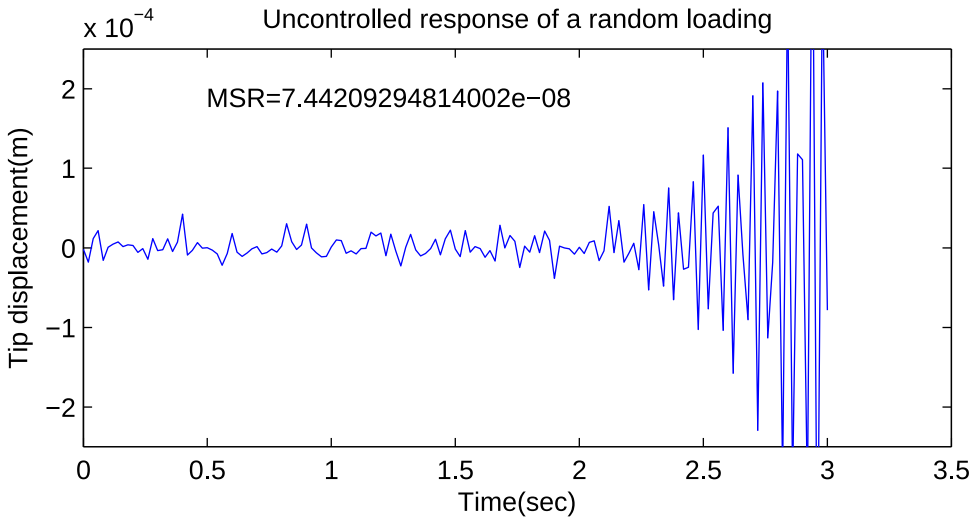

Figure 5–14: Uncontrolled response of the smart composite plate due to the random loading

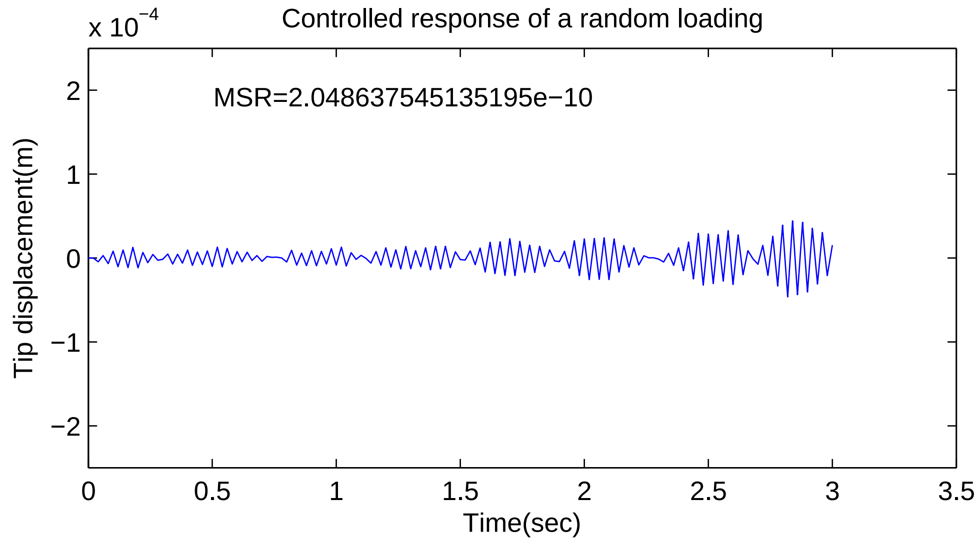

Figure 5–15: Controlled response of the smart composite plate due to the random loading

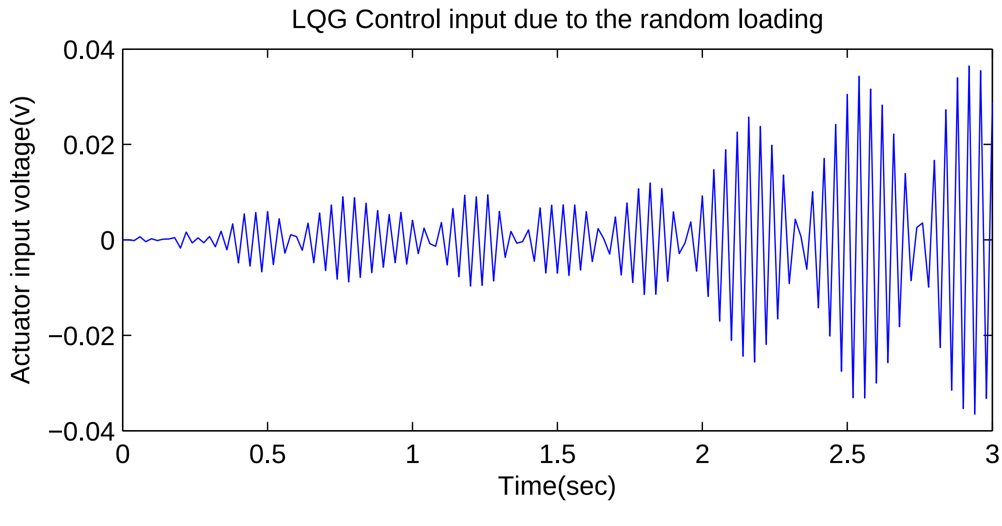

Figure 5–16: Actuator control input of the smart composite plate due to the random loading

5.5.2 Active Buckling Control of the Cantilever Composite Plate

The active buckling control of the same plate as the last case with uniaxial compressive load per unit length N_x applied in the x-direction is studied in this case. Table 5–10 shows the first six buckling loads P_{cr} and Figure 5–17 shows the first four buckling mode shapes. The results show the critical buckling load can be increased to the second buckling load (i.e. $210840.66N/m$) theoretically which is about 9 times of the first buckling load (i.e. $23483.67N/m$).

Table 5–10: The first six buckling loads (N/m) for a cantilever composite plate

Mode	1	2	3	4	5	6
P_{cr}	23483.67	210840.66	582420.08	1130344.14	1840004.69	2689188.84

The weight matrices $Q = C^TC, R = I$ and control parameters $\alpha = 10^4$ and $\beta = 1$ are kept the same as in the active vibration control design of the last case study. The feedback gain matrix $[G]$ is computed for an axial load exceeding $P = P_{cr2}$ so that the plate is forced to buckle in the second mode.

Both the one mode minimal model and the first six modes reduced model of the system are studied. Figure 5–18 shows all the singular values sorted in increasing or decreasing order. It can be seen again that the approximate LQG singular values of the six-mode reduced model are the same as the LQG singular values of the structure system so that the six-mode reduced model can accurately represent the full state finite element model. From the sorted LQG compensator singular values, three modes have large contributions to the impulse response of the tip displacement, the minimal realization of the system should include at least these three modes. But for the approximate LQG compensator singular values,

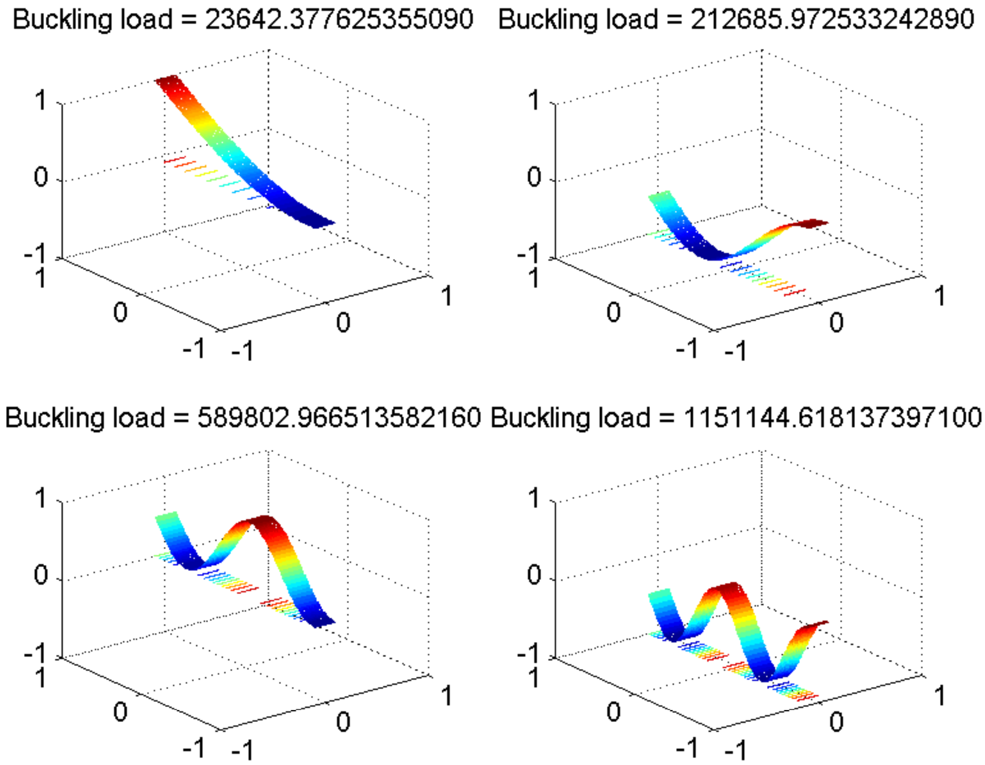

Figure 5–17: The first four buckling modes of a composite cantilever plate with distributed PZT sensor and actuator

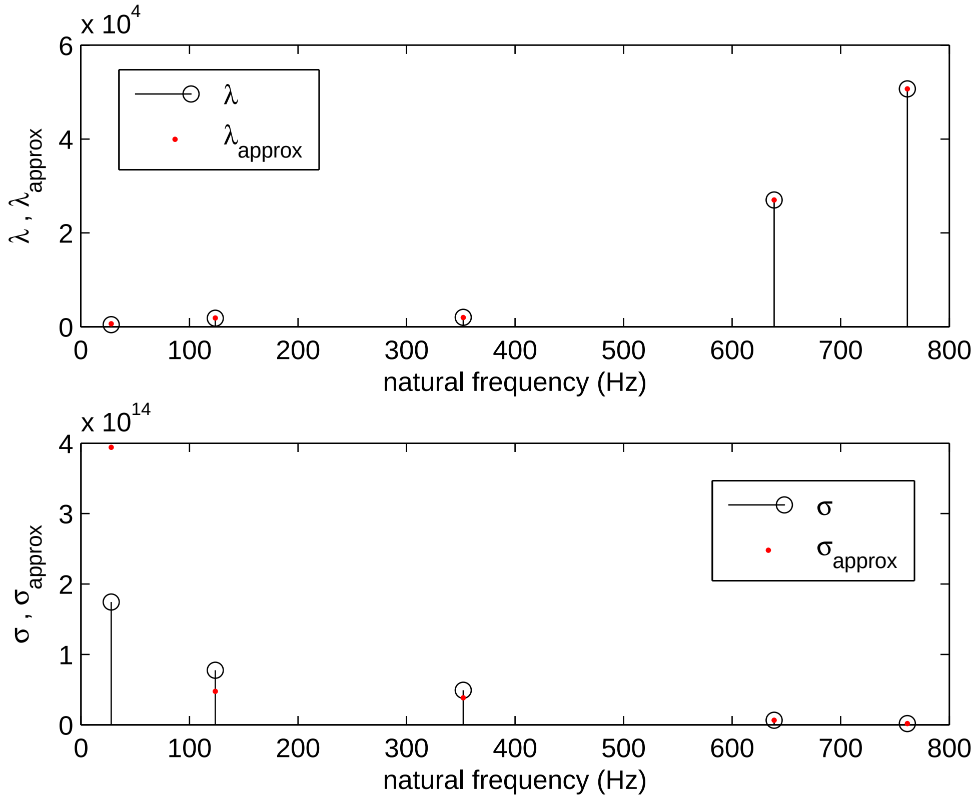

Figure 5–18: LQG singular values, approximate LQG singular values of both system and LQG compensator

only the first mode has a large contribution (about 8 times of the second one) to the impulse response of the tip displacement, thus the other modes can be reduced. Next the six-mode model is applied for the first buckling mode control design.

The resulting sensor output voltage to a 0.1N impulse load applied on the tip of the plate and the control input voltage of the actuator for the axial compressive load $P = 0.9P_{cr2}$ are shown in figures 5–19 and 5–20. The time and frequency responses of the impulse load for the axial compressive load $P = 0.9P_{cr2}$ are shown

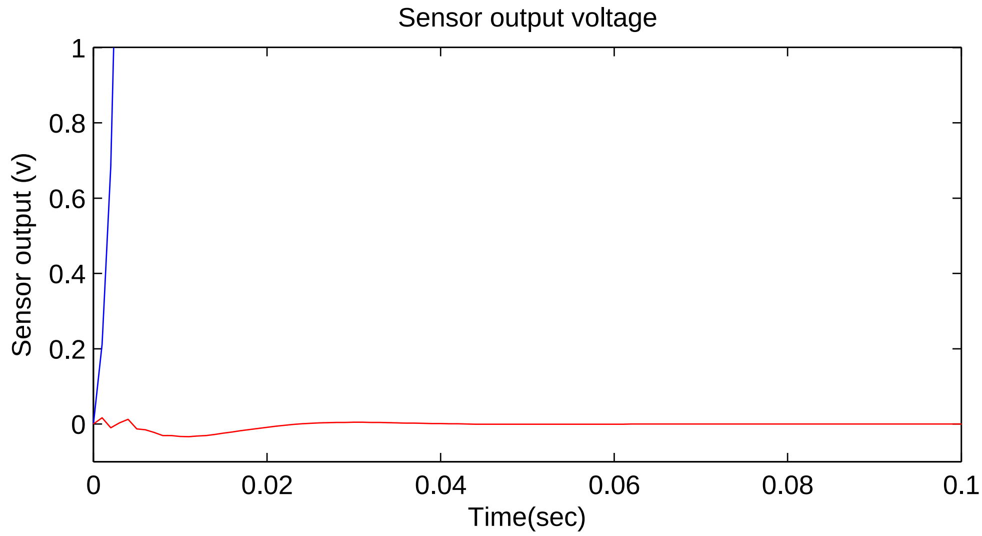

Figure 5–19: Sensor output voltage of the buckling smart plate

in figures 5–21 and 5–22. The time response shows the uncontrolled buckling displacement and controlled stabilizing displacement and the sensor output shows the corresponding voltage outputs also in both uncontrolled and controlled cases. For the comparison, both the controlled frequency responses of the two models are shown in Figure 5–22. Obviously the only one-mode model cannot control the higher two modes and two more sesors/actuators segmented pairs are needed to build an approximate minimal reduced model. It is seen that the actuator control voltage in 5–20 has an absolute value less than the breakdown voltage ($V_{max} = h_a \times 1.0v/\mu m = 100v$) of the piezoelectric PZT-actuator. The designed LQR/LQG controller has stabilized the first buckling mode to the second buckling load P_{cr2}.

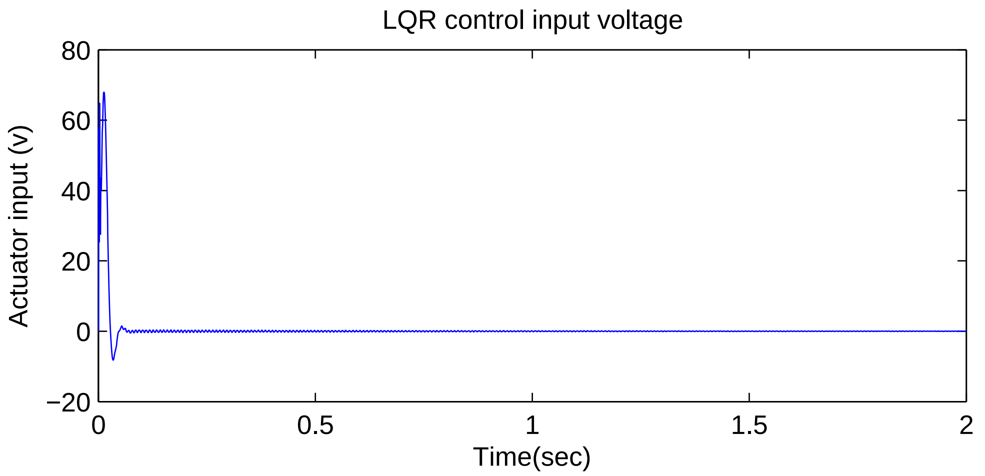

Figure 5–20: Actuator control input of the buckling smart plate

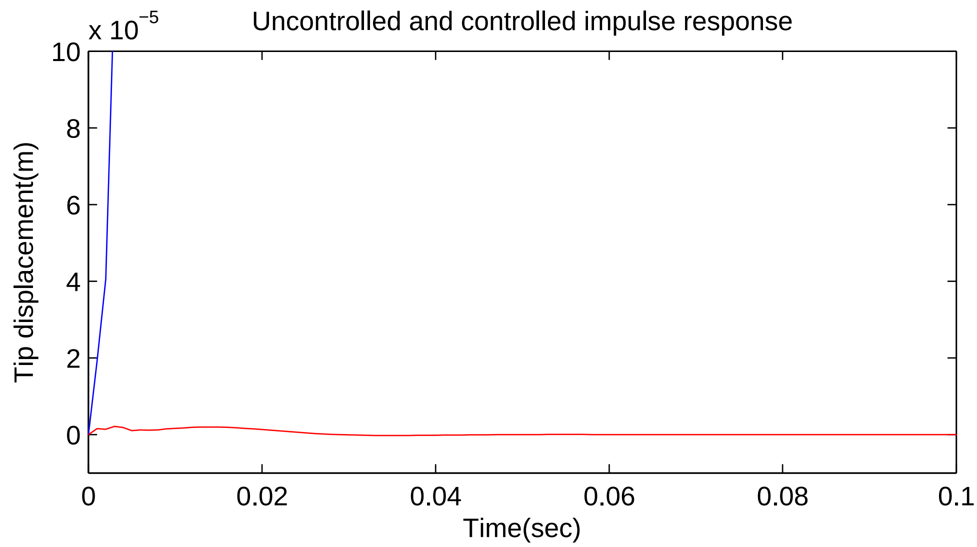

Figure 5–21: Tip displacement of the buckling smart plate

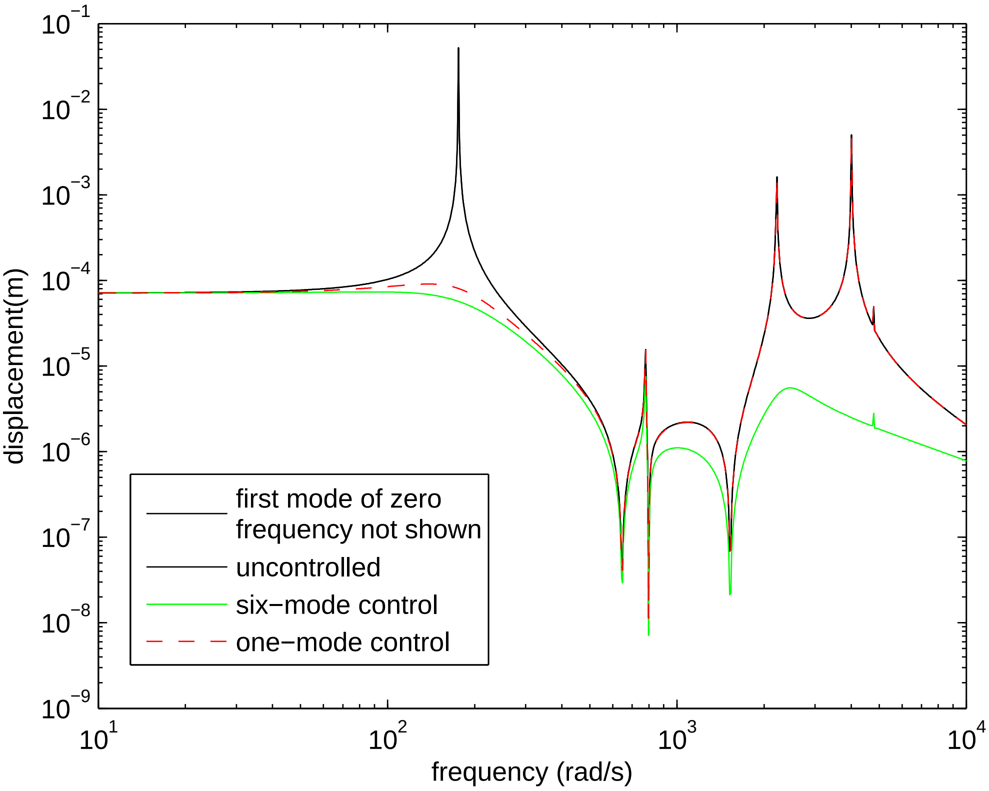

Figure 5–22: Frequency responses of the buckling smart plate

5.5.3 Active Vibration Control of a Semicircular Piezolaminated Steel Shell

This case was also studied by Balamurugan and Narayanan [24]. The analysis in this thesis shows that consistent results are obtained.

Table 5–11 shows the first six natural frequencies comparison. They are well matched with the shell modeled using the same mesh size (25×4).

Table 5–11: The first six natural frequencies (Hz) for a semicircular piezolaminated steel shell

Mode	Q9 shell element [24]	Present Q8 shell element
1	7.16	7.1749
2	11.59	11.5669
3	22.61	22.6180
4	63.26	63.3035
5	77.4	77.3141
6	172.7	172.4277

The first six modes are chosen to build an approximate reduced model. As shown in Figure 5–23, the approximate LQG singular values of the reduced model are the same as the LQG singular values of the structure system. This means that the six modes reduced model can accurately represent the full states finite element model. But the sorted approximate LQG compensator singular values also show that only the first and the third modes have contributions to the impulse response of the tip displacement, the other modes can be reduced. From the physical view, the second and the fourth modes are in the width direction and hence do not participate in the radial and hoop direction responses.

From the above observation, we can determine the smallest model which can keep an accurate representation of the frequency response characteristics to include

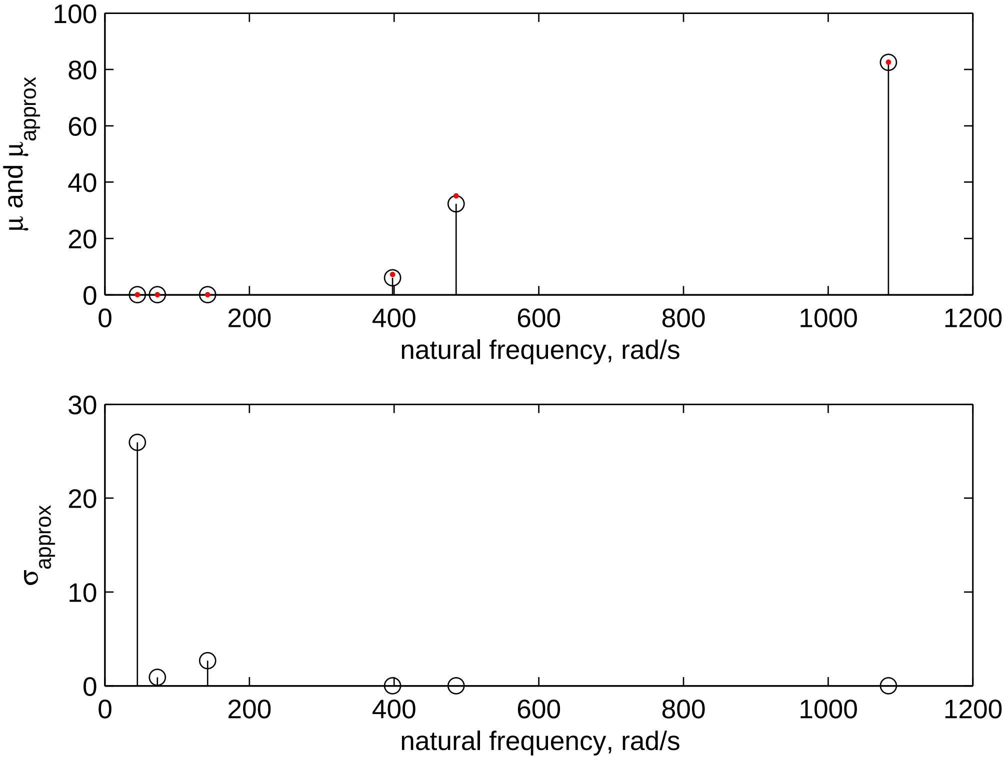

Figure 5–23: LQG singular values, approximate LQG singular values and approximate LQG compensator singular values

only the first and third modes. Next, only these two transverse modes are used to design an LQR/LQG compensator to control the vibration of this piezolaminated semicircular shell. An initial structural dampings are assumed to be 0.0020 and 0.0064 for the two modes. An impact line load of $2000/3\,(N/m)$ is applied at the free end of the shell along the hoop direction as in the study by Balamurugan and Narayanan [24] for comparison. The dynamic tip responses without and with control are evaluated.

A free time response of the shell's tip displacement without control is shown in Figure 5–24. It can be noticed that the higher mode hoop displacement (u) with higher structural damping in the figure dies down quickly. The sensor output voltage in Figure 5–25 shows a beat-like phenomenon due to the strong coupling between the first two transverse modes.

Next, an LQR/LQG compensator can be designed following the same procedures as before. The radial vertical displacement (w) at the free end of the shell is set as the performance output, the state weight matrix Q can be computed from output matrix C with $Q = C^TC$ and control parameters are taken as $\alpha = 10^{10}$ and $\beta = 1$.

Figure 5–26 shows controlled tip responses of the piezolaminated semicircular shell. The actuator control input voltage is also shown in Figure 5–27. It is seen that the actuator control voltage has an absolute value less than the breakdown voltage ($V_{max} = h_a \times 1.0v/\mu m = 250v$) of the piezoelectric PZT-actuator (i.e. $-250v < V_{control} < 250v$). The designed LQR/LQG controller has suppressed the vibration of the semicircular shell under the tip hoop impact load.

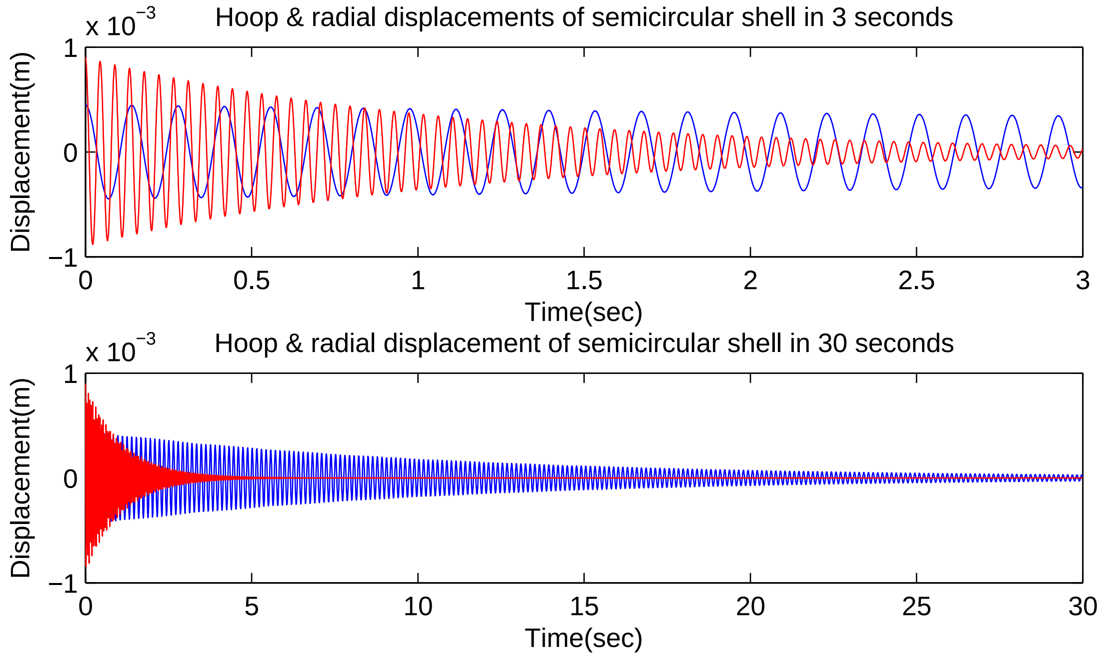

Figure 5–24: Tip displacements of the piezolaminated semicircular shell

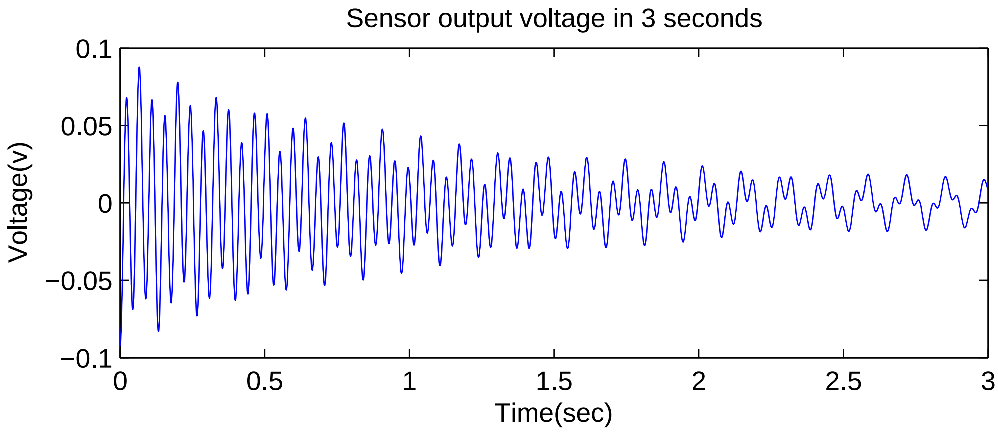

Figure 5–25: Sensor output voltage of the piezolaminated semicircular shell

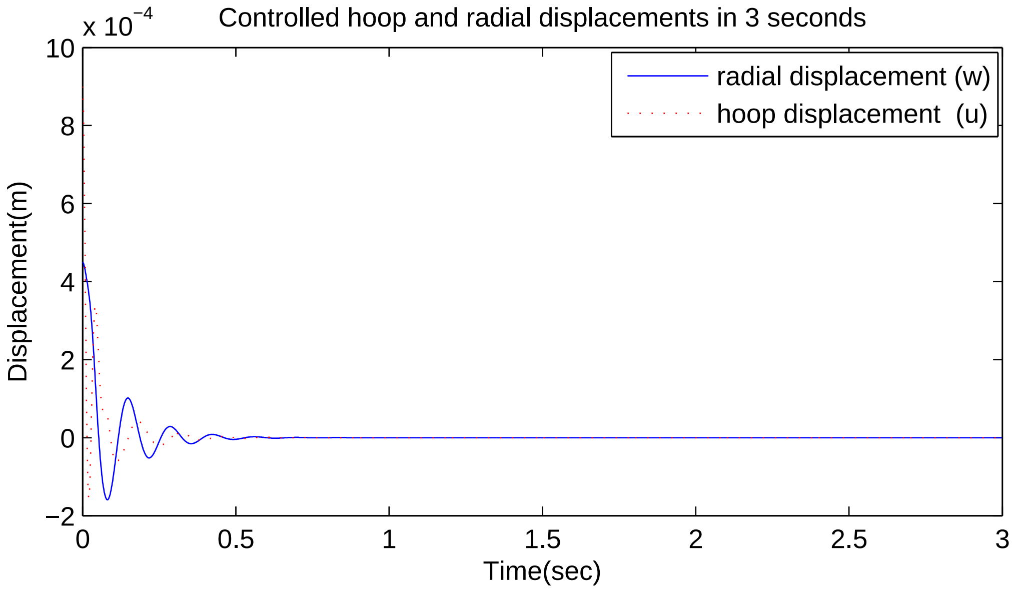

Figure 5–26: Controlled tip displacements of the piezolaminated semicircular shell

The corresponding frequency response of the uncontrolled and controlled tip displacement is shown in Figure 5–28. It can also be seen from this Bode plot that the second and fourth frequencies have the smallest pole amplitudes compared with the other four modes as they are the width direction displacements and do not contribute to the transverse responses.

Lastly, Figure 5–29 shows the controlled tip frequency responses between the two modes (the first and the third mode) least states model control and the six modes (actually only four transverse modes participated) approximate model control.

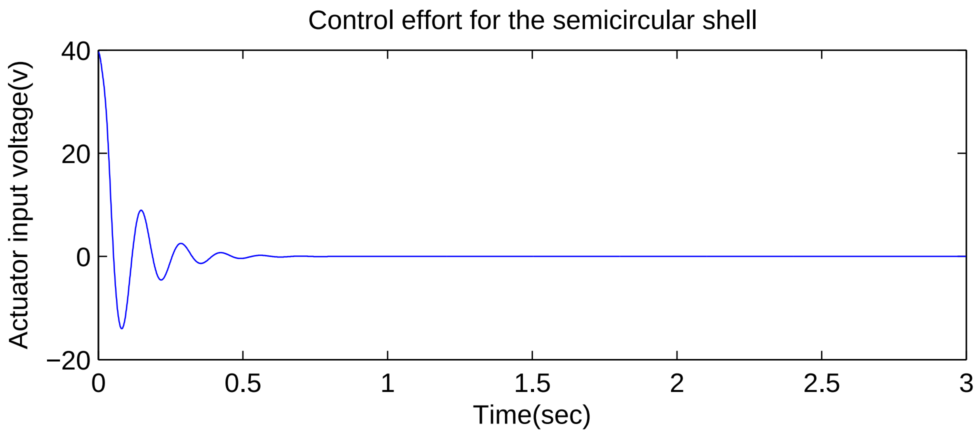

Figure 5–27: Actuator control input voltage of the piezolaminated semicircular shell

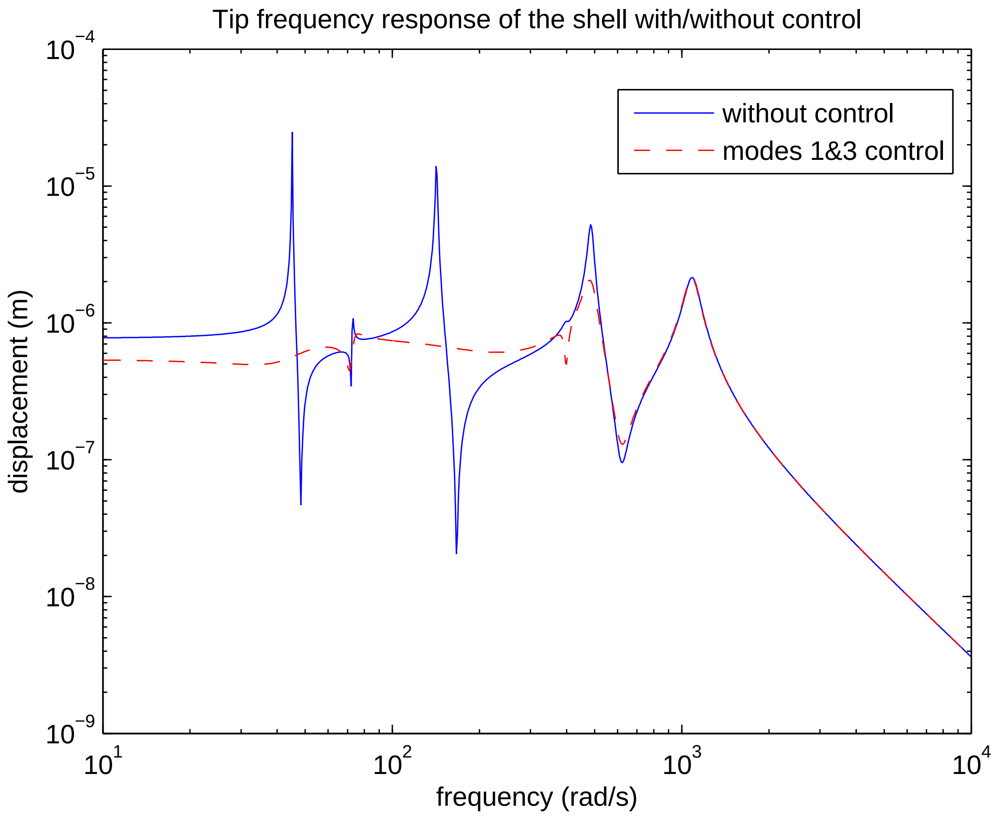

Figure 5–28: Frequency responses of the shell with and without control

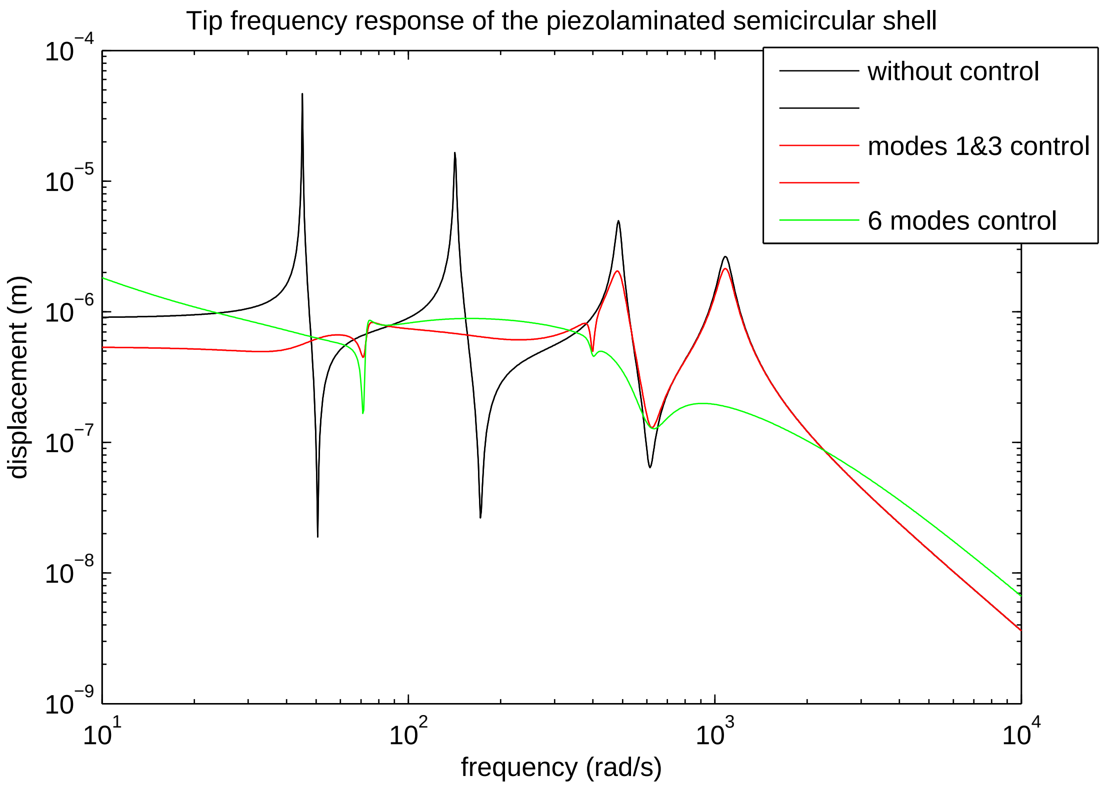

Figure 5–29: Frequency responses comparison of two modes and six modes control of the shell

5.6 Conclusions

1. The finite element analysis and the active control simulation results of the composite plate are consistent with both theoretical analysis results and experimental data.
2. The modal model approach with an LQR/LQG control technique gives much more efficient control results to both the vibration suppression and buckling control with lesser control input peak voltages when compared to the classical controls.
3. The model size reduction technique is necessary in the design of complex real-life structures to determine the smallest states model while keeping accurate representation of the frequency response characteristics. By singular values analysis, the least modes which have the most contributions to the structute system response can be selected to build an approximate reduced modal model.
4. The distributed sensors usually need the dynamic states estimator for the large states structure control.
5. The LQG compensator are also effective in controlling the random vibrations. Numerical simulations show that the required control voltage of the LQG control is in the acceptable range.
6. The first buckling mode of a cantilever plate has been stabilized by feedback control using distributed piezoelectric sensor and actuator. Therefore the controlled plate can support a load up to the second buckling load theoretically.

CHAPTER 6

Contributions, Conclusions and Future Work

6.1 Contributions

1. Piezoelectric laminated beam elements are developed and are applied to active controls of both a cantilevered and a simply supported beam bonded with segmented piezoelectric sensors and actuators. The beam elements are derived based on both classical Euler-Bernoulli theory and layer-wise Timoshenko shear deformation theory. The former for thin beam analysis and the latter for medium thick composite beam analysis. Also, the proposed beam elements are validated with the known theoretical and experimental results and are capable of simulating piezoelectric coupling effects and shear effects of multilayered composite beams accurately.
2. Active vibration suppression of a cantilever beam is studied using LQR/LQG optimal control techniques for different kinds of loading environments. Based on the modal model approach, both full state LQR controller and full state LQG compensator are designed for the effective vibration controls. The control simulation results of both LQR control without environment disturbances or sensor noises and LQG control with the noises are consistent with both the theoretical analysis results and the experimental data in the literature.

3. The control of the first two buckling modes of a simply supported beam under the impulse load is studied using the appoximate reduced modal model and LQR/LQG optimal control techniques. The control simulation results show that the LQR/LQG are very effective in enhancing the buckling load of the beam with the actuator peak control input voltages in the safe range of the breakdown voltage of the piezoelectric actuators. Also, a comparison between the vibration suppression and the buckling control of the same simply supported beam shows that there is essentially no difference between them and the control can be achieved with the same reduced modal model and LQR/LQG control techniques.
4. Piezoelectric laminated shell elements are developed and are used for active control of vibration and buckling of a cantilevered plate surface bonded with distributed piezoelectric sensor and actuator. The shell elements are derived based on the shear flexible curvilinear shell theory. The proposed doubly curved piezolaminated eight-noded serendipity composite shell element is C^0 continuous and having an independent cross-sectional rotation for each layer as a degree of freedom. It can model each layer as an individual Mindlin plate and the displacement continuity between each layer renders the element capable of modeling the piezo layers. The element is validated with the existing theoretical and experimental results in the literature.
5. Vibration suppression of a piezolaminated composite plate with distributed sensor and actuator is studied for both impulse and random loading. Both the one mode least reduced modal model and six modes modal model are

used to design the LQR controllers and static estimators to achieve the control. The control results of both the impulse and random loading are consistent with those in the literature.

6. Buckling control of the first mode of the same piezolaminated composite plate. Numerical simulations show that the first buckling mode has been stabilized and the critical buckling load is enhanced to the second theoretical buckling load with the required control voltage of the actuator in the acceptable safe range.
7. Vibration suppression of a piezolaminated semicircular cylindrical shell with distributed sensor and actuator is studied for linear impact loading. Both the two modes least reduced modal model and six modes modal model are used to design the LQR controllers and static estimators to achieve the control. The control results are consistent with those in the literature.

6.2 Conclusions and Future Work

The vibration and buckling controls of piezolaminated composite beam, plate, and shell structures with integrated piezoelectric sensors and actuators are studied in this dissertation. The finite element model is based on layer-wise first order shear deformation theory in conjunction with linear piezoelectric constitutive relations. The proposed beam, plate, and shell elements are validated by comparing with existing results in the literature.

Modal model approach with LQR/LQG control techniques is applied to design the feedback control systems for the vibration suppression and buckling control of the structures. The control results show that a full state LQR/LQG compensator with a dynamic states observer are effective in controlling the impulse or random load excited vibrations and are capable to achieve control of the environmental disturbances and sensor noise.

The model size reduction technique is used to determine the smallest states model while keeping accurate representation of the frequency response characteristics. By singular values analysis, the least modes which have the most contributions to the structute system response are selected to build the approximate reduced modal model which makes the control of the large states finite element model of the structures possible.

In the future studies, following areas of improvement would be appropriate for the continuation of this research:

- Implementation of active buckling control of piezolaminated composite shell.
- Implementation of a better nonlinear piezoelectric constitutive equation which can precisely represent the piezoelectric-mechanical coupling effects.
- Implementation of an effective model which can estimate the hysteretic behaviour of the piezoelectric material and integrating it with the control system design.
- Implementation of other control system design such as H_∞.
- Implementation of other applications such as noise control and structural health monitoring.

References

[1] Srinivasan, A.V. and McFarland, D.M., 2001, Smart Structures: Analysis and Design. Cambridge: Cambridge University Press.

[2] Wadhawan, V.K., 2007, Smart Structures: Blurring the Distinction Between the Living and the Nonliving. Oxford: Oxford University Press.

[3] Sunar M. & Rao S.S., 1997, Thermo-piezoelectric control design and actuator placement, AIAA J., 35(3): 534–539, 1997.

[4] Suleman A. & Venkayya V.B., 1995, A simple finite element formulation for a laminated composite plate with piezoelectric layers, J. Intell. Mat. Structure, 776–782.

[5] Crawley E.F. and Anderson E.H., 1990, Detailed models of piezoceramics actuation of beams, J. Intell. Mat. Struct. 14–24

[6] Yang J.S., Batra R.C.: A second-order theory for piezoelectric materials, J. Acoustic Soc. Am. 97(1), 280-288, 1995.

[7] Kusculuoglu, Z.Koray, Royston, T.J. Finite element formulation of composite plates with piezoceramic layers for optimal vibration control applications, Smart Materials and Structures, v14, pp 1139-1153, 2005.

[8] Polit O., Bruant I. Electric potential approximations for an eight node plate finite element, Computers and Structures 84, 1480-1493, 2006.

[9] Thornburgh, R.P., and Chattopadhyay, A., Nonlinear Actuation of Smart Composites Using a Coupled Piezoelectric- Mechanical Model, Smart Materials and Structures, Vol. 10, 2001, pp. 743–749.

[10] Pai, P. F., Nayfeh, A. H., Oh, K., and Mook, D. T., A Refined Nonlinear Model of Composite Plates with Integrated Piezoelectric Actuators and Sensors, Int. Journal of Solids & Structures, Vol. 30, 1993, pp. 1603–1630.

[11] Varelis D., Saravanos D.A., 2002. Nonlinear coupled mechanics and initial buckling of composite plates with piezoelectric actuators and sensors. Journal of Smart Materials and Structures 11, 330-336.

[12] Tzou H.S., A new distributed sensor and actuator theory for "intelligent shells", J. Sound and Vibration (1992) 153(2), 335-349.

[13] Iozzi R. and Gaudenzi P., Effective shear deformable shell elements for adaptive laminated structures, J. Intelligent Material Systems and Structures, 12(2001), 415-421.

[14] Pinto Correia I.F., Mota Soares C.M., Mota Soares C.A., Herskovits J., Analysis of adaptive shell structures using a refined laminated model, Composite Structures 66(2004) 261-268.

[15] Saravanos, D. A., and Heyliger, P. R., Mechanics and Computational Models for Laminated Piezoelectric Beams, Plates and Shells, Applied Mechanics Reviews, Vol. 52, 1999, pp. 305–320.

[16] Benjeddou A. Advances in piezoelectric finite element modeling of adaptive structural elements: a survey, Computers and Structures, 76, (2000), 347-363.

[17] Chandrashekhara K., and Bhatia K., 1993, Active buckling control of smart composite plates—finite-element analysis, Smart Mater. Structure, 2, 31-39

[18] Thompson S.P., and Loughlan J., 1995, The active buckling control of some composite column strips using piezoceramic actuators, Comput. Structure, 32, 59-67

[19] Meressi T., and Paden B., 1993, Buckling control of a flexible beam using piezoelectric actuators. Journal of Guidance, Control, and Dynamics, V.16, No.5, 1993, pp977-980.

[20] Cui S., Hao H., Cheong H.K., Numerical analysis of dynamic buckling of rectangular plates subjected to intermediate-velocity impact, Int. J. Impact placecountry-regionEng. 25, 147-167, 2001.

[21] Varelis D, Saravanos D.A., Coupled buckling and post-buckling analysis of active laminated piezoelectric composite plates, Int. J. Solids and Structures, 41, 1519-38, 2004.

[22] Batra,R.C., and T.S., Geng Enhancement of the dynamic buckling load for a plate by using piezoceramic actuators, Smart Mater. Structure, 10, (2001), 925-933

[23] Law W.W., W-H Liao, Huang J., Vibration control of structures with self-sensing piezoelectric actuators incorporating adaptive mechanisms, Smart Materials and Structures, v 12, pp 720-730, 2003.

[24] Balamurugan V., S. Narayanan, Shell finite element for smart piezoelectric composite plate/shell structures and its application to the study of active vibration control, Finite Elements in Analysis and Design, v37, pp 713-738, 2001.

[25] Narayan S., Balamurugan V., Finite element modeling of piezo-laminated smart structures for active vibration control with distributed sensors and actuators, J. of Sound and Vibration, v 262, pp 529-562, 2003.

[26] Bhattacharya P., Suhail H., Sinha P.K., Finite element analysis and distributed control of laminated composite shells using LQR/IMSC approach Aerospace Science and Technology 6(2002) 273-281.

[27] Han J-H, Lee I, Analysis of composite plates with piezoelectric actuators for vibration control using layer-wise displacement theory, Composites B., v 29, pp 621-32, 1998.

[28] Goodwin,G.C., S.F. Graebe, and M.E. Salgado, Control System Design, Prentice-Hall, 2001.

[29] Petersen,I.R. and V. Ugrinovskii, and A. Savkin, Robust Control Design Using H_∞. Springer-Verlag, 2000.

[30] IEEE Standard on Piezoelectricity ANSI/IEEE Std 176-1987

[31] Bathe K.J., 1982, Finite element procedures in engineering analysis,Englewood Cliffs, NJ: Prentics-Hall.

[32] Vinson, J.R. and Sierakowski, R.L.(2002), The Behavior of Structures Composed of Composite Materials, 2nd Edition, Kluwer Academic Publishers, Dordrecht, The Netherlands.

[33] Reddy, J.N., Energy and Variational Methods in Applied Mechanics, John Wiley & Sons Inc., New York, 1984.

[34] Robert M. Jones, Mechanics of Composite Materials, 2nd edition, Taylor & Francis Group, New York, 1999.

[35] Chen,C.T., Linear System Theory and Design, Holt, Rinehart and Winston, New York, 1984.

[36] F.Lewis, V.L.Syrmos, Optimal Control, Wiley, New York, 1995.

[37] Kailath, T., Linear Systems, Prentice-Hall, Englewood Cliffs, NJ,1980.

[38] Kuo, B.C., and Hanselman, D.C., MATLAB Tools for Control System Analysis and Design, Prentice-Hall, Englewood Cliffs, NJ, 1994.

[39] Jonckheere, E.A., and Silverman, L.M., A New Set of Invariants for Linear SystemsApplication to Reduced-Order Controller Design, IEEE Transactions on Automatic Control, vol. AC-28, 1983, pp. 953964.

[40] Opdenacker, P., and Jonckheere, E.A., LQG Balancing and Reduced LQG Compensation of Symmetric Passive Systems, International Journal of Control, vol. 41, 1985, pp. 73109.

[41] Gawronski, W., Balanced LQG Compensator for Flexible Structures, Automatica, vol. 30, 1994, pp. 15551564.

[42] Berlin, A.A., Active control of buckling using piezo-ceramic actuators, 1995, Industrial and Commercial Applications Smart Materials SPIE, Smart Structures & Materials Workshop, San Diego, CA.

[43] Preumont, A., Vibration Control of Active Structures - An Introduction, 2nd Edition, Kluwer Academic Publishers, 2002.

[44] Kwon, Y.W., and Bang H., The Finite Element Method Using MATLAB, 2nd Edition, CRC Press, 2000.

[45] Cook,R.D.,et al.,Concepts and Applications of Finite Element Analysis,4th ed.,John Wiley & Sons,Inc.,New York,2001.

[46] M. Petyt., Introduction to finite element vibration analysis. Cambridge University Press, Cambridge, 1990.

[47] A.J.M. Ferreira. Matlab codes for finite element analysis. Springer, 2009.

[48] Z.P. Bazant and L. Cedolin., Stability of structures. Oxford University Press, New York, 1991

[49] A. Yousefi-Koma, Active vibration control of smart structures using piezoelements, PhD. thesis, Carleton University, 1997.

[50] E.M. Sekouri, Modeling and shape estimation of smart structures for active control, PhD. thesis, Ecole de Technologie Superieure University du Quebec, 2004.

[51] S.X. Xu, T.S.Koko, Finite element analysis and design of actively controlled piezoelectric smart structures, Finite Elements in Analysis and Design, 40, (2004) 241–262.

[52] Reddy, J.N., A Generalization of Two-Dimensional Theories of Laminated Composite Plates, Communications in Applied Numerical Methods, V3, No3, 1987, pp173-180.

[53] Sun, C.T., and Whitney, J.M., Theories for the Dynamic Response of Laminated Plates, J.AIAA, V11, No2, 1973, pp178-183.

[54] Chopra, Inderjit, Review of state of art of smart structures and integrated systems, J.AIAA, V40, No11, 2002.

[55] Amabili, Marco, 2008, Nonlinear Vibrations and Stability of Shells and Plates. Cambridge: Cambridge University Press.

[56] K.M. Liew, J. Wang, T.Y. Ng, and M.J. Tan, Free vibration and buckling analyses of shear-deformable plates based on FSDT meshfree method. Journal of Sound and Vibration, 276: 9971017, 2004.

[57] K.M. Liew, Solving the vibration of thick symmetric laminates by reissner/mindlin plate theory and the p-ritz method, Journal of Sound and Vibration, 198(3): 343360, 1996.

[58] Srinivas S and Rao A. K. Buckling of thick rectangular plates AIAA J. 7 1645-6, 1969.

[59] E. Hinton. Numerical methods and software for dynamic analysis of plates and shells. Pineridge Press, Swansea, 1988.

[60] Mandell,J.F., “An Experimental Study of the Buckling of Anisotropic Plates”, M.S.Thesis, Case Western Reserve University, 315pp., (June,1968).

[61] Mandell,J.F., “An Experimental Investigation of Anisotropic Fiber Reinforced Plastic Plates”, Technical Report, AFML TR 68-281pp., (1968).

[62] Chia,C.-Y., “Nonlinear Analysis of Plates”, McGraw-Hill Book Co., 422pp, (1980).

[63] Chia,C.-Y., and Prabhakara,M.K., “Postbuckling Behavior of Unsymmetrically layered Anisotropic Rectangular Plates”, Trans.ASME, Journal of Applied Mechanics, Vol.41, 155-162pp, (1974).

[64] Zhang,Y. and Matthews,F.L., “Initial Buckling of Curved Panels of Generally Layered Composite Materials”, Composite Structures, Vol.1, 3-30pp, (1983).

[65] Leissa,A.W., Buckling of Laminated Composite Plates and shell panels, Technical report, The Ohio State University, 37pp, 213pp, (1980).

[66] V.Balamurugan, S.Narayanan, Shell finite elements for smart piezoelectric composite plates/shell structures and its application to the study of active vibration control, Finite Elements in Analysis and Design 37(9) (2001) 713-738pp.

[67] T.Belytschko, H.Stolarski, W.K.Liu, N.Carpenter and J.S.-J.ONG, Stress Projection for Membrane and Shear Locking in Shell Finite Elements. Computer Methods in Applied Mechanics and Engineering, 51, (1985), 221-258, North-Holland.

[68] K.Rah, W.Van Paepegem, A.M.Habraken, J.Degrieck, R.J.Alves de Sousa, R.A.F.Valente, Optimal low-order fully integrated solid-shell elements. Comput Mech., DOI 10, 1007/s00466-012-0726-6, Springer-Verlag 2012.